Using the fine structure "constant" to probe Dark Energy

David Corre

Mestrado em Astronomia
Departamento de Fisica e Astronomia
2015

Orientador
Carlos Martins, Investigador Coordenador,
Centro de Astrofísica da Universidade do Porto

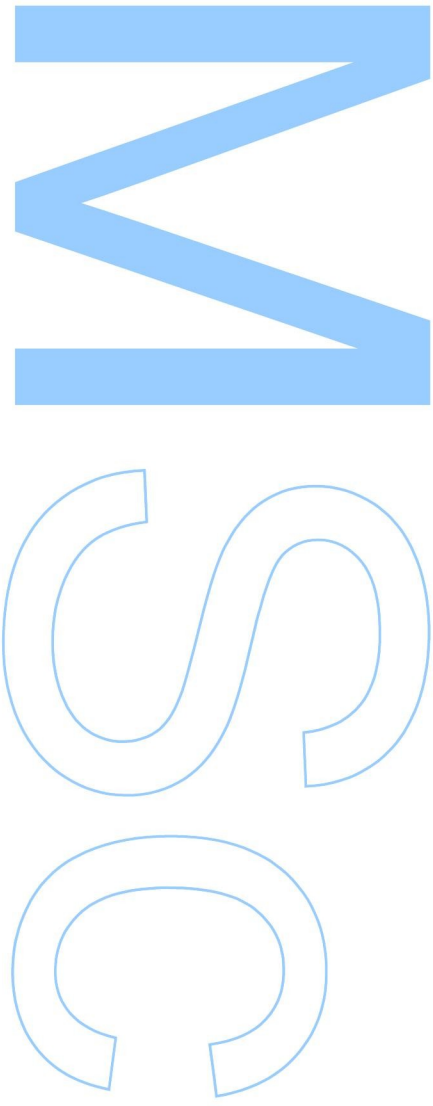

U.PORTO

FACULDADE DE CIÊNCIAS
UNIVERSIDADE DO PORTO

Todas as correções determinadas pelo júri, e só essas, foram efetuadas.

O Presidente do Júri,

Porto, _____/_____/_____

Acknowledgements

I would like to express my gratitude to my supervisor, Prof. Carlos Martins, and whose expertise, understanding, and patience, added considerably to my graduate experience. He not only offered me the opportunity to discover the field of Cosmology but also to pursue in it with by supporting my PhD applications.

I would also like to thank the other members of the jury, Prof. Pedro Viana, and Prof. Jorge Páramos for accepting to be part of the jury and for their availability and the useful advices they gave me.

I must also acknowledge Ana Catarina Leite for her help and useful discussions especially about the Principal Component Analysis part.

A very special thanks goes out to Sofia Silva Santos, who was always ready to help and who saved me several times with various administration processes.

Finally, I thank Paulo Peixoto for his technical support and assistance all along my thesis.

Abstract

Over the past years, independent observations have lead to the conclusion that the expansion of the Universe is accelerating. The nature of its source is unknown and called “Dark Energy” (DE). Understanding this acceleration of the expansion of the Universe is one of the most compelling challenges of cosmology and fundamental physics. To do so, the equation of state (eos), pressure over the density, of Dark Energy is used. So far the most common dataset used to constrain or reconstruct this eos is Type Ia Supernovae observations, which give us some information up to a redshift of 2 (75% of the Universe lifetime). As shown in Webb et al. [2011b], there is an indication of a spatial variation of the fine structure constant, called alpha, at 4.2 sigma using quasar absorption lines. Although this can be due to some yet undetected systematics. As these observations are made up to a redshift of 4, it is interesting to explore these methods to probe dark energy at high redshift.

In this work I will present 3 different approaches to constrain and reconstruct the equation of state of the Dark Energy from observations of the fine structure constant measurements.
The first approach is to perform a quantitative analysis to study whether these measurements might distinguish between a freezing and a thawing behavior, which are the 2 categories in which quintessence models are ranged, of the eos. The second approach is to use the observations to constrain parametric characterisations of the equation of state, assuming toy models (like CPL) and quintessence models to study whether the alpha measurements might bring tighter constraints. The last approach is non-parametric, first using a Principal Component Analysis (PCA) technique and then using a Gaussian Process technique to reconstruct either the eos or the variation of alpha.

The first approach shows that with the future telescope facilities such as ESPRESSO at the VLT, the accuracy of observations will allow to distinguish between some thawing and freezing models as well as between different freezing models. The second approach shows that current alpha measurements already bring slightly tighter constraints on a dynamical equation of state. Finally, the third approach confirms the result of the first one by showing the spectrographs ESPRESSO

at the VLT and HIRES at the E-ELT will be able to distinguish between the freezing model to the thawing model we have chosen for the tested scenarios.

We have applied the Gaussian Process technique but it appears that the scattering of the measurements data of the current data is too important to be used to constrain the coupling factor, ζ, describing a linear coupling between the scalar field responsible for the Dark Energy (in quintessence models) and the electromagnetic field.

Contents

List of Figures

List of Tables

Chapter 1.

The Standard Cosmological Model

1.1 The Cosmological Principle

The Cosmological Principle is a basic working hypothesis whic states that, at each epoch, i.e. a fixed value for the cosmological time, the universe is homogeneous and isotropic on sufficiently large scales. Thus it has the same aspect from each point. The isotropy means that there is no special direction, they all look alike and thus physical properties should not depend on the spatial direction. The homogeneity means that there is no special location in the universe, all places look alike in terms of physical properties. It is also important to notice that we assume that the observable part of the universe is a fair sample of the whole universe.
To avoid local irregularities, the Earth does not look like the Sun for instance, we assume this principle to be valid at large scales of hundred of Mpc only.

This assumption is well supported by observations such as the Two-Degree-Field Galaxy Redshift Survey (2dF) and the Sloan Digital Sky Survey (SDSS) Sarkar et al. [2009] which have confirmed that at scales larger than 100 Mpc the universe is homogeneous and isotropic, or more recently the latest results of the Planck mission reported deviations in the isotropy of the CMB radiation of a few parts of 10^5 Planck Collaboration et al. [2014], Maartens [2011].

1.2 The Backgroung Geometry and distances

1.2.1 The Friedmann-Lemaître-Robertson-Walker metric

The metric tensor is an order 2 tensor which is used to define length and angles for a given coordinate system. The metric tensor, written here $g_{\mu\nu}$, relates the infinitesimal length measurement ds to the chosen coordinates $\{dx^\mu\}$ as:

$$ds^2 = g_{\mu\nu} dx^\mu dx^\nu \tag{1.1}$$

where the Einstein's convention of summing over repeating indices is assumed.

In the following we will use the Friedmann-Lemaître-Robertson-Walker (FLRW) metric which is an exact solution of Einstein's field equations of general relativity for an isotropic and homogeneous universe. It also states that the spatial components may be time-dependent.

In spherical coordinates (r, θ, ϕ) the length ds in the 4D space-time for the LFRW metric is defined as:

$$ds^2 = -c^2 dt + a(t)^2 \left[\frac{dr^2}{1 - Kr^2} + r^2 (d\theta^2 + sin^2\theta \, d\phi^2) \right] \tag{1.2}$$

In the following we choose units such as $c = 3.10^8 m.s^{-1}$.

Here t is the cosmic time, it is the time seen by an observer moving along with the expansion of the Universe, $a(t)$ is the scale factor which describes the time-variation of the distance between two objects in the universe. Thus it is related to the expansion of the universe. Its present value, $a(t_0)$ with t_0 the present time.

The spatial coordinates (r, θ, ϕ) are called the comoving coordinates which remain fixed for an observer moving along with the expansion. Thus comoving coordinates label objects at rest in the expanding frame of the Universe.

It is possible to rewrite the metric 1.2 by changing coordinate from r to χ, where $r = S_K(\chi)$ and:

$$S_K(\chi) \equiv \begin{cases} \frac{1}{\sqrt{K}} \sin(\sqrt{K}\,\chi) & K > 0 \\ \chi & K = 0 \\ \frac{1}{\sqrt{|K|}} \sinh(\sqrt{|K|}\,\chi) & K < 0 \end{cases} \tag{1.3}$$

The metric becomes then:

$$ds^2 = -c^2 dt + a(t)^2 \left[d\chi^2 + S_K(\chi)^2 (d\theta^2 + sin^2\theta \, d\phi^2) \right] \tag{1.4}$$

In this form the proper radial distance of an object at radial coordinate r at time t is defined by $a(t)\ \chi$. The coordiante χ is called the *comoving distance* and defines the distance between two fundamental observers, i.e. comoving with the expansion of the Universe, and thus does not change with the time. For instance if two observers without relative motion are at a comoving distance χ_0 they will remain at the same distance but their physical distance (or proper distance) $a(t)\ \chi_0$ changes with time.

As most of our observations of the Universe rely on the information carried by photons, it is important to understand the behavior of a photon from the moment it is emitted to the moment we observe it. If we consider a static source at a fixed radial comoving distance χ, as light travels along null geodesics, i.e. $ds^2 = 0$, from the metric 1.4 the radial comoving distance is:

$$\chi = \int_{t_e}^{t_{obs}} \frac{c}{a(t)}\,\mathrm{d}t \tag{1.5}$$

where we took $\theta = \phi = 0$ assuming isotropy and t_e the time the photon is emitted and t_{obs} the time it is observed and $a(t)$ the scale factor.

1.2.2 The cosmological redshift

In their rest frames, atoms can emit or absorb radiation at characteristic wavelength, which can be measured accurately in a laboratory. Consequently by observing known emission or absorption lines of distant sources we may observe a shift in the wavelength between the emission and the moment we observe it. If we consider one specific absorption line for which we know from laboratory measurement to have a wavelength λ_{em}, the received wavelength by the observer may be different. We define such a wavelength shift as:

$$z \equiv \frac{\lambda_{rec} - \lambda_{em}}{\lambda_{em}}$$

or equivalently:

$$1 + z \equiv \frac{\lambda_{rec}}{\lambda_{em}} \tag{1.6}$$

where the observable quantity z is called the *redshift*. We will explain why in the next section.

The comoving distance expressed in 1.5 can be seen as the comoving distance of a fixed source emitting a wave crest at $t_1 = t_{em}$ at χ, and $t_2 = t_{obs}$ the time the wave crest is received at $\chi = 0$. If we consider the next wave crest emitted at $t_1 + \delta t_1$ and received at $t_2 + \delta t_2$, since the comoving distance of the source is assumed to be constant we get:

$$\chi = \int_{t_1}^{t_2} \frac{c}{a(t)}\,\mathrm{d}t = \int_{t_1+\delta t_1}^{t_2+\delta t_2} \frac{c}{a(t)}\,\mathrm{d}t \tag{1.7}$$

Assuming that the scale factor remains approximately the same in the time interval δt, 1.7 gives:

$$\frac{\delta t_2}{a(t_2)} - \frac{\delta t_1}{a(t_1)} = 0 \Rightarrow \frac{\delta t_2}{\delta t_1} = \frac{\nu_1}{\nu_2} = \frac{a(t_2)}{a(t_1)} \tag{1.8}$$

where $\nu = \frac{1}{\delta t}$ is the frequency. Combining 1.6 and 1.8 yields:

$$1 \, + \, z \, \equiv \, \frac{\lambda_{rec}}{\lambda_{em}} \, = \, \frac{a(t_{rec})}{a(t_{em})} \tag{1.9}$$

As the universe is expanding, $a(t_{rec}) > a(t_{em})$ and then $z > 0$. In particular if $t_{rec} = t_0$ and if we take $a(t_0) = 1$, the relation between the redshift and the scale factor is:

$$1 \, + \, z \, \equiv \, \frac{1}{a(t_{em})} \tag{1.10}$$

1.2.3 Hubble's law

Before having observations which indicated that the Universe is expanding today, we expected to observe a random distribution of positive and negative wavelengths for different observed galaxies. A positive value means that the visible part of the spectrum is shifted to the red part, it is then called "redshifted". A negative value shifts the visible part of the spectrum to the blue part, it is thus called "blueshifted". Vesto Slipher was the first one to measure the Doppler shift of 41 spiral galaxies by 1921, at the Arizona's Lowell Observatory Slipher [1913, 1915, 1917, 1921] and he observed that all Galaxies beyond the Local Group were redshifted, though some were blueshifted in the Local Group because at these distances the peculiar motion of Galaxies is still comparable to the recession velocity. Edwin Hubble then tried to correlate this result with the distances measurement. He published his result in 1929 and found a linear relation between the redshift and the distance, this is known as the Hubble's law:

$$z \, = \, \frac{H_0}{c} \, D$$

where c is the speed of light, H_0 the Hubble constant giving the recession speed per unit separation between the receiving and emitting galaxies, and D. If we use the Doppler effect, which is for non relativistic motion:

$$z \, = \, \frac{\Delta\lambda}{\lambda} \, \simeq \, \frac{v}{c}$$

where v is the recession velocity of the emitter.

It follows then that in Doppler interpretation the recession velocity of a Galaxy is given by:

$$v \, = \, H_0 \, D$$

On scales larger than 10Mpc all galaxies observed at this time obeyed the Hubble's law so all galaxies recede from us with a speed linearly proportional to the distance. After several decades

of observations and debates, the value of the Hubble constant is considered to be:

$$H_0 \;=\; 100.\, h\; km.s^{-1}.Mpc^{-1} \tag{1.11}$$

where the subscript 0 stands for present, $H_0 \equiv H(t_0)$ and h the dimensionless hubble constant. After the results of Planck $h = 0.678 \;\pm\; 0.09$ Planck Collaboration et al. [2015a].

The generalisation of the Hubble's law at larger distances is given by defining the relative velocity given by the rate of change of proper distance: $d_P = a(t)\chi$:

$$v_{rec} \;\equiv\; \frac{d\, d_P}{dt} \;=\; \dot{a}\,\chi \;=\; (\frac{\dot{a}}{a})\, d_P \;\equiv\; H\, d_P \tag{1.12}$$

where dots represents time derivatives. For nearby objects H can be approximated as a constant.

1.2.4 Cosmological Distances

Comoving distance

When observing objects in the Universe the relevant line-of-sight comoving distance is the distance travelled by the light since its emission. As we have seen above, photons travel along null geodesics and the comoving distance χ can be expressed as 1.5.

Transverse comoving distance

This is the distance between two objects at the same comoving distance, i.e. $d\chi \;=\; 0$. If the two objects are separated by an angle θ and we take $d\phi \;=\; 0$ the metric 1.4 gives us the proper transverse distance:

$$ds \;=\; a(t)\; S_K(\chi)\; d\theta$$

To obtain the comoving transverse distance we just divide by $a(t)$ and then define the transverse comoving distance d_{trans} so that: $\frac{ds}{a(t)} \;=\; d_{trans}\; d\theta$, which implies:

$$d_{trans} \;=\; S_K(\chi) \tag{1.13}$$

Angular diameter distance

For an object of physical length D observed with a small angular size $d\theta$, the angular diameter d_{ang} is defined as $D \;=\; d_{ang}\; d\theta$. The size, D, of the object can be written thanks to the metric

1.4, as we did for the transverse comoving distance, $D = ds = a(t)\ S_K(\chi)\ d\theta$. It is then straightforward to write the angular diameter distance as:

$$d_{ang} = a(t)\ S_K(\chi) = a(t)\ d_{trans} = \frac{d_{trans}}{1+z} \tag{1.14}$$

Luminosity distance

Assuming that an object has an intrinsic luminosity L and radiates isotropically, the flux S that we observe is by definition given by

$$S \equiv \frac{L}{4\pi d_L^2} \tag{1.15}$$

where d_L is the luminosity distance. This relation is valid only in Euclidean space, i.e. at small distances in our Universe. For larger distances the expansion of the Universe has to be taken into account.

Let's then consider a time interval δt_1 in which the source delivers an energy equal of $L\ \delta t_1$ in its rest frame. Because of the space dilution we only receive a fraction of this energy. Assuming an isotropic emission the fraction is $\frac{A}{4\pi d_{trans}^2}$, where A is the observation area (for instance the telescope aperture) and d_{trans} is the transverse comoving distance (i.e. the "comoving object size"). As we have seen the frequency is redshifted with the expansion of Universe so the energy of a photon $h\nu$ is redshifted by a factor $\frac{1}{1+z}$.

The energy we receive is then:

$$E = \frac{L\ \delta t_1\ A}{(1+z)\ 4\pi d_{trans}^2}$$

The flux received per area A and time interval δt_2 is then:

$$S = \frac{E}{A\ \delta t_2} = \frac{L}{(1+z)\ 4\pi d_{trans}^2}\frac{\delta t_1}{\delta t_2} = \frac{L}{(1+z)^2\ 4\pi d_{trans}^2}$$

where we used the 1.8 for the last equality. The luminosity distance hence yields:

$$d_L = (1+z)\ d_{trans} = (1+z)^2\ d_{ang} \tag{1.16}$$

It is important to notice that we have implicitly made the assumption that te number of photons are conserved. It means that no photons is lost (by scattering for instance) or created between the source and the observer.

1.3 Dynamics of the Universe

1.3.1 General Relativity

Einstein equations

So far we have just derived relations using the geometry of the Universe and the isotropy and homogeneity assumptions of the Cosmological Principle. The metric we have thus obtained in 1.4 contains a dynamical parameter, namely the scale factor $a(t)$, which changes with the time. In order to study the evolution of this scale factor and through him the dynamics of the Universe we have to use the General Relativity which will link the geometry to the contents of the Universe. To do so we have to solve the Einstein Field Equations (EFE):

$$G_{\mu\nu} \equiv R_{\mu\nu} - \frac{1}{2} g_{\mu\nu} R = \frac{8\pi G}{c^4} T_{\mu\nu} + \Lambda g_{\mu\nu} \tag{1.17}$$

where $G_{\mu\nu}$ is the Einstein tensor which is a combination of the Ricci tensor $R_{\mu\nu}$ and the Ricci scalar defined as $R \equiv g^{\mu\nu} R_{\mu\nu}$. They inform us about how much the space deviates from an Euclidean one. They are determined by the metric. $g_{\mu\nu}$ is the metric tensor and for an isotropic and homogeneous space it is the FLRW metric which can be written in the form given by 1.4. $T_{\mu\nu}$ is the stress-energy tensor and it is determined by the amount of matter and energy in the Universe. The Λ is the cosmological constant, which can be written either on the left (geometrical part) or right (matter-energy part) part. In this work we will consider the cosmological constant as being contained in the stress-energy tensor and then we will only focus on Dark Energy and not consider the case of modified gravity. In this case the cosmological constant can be rewritten as $T_{\mu\nu}^{(\Lambda)} = \frac{\Lambda c^4}{8\pi G} g_{\mu\nu}$.

If the left hand side of 1.17 is isotropic and homogeneous to respect the Cosmological Principle then the right hand side must be too. In the rest frame of the matter, the stress-energy momentum tensor has to be diagonal and its components can only vary with respect to the time and do not vary with space. These properties lead to consider the Universe and its components as perfect fluids where the stress-energy tensor is:

$$T_{\mu\nu} = (\rho + P)\, U_\mu\, U_\nu - P g_{\mu\nu} \tag{1.18}$$

where $\rho(t)$ is the energy density of the perfect fluid, $P(t)$ its pressure and U_ν the fluid velocity four-vector. In the rest frame of the fluid, $U_\nu = (1, 0, 0, 0)$ so the stress-energy tensor becomes:

$$T_\mu^\nu = diag(\rho(t), -P(t), -P(t), -P(t)) \tag{1.19}$$

Energy conservation

To find what we will later name the "energy conservation" we use the fact that the stress-energy tensor is conserved:

$$T^{\mu\nu}_{;\mu} \;=\; 0$$

The time component (i.e. $\mu = 0$) gives us:

$$T^{\nu}_{0;\nu} \;=\; \dot{\rho} \;+\; 3\left(\frac{\dot{a}}{a}\right)\;(\rho \;+\; P) \;=\; 0 \tag{1.20}$$

which is known as the energy conservation equation.

Friedmann equations

Given the FLRW metric 1.2, we can first derive completly the left hand side of the EFE 1.17. The non-zero component for the Ricci tensor and the RIcci scalar are:

$$\begin{cases} R_{00} = -3\,\dfrac{\ddot{a}}{a} & \text{(1.21a)} \\ R_{ij} = -\left[\dfrac{\ddot{a}}{a} + 2\left(\dfrac{\dot{a}}{a}\right)^2 + 2\dfrac{K}{a^2}\right] & \text{(1.21b)} \\ R = -6\left[\dfrac{\ddot{a}}{a} + \left(\dfrac{\dot{a}}{a}\right)^2 + \dfrac{K}{a^2}\right] & \text{(1.21c)} \end{cases}$$

Using 1.21a, 1.21c and 1.19 the $0-0$ component of the EFE is then:

$$\left(\frac{\dot{a}}{a}\right)^2 \;+\; \frac{K}{a^2} \;=\; \frac{8\pi G}{3}\,\rho \tag{1.22}$$

where ρ is the sum of all contributions to the energy density in the Universe.

Using 1.21b, 1.21c and 1.19 the $i-i$ component of the EFE is:

$$2\,\frac{\ddot{a}}{a} + \left(\frac{\dot{a}}{a}\right)^2 + \frac{K}{a^2} \;=\; -8\pi G P$$

if we use the equation 1.22 it follows:

$$\frac{\ddot{a}}{a} \;=\; -\,\frac{4\pi G}{3}\;(\rho \;+\; 3P)$$

To summarize, and using the Hubble parameter, $H \;=\; \frac{\dot{a}}{a}$, the dynamics of an isotropic and homogenous Universe is given the following set of equations:

$$\begin{cases} H^2 + \dfrac{K}{a^2} = \dfrac{8\pi G}{3}\rho & \text{(1.23a)} \\ \dfrac{\ddot{a}}{a} = -\dfrac{4\pi G}{3}\,(\rho + 3P) & \text{(1.23b)} \\ \dot{\rho} + 3H\,(\rho + P) = 0 & \text{(1.23c)} \end{cases}$$

The first equation is often called te Friedmann equation, the second one the Raychaudhuri equation and the last one the conservation of energy.

1.3.2 Energy density components in the Universe

Critical density

Before enumerating the different contributions to the total energy density of the Universe we introduce the concept of critical density. Dividing the Friedmann equation 1.23a by H^2 yields:

$$\frac{K}{a^2\,H^2} \;=\; \frac{8\pi G}{3\,H^2}\,\rho \;-\; 1$$

We see that there is a specific value of the energy density which implies that the curvature, K, vanishes. This is the critical energy density, $\rho_c \equiv \frac{3\,H^2}{8\pi G}$, which is defined by being the the energy density value required to have a flat Universe. The Friedmann equation can be re-written as:

$$\frac{K}{a^2\,H^2} \;=\; \frac{\rho}{\rho_c} \;-\; 1 \;\equiv\; \Omega \;-\; 1 \tag{1.24}$$

where we have inserted a new parameter, named the dimensionless energy density or density parameter: $\Omega \equiv \frac{\rho}{\rho_c}$.

The value of this parameter informs us on the curvature of the Universe as follows:

$$\begin{aligned}
&\Omega(t) < 1 \;\;\Rightarrow\;\; K < 0 \;\;\Rightarrow\;\; closed\;\; Universe \;/\; positively\;\; curved \\
&\Omega(t) = 1 \;\;\Rightarrow\;\; K = 0 \;\;\Rightarrow\;\; flat\;\; Universe \\
&\Omega(t) > 1 \;\;\Rightarrow\;\; K > 0 \;\;\Rightarrow\;\; open\;\; Universe \;/\; negatively\;\; curved
\end{aligned} \tag{1.25}$$

Contents of the Universe

We usually consider that the Universe is composed of 3 main components: matter, radiation and the vacuum energy contribution of dark energy.

- **Matter :** also called "dust" is composed of non-relativistic particles with a very low pressure, $P_m = 0$ and thus an equation of state $w_m = 0$. Commonly the matter energy density, Ω_m is splitted in 2 parts: baryonic matter Ω_b, though it includes also electrons, and the Cold Dark Matter Ω_c. The non-baryonic dark matter interacts only gravitationnaly and do not absorb nor emit radiation. Its existence is deduced from total mass estimates for galaxy rotation curves Rubin et al. [1980] or from the CMB anisotropies Planck Collaboration et al. [2015a] for instance. The 2015 Planck results have confirmed that the contribution of matter to the energy budget of the Universe is around 30%, with a baryonic contribution of around 5% and a Cold Dark Matter contribution of around 25% ($\Omega_m = 0.308$, $\Omega_b = 0.048$ and $\Omega_c = 0.258$).

- **Radiation :** is composed of relativistic particles and also includes neutrinos and photons, though they have a very small mass for the former or are massless for the latter their momenta exert a pressure which contributes to slow down the expansion of the Universe. The pressure is related to the density as $P_r = w_r \rho_r$ with the equation of state $w_r = \frac{1}{3}$

- **Dark Energy:** The results of 2 independent studies in 1998, Riess et al. [1998], and in 1999, Perlmutter et al. [1999], showed that the Universe's expansion is accelerating. Looking at the Equation 1.3.1 we see that an accelerating expansion requires $P < -\frac{\rho}{3}$, i.e. $w < -\frac{1}{3}$. We know very little about the physical properties of this component which has been named dark energy. The standard cosmological model considers dark energy as a vacuum energy with $P_{vac} = -\rho_{vac}$,i.e. $w_{vac} = -1$.

In cosmology we often refer to one of this component by using the corresponding density parameter: Ω_m for matter, Ω_r for radiation and Ω_Λ for the dark energy. The curvature can also be written in this form: $\Omega_K \equiv -\frac{K}{a^2 H^2}$. The Friedmann equation 1.23a becomes then:

$$1 = \Omega_m(t) + \Omega_r(t) + \Omega_\Lambda(t) + \Omega_K(t) \tag{1.26}$$

or with the energy densities notation:

$$H^2(t) = \frac{8\pi G}{3} \left[\rho_m(t) + \rho_r(t) + \rho_\Lambda(t)\right] - \frac{K}{a^2(t)} \tag{1.27}$$

The evolution of the energy densities are given by the energy conservation equation 1.23c:

$$\dot{\rho} = -3 \frac{\dot{a}}{a} (\rho + P)$$

In order to solve this equation we need a relation between the pressure and the energy density. In the form $P = P(\rho)$, this relation is named the equation of state. For our case, it takes the simple following form: $P = w\,\rho$, where w is the equation of state parameter (but often called the equation of state) and takes the values:

$$w = \begin{cases} 0 & for\ "pressureless"\ matter \\ 1/3 & for\ radiation \\ -1 & for\ the\ cosmological\ constant \end{cases} \tag{1.28}$$

The energy conservation equation can be written as:

$$\frac{\dot{\rho}}{\rho} = -3\,(1 + w)\,\frac{\dot{a}}{a} \tag{1.29}$$

which can be integrated analytically assuming w is constant:

$$\frac{\rho_i(t)}{\rho_i^{(0)}} = \left(\frac{a(t)}{a_0}\right)^{-3\,(1+w)} \begin{cases} \left(\frac{a(t)}{a_0}\right)^{-3} & for\ "pressureless"\ matter \\ \left(\frac{a(t)}{a_0}\right)^{-4} & for\ radiation \\ 1 & for\ the\ cosmological\ constant \end{cases} \tag{1.30}$$

where the subscript i represents either matter, radiation or the cosmological constant and the upperscript (0) the value today. In an expanding Universe, the radiation will dominate at early times, then matter and finally the cosmological constant.

Using the corresponding evolution of the density energies of 1.29 in the Friedmann equation 1.27 yields:

$$H^2(a) = \frac{8\pi G}{3}\left[\frac{\rho_m^{(0)}}{a^3} + \frac{\rho_r^{(0)}}{a^4} + \rho_\Lambda^{(0)}\right] - \frac{K}{a^2} \tag{1.31}$$

where the scale factor is taken to be unity today: $a_0 = 1$. In terms of the density parameter it becomes:

$$H^2(a) = H_0^2\left[\frac{\Omega_m^{(0)}}{a^3} + \frac{\Omega_r^{(0)}}{a^4} + \frac{\Omega_K^{(0)}}{a^2} + \Omega_\Lambda^{(0)}\right] \tag{1.32}$$

From this expression we can easily compute the Hubble parameter as a function of scale factor. To get the evolution with the redshift we just substitute the scale factor a by $\frac{1}{1+z}$.

In the following we will always assume a flat Universe, so $\Omega(t) = 1$ at all times. Furthermore, we will work in a matter - dark energy dominated Universe. It means that we will work after the radiation dominated era. In terms of redshift it means that we will work at redshift $z \lesssim 3200$, which allows us to neglect the radiation term to the energy contribution of the Universe. For a flat Universe, negelcting the radiation component and considering a cosmological constant with $w = -1$ the luminosity distance 1.16 using equations 1.3 and 1.5 becomes:

$$\begin{aligned} d_L(z) &= (1+z)\, d_{trans} = (1+z)\,\chi = (1+z)\int_{t_{em}}^{t_{obs}} \frac{c}{a(t)}\,\mathrm{d}t \\ &= (1+z)\int_0^z \frac{c}{H(z')}\,\mathrm{d}z' = (1+z)\,\frac{c}{H_0}\int_0^z \left[\Omega_m^{(0)}\,(1+z)^3 + \Omega_\Lambda^{(0)}\right]^{-1/2}\,\mathrm{d}z' \end{aligned} \tag{1.33}$$

The left hand side of this equation is an observable, for instance obtained with Type Ia Supernovae observations, and the right hand side depends on the theoretical description of the Universe contents.

Chapter 2.

Dark Energy

2.1 Cosmological constant

2.1.1 Vacuum energy

The most simple explanation is given by a uniform vacuum energy filling space with a negative pressure. The equation of state is $w = -1$. The problem known as the cosmological constant is that the required vacuum energy is many orders of magnitude smaller than the expected in the standard model of particle physics.

2.1.2 Constant eos different from -1

If we do not follow the parametrisation $w_{dark\ energy} = -1$, the first model to check is the one with a constant equation of state and confront it with data to check whether it is consistent with the value of -1.

In this case the conservation of energy reads:

$$\frac{\rho_{DE}(t)}{\rho_{DE}^{(0)}} = \left(\frac{a(t)}{a_0}\right)^{-3\ (1+w)} \tag{2.1}$$

which implies the following modification of the Friedman equation:

$$H^2(z) = H_0^2 \left[\Omega_m^{(0)}\ (1+z)^3 + \Omega_{DE}^{(0)}\ (1+z)^{3(1+w)}\right] \tag{2.2}$$

2.2 Dynamical Dark Energy

The next step is to study a varying equation of state. One way to explain the Dark Energy, whose effects are detectable only on large scales, is to introduce some modification to gravity

on large scales. However we will not discuss it and only focus on Dark Energy resulting from a cosmological scalar field in this work.

2.2.1 The Chevallier-Polarski-Linder model

Before introducing the scalar fields theory let us introduce the most common used parametrisation of varying Dark Energy. It consists in allowing a small dependence on the redshift for the equation of state. First introduced by Chevalier and Polarski Chevallier and Polarski [2001] they considered the following toy model:

$$w(a) \;=\; -1 \;+\; \alpha \;+\; \beta(1 \;-\; \frac{a}{a_0}) \tag{2.3}$$

where α measures the departure today from an equation of state corresponding to a cosmological constant, while the parameter β measures the variation in time of the equation of state.
A couple of years later Linder Linder [2003] proposed the following parametrisation:

$$w(a) \;=\; w_0 \;+\; w_a(1 \;-\; a) \Leftrightarrow\; w(z) \;=\; w_0 \;+\; w_a\,\frac{z}{1+z} \tag{2.4}$$

This is just an other formulation of the expresssion given by Chevallier and Polarski [2001]. This relation, known as the Chevallier-Polarski-Linder (CPL) parametrisation, is very used in cosmology for several reasons: its simplicity, only a 2-parameter space, it is equal to a constant at $z = 0$ and bounded for $z \to \infty$.
With this parametrisation the energy conservation equation is:

$$\frac{\rho_{CPL}(a)}{\rho^{(0)}_{CPL}} \;=\; exp\left(\int\,(\,-\,3\,(1 + w_0 + w_a(1-a)))\frac{da}{a}\right) \tag{2.5}$$

which implies the following modification of the Friedman equation:

$$H^2(z) \;=\; H_0^2\,\left[\Omega_m^{(0)}\,(1+z)^3 \;+\; \Omega_{DE}^{(0)}\,(1+z)^{3\,(1+w_0+w_a)}\,e^{-3\,w_a\frac{z}{1+z}}\right] \tag{2.6}$$

Ths parametrisation is considered to be relatively accurate until $z < 2$.

2.2.2 Scalar fields

Since the discovery of the Higgs scalar field at the CERN's Large Hadron Collider Aad et al. [2015], we know that scalar fields exist in the Universe. As scalar fields arise naturally in particle physics and string theory it is interesting to check whether they can act like Dark Energy with a time variation of the equation of state. Several kind of scalar have been tested, such as quintessence, phantom field, K-essence, ghost condensate or tachyon. In this work we will consider the archetype of these which is the quintessence scalar field and also the phantom scalar field which allows the equation of state of Dark Energy to be smaller than -1.

Quintessence

Quintessence is described by a scalar field ϕ minimally coupled to gravity. This class of scalar field is restricted to $w > -1$. The action for a quintessence scalar field is:

$$S \;=\; \int \mathrm{d}^4x\,\sqrt{-g}\;\left[-\frac{1}{2}\,(\nabla\phi)^2 \;-\; V(\phi)\right] \;+\; S_m \tag{2.7}$$

where the kinetic energy of the field can be rewritten as $(\nabla\phi)^2 \;=\; g^{\mu\nu}\partial_\mu\phi\partial_\nu\phi$, and $V(\phi)$ is the potential of the field. S_m represents the matter action, here we consider only non-relativistic matter with an equation of state $w_m = 0$.

In a flat FLRW metric the variation of the action 2.7 with respect to the field gives the evolution of the field with the time:

$$\ddot{\phi} \;+\; 3H\dot{\phi} + \frac{d\,V}{d\,\phi} \;=\; 0 \tag{2.8}$$

Considering a perfect fluid the density and pressure of the field are given by:

$$\rho_\phi \;=\; \frac{1}{2}\dot{\phi}^2 \;+\; V(\phi) \tag{2.9}$$

$$P_\phi \;=\; \frac{1}{2}\dot{\phi}^2 \;-\; V(\phi) \tag{2.10}$$

The equation of state follows:

$$w_\phi \;=\; \frac{P_\phi}{\rho_\phi} \;=\; \frac{\dot{\phi}^2 \;-\; 2V(\phi)}{\dot{\phi}^2 \;+\; 2V(\phi)} \tag{2.11}$$

The Friedman and Raychaudhuri equations are thus:

$$\begin{cases} H^2 = \dfrac{8\pi G}{3}(\rho_m + \rho_\phi) & \text{(2.12a)} \\ \dfrac{\ddot{a}}{a} = -\dfrac{4\pi G}{3}\,(\rho_m + \rho_\phi + 3P_\phi) & \text{(2.12b)} \end{cases}$$

Phantom field

The action for a phantom scalar field is:

$$S \;=\; \int \mathrm{d}^4x\,\sqrt{-g}\;\left[\frac{1}{2}\,(\nabla\phi)^2 \;-\; V(\phi)\right] \;+\; S_m \tag{2.13}$$

where the only difference with the quintessence field is the sign of the kinetic term.

In a flat FLRW metric the field evolution is given by:

$$\ddot{\phi} \;+\; 3H\dot{\phi} - \frac{d\,V}{d\,\phi} \;=\; 0$$

Considering a perfect fluid the density and pressure of the field are given by:

$$\rho_\phi \;=\; -\frac{1}{2}\dot{\phi}^2 \;+\; V(\phi) \tag{2.14}$$

$$P_\phi \;=\; -\frac{1}{2}\dot{\phi}^2 \;-\; V(\phi) \tag{2.15}$$

which leads to the equation of state:

$$w_\phi \;=\; \frac{P_\phi}{\rho_\phi} \;=\; \frac{\dot{\phi}^2 \;+\; 2V(\phi)}{\dot{\phi}^2 \;-\; 2V(\phi)} \tag{2.16}$$

Autonomous system

In order to study the dynamical evolution of the dynamical dark energy, resulting of a scalar field, and matter we have to solve the following system of 3 equations:

$$\begin{cases} H^2 = \dfrac{8\pi G}{3}(\rho_m + \rho_\phi) & \text{(2.17a)} \\ \dfrac{\ddot{a}}{a} = -\dfrac{4\pi G}{3}\left(\rho_m + \rho_\phi + 3P_\phi\right) & \text{(2.17b)} \\ \ddot{\phi} + 3H\dot{\phi} + \dfrac{dV}{d\phi} = 0 & \text{(2.17c)} \end{cases}$$

where we have assumed a flat Universe and neglected the radiation contribution. We rewrite the equations using the standard new variables:

$$\begin{aligned} x \;&= \frac{\phi'}{\sqrt{6}M_{pl}} \\ y \;&= \frac{\sqrt{V}}{\sqrt{3}HM_{pl}} \\ \lambda \;&= -\,M_{pl}\,\frac{V_{,\phi}}{V} \\ \Gamma \;&= V\,\frac{V_{,\phi\phi}}{V_{,\phi}^2} \end{aligned}$$

where the prime is the derivative with respect to $N \equiv ln(a)$, i.e.$\phi' = d\phi/(da/a)$. The subscript $,\phi$ denotes a derivative with respect to ϕ and $,\phi\phi$ a second derivative with respect to ϕ. $M_{pl} = \frac{1}{\sqrt{8\pi G}}$ is the Planck mass.

In terms of these variables we can write the density parameter of the field and the equation of state of the field as::

$$\begin{aligned} \Omega_\phi \;&= x^2 + y^2 \\ \gamma \;&\equiv 1 \;+\; w \;= \frac{2x^2}{x^2 + y^2} \end{aligned}$$

In terms of Ω_ϕ,γ and λ the autonomous system becomes Kumar et al. [2015]

$$\begin{cases} \gamma' = -3\gamma(2-\gamma) + \lambda(2-\gamma)\sqrt{3\gamma\Omega_\phi} & \text{(2.18a)} \\ \Omega'_\phi = 3(1-\gamma)\Omega_\phi(1-\Omega_\phi) & \text{(2.18b)} \\ \lambda' = -\sqrt{3}\lambda^2(\Gamma - 1)\sqrt{\gamma\Omega_\phi} & \text{(2.18c)} \end{cases}$$

This system is solved starting from initial conditions at decoupling, around $a \simeq 10^{-3}$, and evolves towards today. The initial conditions at the decoupling are taken to be (γ_i,$\Omega_{\phi i}$,λ_i), where $\Omega_{\phi i}$ has to be small Pettorino et al. [2013] and constrained to be $\Omega_\phi(z \simeq 1090) < 0.049$ at the last scattering surface Joudaki [2013]. As a first approach we can adopt the values given in Kumar et al. [2015] which are around 10^{-9} to recover current value of Ω_ϕ today.

If we consider a thawing model, the field is frozen due to the Hubble friction at early times, so the equation of state is close to -1, we then choose $\gamma_i = 10^{-4}$ as in Kumar et al. [2015]. However if we consider the freezing class of model, the field is not initially frozen and then γ_i can be chosen as a free parameter.

For both freezing and thawing models the initial slope of the potential, λ_i, is a parameter of the simulation where $\lambda_i = 0$ implies a constant potential and thus corresponds to the cosmological constant. If $\lambda_i \neq 0$ it quantifies the departure from a cosmological constant.

As the main objective to use these scalar fields is to check whether the observations of the alpha fine structure would help to distinguish between a thawing and a freezing model (see definition in next part), we will first focus on 2 standards potentials which are the power law and the exponential potentials:

$$\begin{aligned} V(\phi) &= K\ \phi^{\,p} \\ V(\phi) &= e^{n\ \phi} \end{aligned} \tag{2.19}$$

where K, p and n are real constants.

2.2.3 Definition of Freezing and Thawing scalar fields

Quintessence models can be separated in 2 classes, called "thawing" and "freezing", according to their evolution in the (w,$\frac{dw}{dlna}$) phase Caldwell and Linder [2005]. For both classes the field evolves down its potential towards a zero minimum, however the field is acelerating at late-time for thawing models and decelerating for freezing ones.

Considering the equation of motion for the field 2.8, we see that the evolution in the (w,$\frac{dw}{dlna}$) phase is determined by the driving term $\dfrac{dV}{d\phi}$ and the damping term $3H\dot{\phi}$, also called the Hubble damping, whose effects are opposite.

In the case of thawing models the field has been frozen by the Hubble damping at a value different from its minimum until recently where it started to roll down to the the minimum. At early time the equation of state of the field is $w_\phi \simeq -1$ and moves towards less negative value, then locating in the region $\frac{dw}{dlna} > 0$.

Freezing models are characterised by having $w_\phi > -1$ initially and then they evolve towards

$w_\phi \simeq -1$, situating then in the region $\frac{dw}{dlna} < 0$. This happens when the field was initally rolling down to its minimum before the expansion of the Universe takes place and damps the field.

Some upper and lower bounds for both models were calculated and simulated by Caldwell and Linder [2005] as shown in figure 2.1.

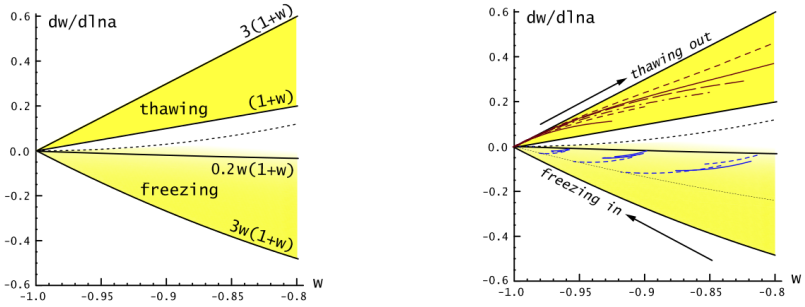

Figure 2.1: *Left:* The $(w, \frac{dw}{dlna})$ phase space occupied by thawing and freezing fields is indicated by the shaded regions from Caldwell and Linder [2005]. *Right:* The evolutionary tracks in $(w, \frac{dw}{dlna})$ phase space are shown for a variety of particle physics models of scalar fields from Caldwell and Linder [2005]

One goal of this work is to study whether the fine structure constant measurements might help to distinguish between these 2 classes as it allows to have some information up to a redshift of around 4.

Chapter 3.

Cosmological Observables

3.1 Supernovae Ia

Decades of Supernovae observations lead to the classification of these extremely luminous explosions into two main types which are named type I and II depending on whether their spectra contains Hydrogen (type II) or not (type I). These 2 categories are then also split in subcategories. The type I supernovae are named Sne Ia if their spectrum contain silicium. If not they are ranged in Ib or Ic whether they contain or not Helium. Here we are interested only in the SN Ia.

A Type Ia Supernova is thought to occur in a binary system, where one of the star is a white dwarf. A white dwarf is the remnant of a low-mass star and has ceased nuclear fusion. However, in a binary system it can accrete some mass from its companion Nomoto et al. [1984], and when it approaches the Chandrasekar limit of $1.4M_{\odot}$, carbon re-ignites at the center Hillebrandt and Niemeyer [2000]. Since the electrons in the white dwarf are a degenerated gas their pressure is almost independent of the temperature. As a consequence the increase in temperature is not compenstaed by an increase of the outward pressure and then further mass accretion result in higher and higher core temperature. At some point the energy generated by the nuclear reactions in the core can not be driven away anymore leading to a thermonuclear runaway process beginning with the burning of the carbon and oxygen and ending in nickel and cobalt. The explosion is very bright, can be as bright as the host galaxy, which makes Type Ia SNe suitable to probe the far Universe. A more detailed explanation of the explosion of Type Ia Supernovae can be read in Mazzali et al. [2007].

Because white dwarfs have nearly the same mass before exploding, and are considered to follow the same explosion mechanism, they were considered as excellent candidates for standard candles. A “standard candle” defines any distinguishable class of astronomical objects of known

intrinsic brightness that can be identified over a wide distance range. In principle, it can be used to determine quite easily the expansion history of the Universe.

As shown in Figure 3.1 the light curves of Type Ia Supernova have a similar behaviour but their intrinsic luminosity can vary over a factor of 3. The peak luminosity is determined by the amount of ^{56}Ni produced in the explosion Arnett [1982], which for a fully burned white dwarf is about 0.6 solar masses. Though some white dwarfs may not be completely burned, and the explosion mechanism is still not fully understood, the majority of SNe Ia do exhibit similar light curves and one can calibrate them in order to obtain a well-known correlation between the maximum brightness and rate of decline of the light curve discovered by Phillips in 1993 Phillips [1993]. The brighter SNe Ia have a slower decline of their light curves whereas fainter ones have the fastest decline.

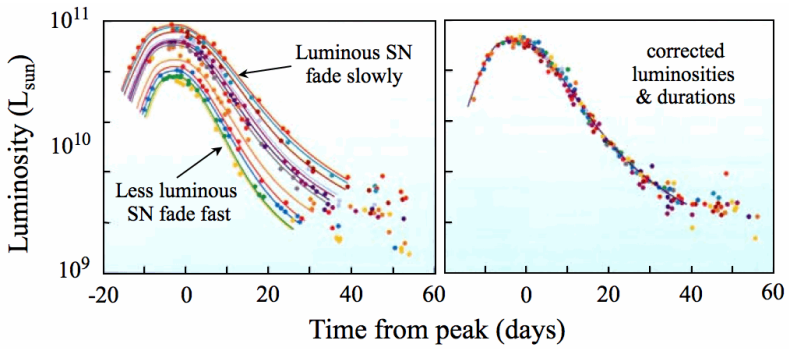

Figure 3.1: Type Ia Supernova light curves. There is a duration-brightness relation for supernovae type Ia (left). Once calibrated, one obtains the true luminosity (right). Source: https://www.astro.virginia.edu/class/whittle/astr553/Topic16/t16_SNIa_distances.html

Once calibrated the luminosity is considered to be the same and we can then use it to determine the distance at which the explosion occured.

So even if Type Ia SNe are not typical standard candles we can use them as "calibrated candles" in order to obtain information of the history of the Universe. At present time it allows us to measure distances with an accuracy of 1%.

What we observe is the apparent magnitude, $m(z)$, which relates to $d_L(z)$ as:

$$m(z) = 5\, log_{10}\left(\frac{d_L(z)}{1Mpc}\right) \; + \; M \; + \; 25 \tag{3.1}$$

where the M is the absolute magnitude of the source.

Or by expressing the luminosity distance:

$$d_L(z) = 10^{(\frac{m(z)-M-25}{5})} \tag{3.2}$$

In this work we are using the Union2.1 Type Ia supernovae data Suzuki et al. [2012] containing 580 measurements.

3.2 Hubble parameter measurements

Up to now there are two typical methods to measure the Hubble parameter $H(z)$: the differential age method and the Baryonic Acoustic Oscillations (BAO) along the line-of-sight direction from the spectroscopic galaxy sample. The differential age method is based on observations of passively evolving galaxies, and using the definition of the Hubble parameter:

$$H \equiv \frac{\ddot{a}}{a} = -\frac{1}{1+z}\frac{dz}{dt_{ct}}$$

where dt_{ct} is the variation of the cosmic time due to a small change in the redshift dz. See Jimenez and Loeb [2002] and Simon et al. [2005] for more details.

While standard candles, most notably Type Ia supernovae, opened the era of accurate extragalactic distance measurements, the standard rulers, in particular the BAO, can also play a role in determining the distances. A "standard ruler" in Cosmology is an object of a known size at a single redshift, or a population of objects at different redshifts whose size changes in a well-known way with redshift.

The BAO in the radial and tangential directions provide measurements of the Hubble parameter and angular diameter distance respectively. We do not intent to make a detailed review of the radial BAO technique, for more details on this method see Gaztanaga et al. [2009].

In this work we are using the compilation of 28 independent measurements of the Hubble parameter between redshifts 0.07 and 2.3 given in Farooq and Ratra [2013] and shown in Table 3.1.

3.3 Redshift drift

The redshift drift, also known as the Sangae-Loeb Test, is the temporal measurement of the redshift variation for an object following the Hubble flow. Since the Universe expands, the redshift measurement of distant sources at different times is a direct probe of this expansion using relatively simple and well-understood physics. If one needs to combine spectra from different lines of sight, the only necessary assumptions are the large scale isotropy and homogeneity. The first person who suggested this technique was Allan Sandage in 1962 (Sandage [1962]), unfortunately the observational facilities at that time were sensitive to detect a small redshift variation only on a time interval of 10^7 years. As the technology improved, A. Loeb reconsidered this idea in

Table 3.1: Hubble Parameter versus redshift data

z	H(z) $(km.s^{-1}.Mpc^{-1})$	σ_H $(km.s^{-1}.Mpc^{-1})$	Reference
0.07	69	19.6	Zhang et al. [2014]
0.1	69	12	Simon et al. [2005]
0.12	68.6	26.2	Zhang et al. [2014]
0.17	83	8	Simon et al. [2005]
0.179	75	4	Moresco et al. [2012]
0.199	75	5	Moresco et al. [2012]
0.2	72.9	29.6	Zhang et al. [2014]
0.27	77	14	Simon et al. [2005]
0.28	88.8	36.6	Zhang et al. [2014]
0.35	76.3	5.6	Chuang and Wang [2013]
0.352	83	14	Moresco et al. [2012]
0.4	95	17	Simon et al. [2005]
0.44	82.6	7.8	Blake et al. [2012]
0.48	97	62	Stern et al. [2010]
0.593	104	13	Moresco et al. [2012]
0.6	87.9	6.1	Blake et al. [2012]
0.68	92	8	Moresco et al. [2012]
0.73	97.3	7	Blake et al. [2012]
0.781	105	12	Moresco et al. [2012]
0.875	125	17	Moresco et al. [2012]
0.88	90	40	Stern et al. [2010]
0.900	117	23	Simon et al. [2005]
1.037	154	20	Moresco et al. [2012]
1.30	168	17	Simon et al. [2005]
1.43	177	18	Simon et al. [2005]
1.53	140	14	Simon et al. [2005]
1.75	202	40	Simon et al. [2005]
2.3	224	8	Busca et al. [2013]

1998 (Loeb [1998]) and suggested to use spectroscopc redshifts measurements of the Lyα forest of distant quasars (QSOs). With a variation estimated of a few m/s per century, this should be

detected in the next decades with for instance the High Resolution Spectrograph (HIRES) for the European-Extremly Large Telescope (E-ELT).

This method is promising because it probes a redshift range $2 < z < 5$ which is so far very poorly probed. For instane, Type Ia SNe and weak lensing observations probes at lower redshift and the CMB at much higher redshift.

In this work it will be used as a consistency test in comparison of the alpha measurements when used to constrain dark energy.

Let us now derive the expresion of the redshift drift following Corasaniti et al. [2007]. If we consider a source at a redshift z, this redshift measured by the observer can be expressed with equation 1.9 as :

$$1 + z(t_0) = \frac{a(t_0)}{a(t_s)} \tag{3.3}$$

where t_0 is the time of observation and t_s is the time of emission of the electromagnetic wave.

If we consider a second wave emitted at a time $t_s + \Delta t_s$ and observed at $t_0 + \Delta t_0$ the observed redshift becomes:

$$1 + z(t_0 + \Delta t_0) = \frac{a(t_0 + \Delta t_0)}{a(t_s + \Delta t_s)} \tag{3.4}$$

The redshift difference between the two observations is then:

$$z(t_0 + \Delta t_0) - z(t_0) = \frac{a(t_0 + \Delta t_0)}{a(t_s + \Delta t_s)} - \frac{a(t_0)}{a(t_s)} \tag{3.5}$$

In the limit $\Delta t \ll t$ the scale factor for the second wave can be expressed as a Taylor expansion of order 1, $a(t + \Delta t) \simeq a(t) + \dot{(a)}\Delta t$. Using the relation 1.8, $\frac{\Delta t_0}{\Delta t_s} = \frac{a(t_0)}{a(t_s)}$, the difference in the observed redshift can be then approximated as in Corasaniti et al. [2007]:

$$\Delta z \simeq \left(\frac{\dot{a}(t_0) - \dot{a}(t_s)}{a(t_s)} \right) \Delta t_0 \tag{3.6}$$

This redshift shift is more conveniently expressed in term of a spectroscopic velocity shift Δv, using the relation:

$$\frac{\Delta v}{c} \equiv \frac{\Delta z}{1 + z} \tag{3.7}$$

where c is the speed of light in vacuum.

Considering a flat Friedmann-Robertson-Walker universe dominated by matter and dark energy, setting ($a(t_0) = 1$ and using the Friedmann equation 2.2 one can express Δv as follows:

$$\frac{\Delta v}{c} = H_0 \Delta t_0 \left[1 - \frac{E(z)}{1 + z} \right] \tag{3.8}$$

where H_0 is the Hubble constant and $E(z) = \frac{H(z)}{H_0} = \sqrt{\Omega_m^0 (1 + z)^3 + \Omega_\Lambda}$ in our case.

According to some Monte-Carlo simulation performed for the high resolution spectrograph E-ELT CODEX (now HIRES), the error on the measured spectroscopy velocity shift an be expressed

as Bonifacio et al. [2010]:

$$\sigma_{\Delta v} = 1.35 \frac{2370}{S/N} \sqrt{\frac{30}{N_{QSO}}} \left(\frac{5}{1 + z_{QSO}} \right)^{x} cm.s^{-1} \tag{3.9}$$

where S/N is the signa-to-noise ratio, N_{QSO} the number of observed quasars (QSO: Quasi-Stellar Object, also named Quasar) and z_{QSO} their redshift and

$$x = \begin{cases} 1.7 & if \;\; z_{QSO} < 4 \\ 0.9 & if \;\; z_{QSO} > 4 \end{cases} \tag{3.10}$$

Chapter 4.

Detection of a varying fine structure constant

The fine structure constant α measures the strength of the electromagnetic interaction. It can be expressed as:

$$\alpha = \frac{e^2}{2\epsilon_0 hc} \tag{4.1}$$

where e is the elementary charge, ϵ_0 the permittivity of free space, h the Planck constant and c the speed of light in vacuum.

Different type of experiments enable to measure α at different cosmological time, such as the atomic clocks, the Oklo natural nuclear reactor, the meteoritic abundance, the CMB anisotropies, the Big Bang Nucleosynthesis and the Quasar absorption spectra. All these experiments are reviewed in Uzan [2011]. In this work we will only describe qualitatively the Quasar (QSO) absorption spectra.

4.1 Quasar absorption spectra

The observation of distant astrophysical objects such as Quasar absorption spectra gives access to the atomic energy levels at the time and position of absorption. As the transition between atomic energy levels depend on α, this provides a method to measure α at different location and time. Along the line of sight, the QSO emission spectra when crossing a cloud will contain some absorption lines depending of the atoms present in these clouds. By studying these transition lines we can measure α. As the expansion of the Universe shifts all the spectrum, one cannot study only one single transion line, thus the idea is to compare several transition lines of different atoms. There are several methods such as the alkali doublet (AD) focusing on the fine structure

alkali doublet, the many-multiplet (MM) using correlations between various transitions in different atoms, the single ion differential alpha measurement (SIDAM) using different transitions of a single ion.

For the Alkali Doublet method the separation in the wavelength of transitions is proportional to α^2. For the more general Many Multiplet method the observed wavenumber of a given transition, i, depends on α as:

$$\omega_i(z) \equiv \omega_i(0) + q_i \left[\left(\frac{\alpha(z)}{\alpha(0)} \right)^2 - 1 \right] \tag{4.2}$$

where $\omega_i(0)$ is the wavenumber measured in laboraty for the transition i, $\alpha(z)$ the measured value of the fine structure constant at absorption redshift z and $\alpha(0)$ the present value of α. q is the sensitivity coefficient which determines how sensitive the transition i is to a change in α. The q coefficients are calculated using quantum many-body methods simulations Dzuba et al. [1999]. These coefficients are different for all the species, for some transitions q is approximately zero and these transitions are called *Anchor transitions*, transitions with $q > 0$ are called *positive shifters* and transisitons with $q < 0$ are called *negative shifters*. The "quality" of the selected transitions do not depend on the absolute value of q but on the differences in q between the transitions.

We refer to Uzan [2011] for a more detailed review of all of these methods.

In this work we will use 3 different data sets.

- The first one is composed of 143 spectroscopic measurements of α from Murphy et al. [2004] observed with the Keck telescope in Hawai over a redshift range $0.2 < z < 4.2$ and obtained by 3 separate groups. The result is that α may have benn smaller in the past at the 5σ level. The weighted mean is $\frac{\Delta\alpha}{\alpha}$=(-0.57 $\pm$ 0.11) $\times 10^{-5}$. The measurements can be seen in the Figure 4.1.

We will refer this data set as the Keck dataset.

- The second data set is composed of 153 spectroscopic measurements of α from Webb et al. [2011a], King et al. [2012] observed with the VLT telescope in Chile over the redshift range $0.2 < z < 3.2$. The weighted mean is $\frac{\Delta\alpha}{\alpha}$=(0.21 $\pm$ 0.12) $\times 10^{-5}$ King et al. [2012]. The measurements can be seen in the Figure 4.1.

We will refer this data set as the VLT dataset.

To minimise the influence of systematics we will use the two data sets together and refer to it as Keck+VLT.

- We will also use a smaller and recent dataset of 11 measurements compiled by Martins and

Pinho [2015]. This sample combines measurements from Keck and the VLT over a small redshift range $1.08 < z < 1.84$ but in counterpart with low uncertainties on the measurements. This sample can also be seen on the right plots of the Figure 4.1. We will refer this data set as the "small" data set.

The study of systematics errors performed by Murphy Murphy et al. [2001] lead to the conclusion that known systematics do not significantly affect the measurements. However, some still unknown systematics might be not negligible.

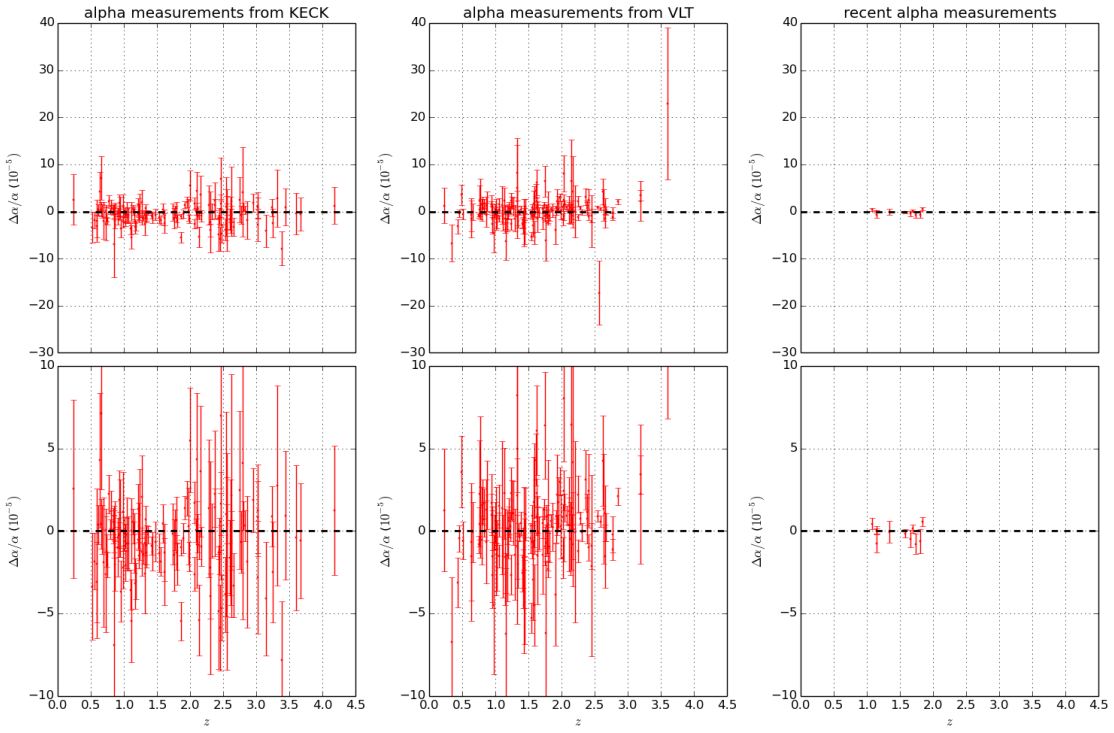

Figure 4.1: Values of $\frac{\Delta\alpha}{\alpha}$ and their total uncertainties for the Keck, VLT and small samples respectively on the left plot, middle plot and right plot. The bottom panels are just a zoom in the range $-10^{-4} < \frac{\Delta\alpha}{\alpha} < 10^{-4}$

4.2 Theoretical background

In the previous sections we have described how we can detect a variation of the fine structure constant. In this section we will describe how the fine structure constant can be linked to the equation of state of Dark Energy.

In this work we study the standard class of models where the variation of the fine-structure constant is linearly proportional to the displacement of a scalar field. Moreover we will assume that this scalar field is also responsible for the acceleration of the Universe Dvali and Zaldar-

riaga [2002], Chiba and Kohri [2002], Anchordoqui and Goldberg [2003], Copeland et al. [2004], Marra and Rosati [2005].

The dynamical scalar field is expected to be coupled to the rest of the theory, unless a (still unknown) symmetry suppresses this coupling Carroll [1998]. We will assume in the following that this is the case.

We will study a coupling between the scalar field ϕ and the electromagnetic sector. We take ths coupling to be:

$$\mathcal{L}_{\phi F} = -\frac{1}{4} B_F(\phi) F_{\mu\nu} F^{\mu\nu} \,. \tag{4.3}$$

where ζ is the coupling constant and the gauge kinetic function $B_F(\phi)$ can be taken as linear with a good approximation Nunes and Lidsey [2004], Avelino et al. [2006],

$$B_F(\phi) = 1 - \zeta\kappa(\phi - \phi_0) \,, \tag{4.4}$$

(with $\kappa^2 = 8\pi G$). This form of the gauge kinetic function can be seen as the first term of a Taylor expansion, which is a good approximation in the case of a slowly varying field at low redshifts. It correponds to the original Bekenstein proposal Bekenstein [1982]. See Marra and Rosati [2005] for a review of different gauge kinetic funtions.

The constraints on the coupling ζ are discussed in the next section.

The effective fine structure constant depends on the value of ϕ as

$$\alpha = \frac{\alpha_0}{B_F(\phi)} \tag{4.5}$$

With these assumptions the evolution of α can be written

$$\frac{\Delta\alpha}{\alpha} \equiv \frac{\alpha - \alpha_0}{\alpha_0} = B_F^{-1}(\phi) - 1 = \zeta\kappa(\phi - \phi_0) \,, \tag{4.6}$$

Now we want to explicitly relate the evolution of α to that of dark energy.

As we have seen before, for a flat Friedmann-Robertson-Walker Universe with a quintessence scalar field (using Eq.2.16)

$$\dot{\phi}^2 = (1 + w_\phi(z))\rho_\phi \tag{4.7}$$

and the fraction of the dark energy density is defined as

$$\Omega_\phi(z) \equiv \frac{\rho_\phi(z)}{\rho_{\rm tot}(z)} \simeq \frac{\rho_\phi(z)}{\rho_\phi(z) + \rho_m(z)} \,, \tag{4.8}$$

where in the lest step we have neglected the contribution from radiation (since we will be interested in low redshifts, $z < 5$, where it is indeed negligible). The evolution of the scalar field can

be now expressed in terms of the dark energy properties Ω_ϕ and w as Avelino et al. [2006], Nunes et al. [2009]

$$1 + w_\phi = \frac{(\kappa\phi')^2}{3\Omega_\phi}\,, \tag{4.9}$$

with the prime denoting the derivative with respect to the logarithm of the scale factor. We finally obtain

$$\frac{\Delta\alpha}{\alpha}(z) = \zeta \int_0^z \sqrt{3\Omega_\phi(z)\,(1 + w_\phi(z))}\frac{dz'}{1+z'}\,. \tag{4.10}$$

where we have chosen the positive root of the solution as we expect the field to roll down its potential.

The above relation assumes a quintessence scalar field, but the argument can be repeated for phantom fields, leading to

$$\frac{\Delta\alpha}{\alpha}(z) = -\zeta \int_0^z \sqrt{3\Omega_\phi(z)\,|1 + w_\phi(z)|}\frac{dz'}{1+z'}\,; \tag{4.11}$$

the change of sign comes from the fact that one expects the phantom field to roll up the potential rather than down.

4.3 Constraints

In this part we summarise the different constraints on the variation of alpha or the coupling factor given from various experiment in Table 4.1. These experiments give different measurements of α at different redshift. A detailed review of these experiments was made by the work of Uzan Uzan [2011].

We will especially use the constraint from atomic clocks as it is the tightest one. This constraint on the current drift of α from the work of Rosenband et al. [2008] an be written as:

$$\frac{1}{H_0}\frac{\dot{\alpha}}{\alpha} = (-2.2 \pm 3.2) \times 10^{-7} \tag{4.12}$$

Table 4.1: Different constraints on $\frac{\Delta\alpha}{\alpha}$ and ζ

Experiment	Redshift	Constraint	References
Atomic clocks	z=0	$\left\|\frac{\dot{\alpha}}{\alpha}\right\| \lesssim 1.6 \times 10^{-17} yr^{-1}$	Rosenband et al. [2008]
Oklo natural reactor	z=0.14	$\left\|\frac{\Delta\alpha}{\alpha}\right\| \lesssim 10^{-7}$	Damour and Dyson [1996] Fujii et al. [2000] Olive et al. [2002]
Meteoritic abundance (Decay rate $^{187}Re \rightarrow ^{187} Os$)	z=0.45	$\left\|\frac{\Delta\alpha}{\alpha}\right\| \lesssim 10^{-7}$	Olive et al. [2002]
Cosmic Microwave Background Radiation	z=10^3	$\left\|\frac{\Delta\alpha}{\alpha}\right\| \lesssim 10^{-2}$	Avelino et al. [2001]
Big Bang nucleosynthesis	z=$10^8 - 10^{10}$	$\left\|\frac{\Delta\alpha}{\alpha}\right\| \lesssim 2 \times 10^{-2}$	Bergstrom et al. [1999] Nollett and Lopez [2002] Ichikawa and Kawasaki [2002]
Equivalence principle tests	/	$\|\zeta\| \leq 10^{-3}$	Uzan [2011]

Chapter 5.

Parametric Analysis

In this part, we will first employ a quantitative approach where we have simulated some freezing and thawing models to study the evolution of $w(z)$ and $\alpha(z)$. Given the accuracy of future sources of high-quality data such as ESPRESSO Pepe et al. [2013] and ELT-HIRES Liske et al. [2014], it will give us a first idea of how good the alpha measurements might be to distinguish these 2 models.
We will then perform a more detailed analysis using a Monte Carlo Markov Chain algorithm mainly to constrain the coupling factor ζ. The constraints on the equation of state of dark energy and some cosmological parameters will also be studied.
Finally, we will select two quintessence models corresponding to a freezing one and a thawing one and study the constraints that alpha measurements may bring to the parameters in the potentials used.

5.1 First (quantitative) approach

In this section we perform a quantitative analysis by simulating various families of freezing and thawing models. We have used a modified version of the code of Marsh et al. [2014]. We will first describe the method developped by Marsh et al. [2014] and then the modifications we have made. The aim of the first part is to find a model representative of both classes. Once it is done we will study the corresponding evolution of the fine structure constant and finally compare it with the redshift drift method.

5.1.1 Definition of models

The quintessence models initially implemented by Marsh et al. [2014] have a potential described by:

$$V(\phi) = AM_P^2 M_H^2 P(\phi) \tag{5.1}$$

where $M_P = 1/\sqrt{8\pi G}$ is the reduced Planck mass and $M_H = 100km.s^{-1}Mpc^{-1}$ is the Hubble rate, and A is an overall scale.

$P(\phi)$ represents a dimensionless potential and takes the form:

$$P(\phi) = c_\Lambda \xi_\Lambda + f(\phi) + \sum_{n_{min}}^{n_{max}} c_n \xi_n b_n(\phi) \tag{5.2}$$

where c_Λ is equal either to 0 or 1 and enables to switch on or off the "cosmological constant" term. $\xi_{\Lambda,n}$ are random variables distributed with a Normal Gaussian $\mathcal{N}(0,1)$, c_n is a constant. $f(\phi)$ is the leading contribution of the potential and $b_n(\phi)$ is a basis function. All the potenetials are truncated at the same order, n_{max} and the first order n_{min} is model specific.

One can choose a model among the following ones:

- *Kac and Weyl:* random polynomial potentials without any physical motivation. Tao and Vu [2013]

- *Monomial:* integer power law potential with only one order ϕ^N. The main reason of using this kind of models is its simplicity.

- *Effective Field Theory (EFT):* potential subject to the rules of effective field theory. The potential is parametrised as a leading term $f(\phi) = \xi_2 \epsilon_F^2 \phi^2 + \xi_4 \epsilon_F^4 \phi^4$ and a random potential corresponding to quantum corrections.

- *Extra dimension:* potential derived from extra dimension theory which includes exponential Freund and Rubin [1980]

The dimensionless potential and its parameters ditribution are given in Tables 5.1 and 5.2.

5.1.2 Observational cuts

In order to have results in agreement with the observations we have used the following weak priors:

- $\Omega_{DE}(z \simeq 1090) < 0.042$

- $0.6 < h < 0.8$, h being the dimensionless Hubble constant

- $0.6 < \Omega_{DE}^{(0)} < 0.8$

Table 5.1: Definition of the dimensionless potential for various quintessence models. Marsh et al. [2014]

Models	$b_n(\phi)$	c_n	n_{min}	$f(\phi)$	ϕ_i
Kac	ϕ^n	1	1	0	[-1,1]
Weyl	ϕ^n	$1/\sqrt{n!}$	1	0	[-1,1]
Monomial	0	/	/	ϕ^N	[0,4]
EFT	ϕ^n	$(\epsilon_F)^n$	p_E	$\xi_2\epsilon_F^2\phi^2$ + $\xi_4\epsilon_F^4\phi^4$	[-ϵ_F^{-1},ϵ_F^{-1}]
Extra dim.	$e^{\alpha(p_D-n)\phi}$	$(\epsilon_D)^n$	0	0	[-1,1]

Table 5.2: Distribution of the parameters in Table 5.1. U stands for an uniform distribution and the subscript Z indicates that the distribution is over intergers. Marsh et al. [2014]

Parameters	Models	Distribution
$log_{10}(A)$	all	$U(-1,1)$
N	Monomial	$U_Z(1,7)$
n_{max}	Kac, Weyl, Extra dim.	$U_Z(10,20)$
n_Q, p_E	EFT	$U_Z(5,10)$
$log_{10}(\epsilon_{F,D})$	EFT, Extra dim.	$U(-3,-1)$
p_D	Extra dim.	$U_Z(1,5)$
α	Extra dim.	$U(0,1)$

- $-0.85 < w_{DE}^{(0)} \leq -1$

- models who do not reach a scale factor $a = 1$ are not considered

These constraints are weaker than the current observations ones but the aim here is to obtain realistic cosmological models with a reasonnable computational time and not to constrain the models themselves.

The evolution of the cosmological parameters is given by solving the set of differential equations (2.17a),(2.17a), (2.17c) adding a radiation component and considering 3 neutrinos species. The initial condition for the scale factor is $a_i = 10^{-2}a_{eq}$ where a_{eq} is the scale factor at the matter-radiation equality defined by $a_{eq} = 1/z_{eq} - 1$. z_{eq} is drawn from the uniform distribution $U(2000, 4000)$.

The initial conditions for the field are shown in Table 5.1. The velocity of the field is taken to

be $\dot{\phi}_i = 0$. We analysed the influence of adding a cosmological constant, of using a uniform or a logarithmic distribution for the parameters, and of taking $\dot{\phi}_i \neq 0$. Minor differences are seen but the overall behavior is similar and about the same numbers of samples pass the observational cuts (around 5%). However we notice a non negligible sentivity when adding the cosmological constant term.

5.1.3 Results

Evolution of the equation of state of dark energy

We have simulated 2000 samples of each models and the results can be seen in the Figure 5.1. When applying the observational cuts all of these models exhibit almost exclusively a thawing behavior in the sense that the equation of state of dark energy is close to -1 until recently where it begins to go away from -1. This result is logically in agreement with Marsh et al. [2014]. As the evolution of the equation of state is similar for each model and each configuration, after applying the observational cuts, we can only consider one model of these to represent the thawing class, at least for this quantitaive approach. We have chosen the Effective Field Theory as it is a more physically motivated potential than the other ones. The same can be said of the potential resulting of Extra dimensions theory, nevertheless the evolution of the equation of state is very similar for both models so it does not make much differences chosing one or the other.

In order to check whether the behavior is model dependent we have selected potentials considered as of the "freezing class". These potentials are listed in Table 5.3. We have just implemented the potentials with a leading order, i.e. no polynomials so far. This is sufficient to have a first qualitative overview of whether these models enable the equation of state of dark energy to have a freezing behavior. We have decided not to implement an additional cosmological constant term with these models as we only consider a leading order.

Table 5.3: Definition of the dimensionless potential for various "freezing models".

Models	$b_n(\phi)$	c_n	n_{min}	$f(\phi)$	ϕ_i	p_1	p_2
Inverse Power Law	0	/	/	ϕ^{-p_1}	[-1,1]	$U_Z(0.01, 10)$	/
Exponential	0	/	/	$e^{-p_2\phi}$	[-1,1]	/	$U_Z(0.01, 10)$
Hybrid1	0	/	/	$\phi^{-p_1} \times e^{p_2\phi}$	[-1,1]	$U_Z(0.01, 10)$	$U_Z(-5, 5)$
Hybrid2	0	/	/	$\phi^{-p_1} \times e^{p_2\phi^2}$	[-1,1]	$U_Z(0.01, 10)$	$U_Z(-5, 5)$

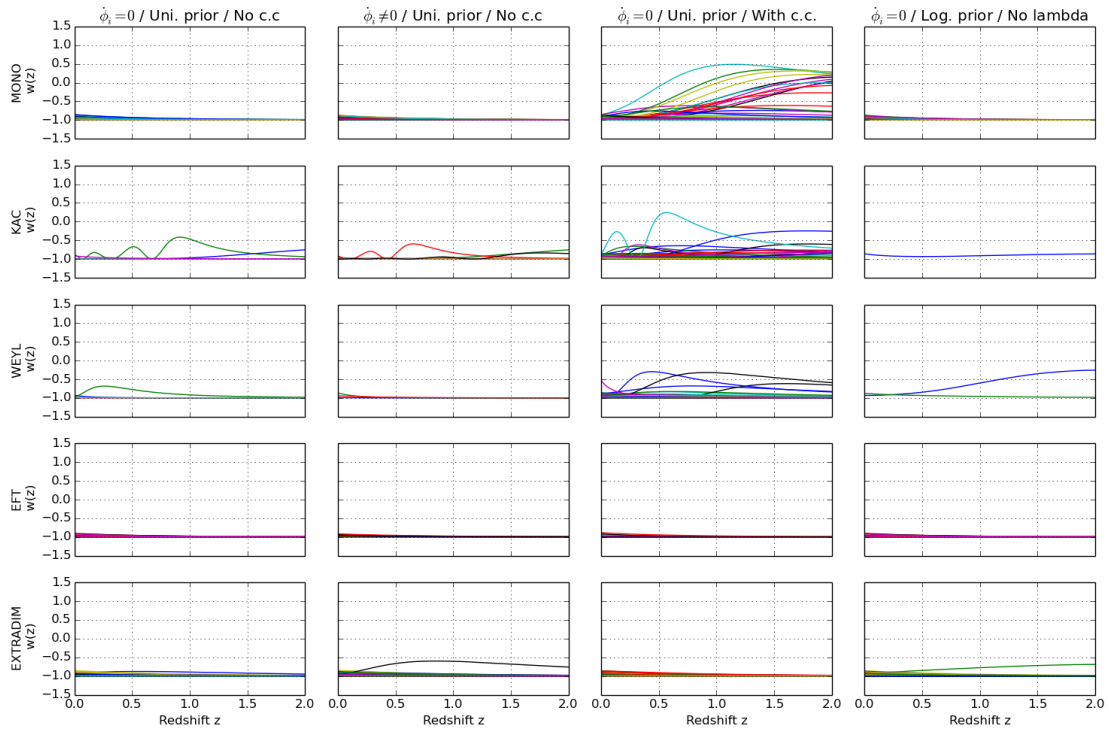

Figure 5.1: Evolution of the equation of state for the 5 models listed in Table 5.1 after applying the observational cuts. With 4 different configurations: *left:* $\dot{\phi}_i = 0$, No cosmologial constant and Uniform distribution, *Middle-left:* $\dot{\phi}_i = 0$, cosmologial constant and Uniform distribution, *Middle-Right:* $\dot{\phi}_i \neq 0$, no cosmologicail constant and Uniform distribution, *Right:* $\dot{\phi}_i = 0$, no cosmological constant and Logarithmic distribution.

We have simulated again 2000 samples for each potential which can be seen in the Figure 5.2. Again very little variations are observed if a logarithmic distribution is used instead of a uniform one, or if the field velocity is chosen to initially equal to zero or not. The "Hybrid1" potential is however very sensitive on the initial value of the field velocity and on the type of distribution.
It is interesting to notice that the Inverse Power Law (IPL) and the exponential with negative coefficient exhibit only thawing behaviors after applying the observational cuts. This can be partly explained by the fact that we impose the field to be frozen at early times to pass the early dark energy observational cut, which imposes a very strong constraint on the evolution of the equation of state which has to be close to -1 at early times, then go away from -1 before approaching -1 again now. Given the more sophisticated form of their potentials the "Hybrid1" and "Hybrid2" potentials allow a freezing behavior more or less in the same proportion as a thawing behavior. As the "Hybrid1" potential shows a high sentivity regarding to the initial conditions and the use of a logarithmic distribution instead of a uniform one, we will prefer to consider the "Hybrid2" potential to perform a quantitative comparison between representatives freezing and thawing models.
In appendix A the Figure A.1 shows the evolution of the 4 selected "freezing" models without

applying the observational cuts and for the configuration: $\dot{\phi}_i = 0$ and Uniform distribution. We qualitatively see that each model exhibits thawing and freezing behaviors, and it illustrates that even if the priors we have used are quite weak they are most of the time favoring a thawing behavior.

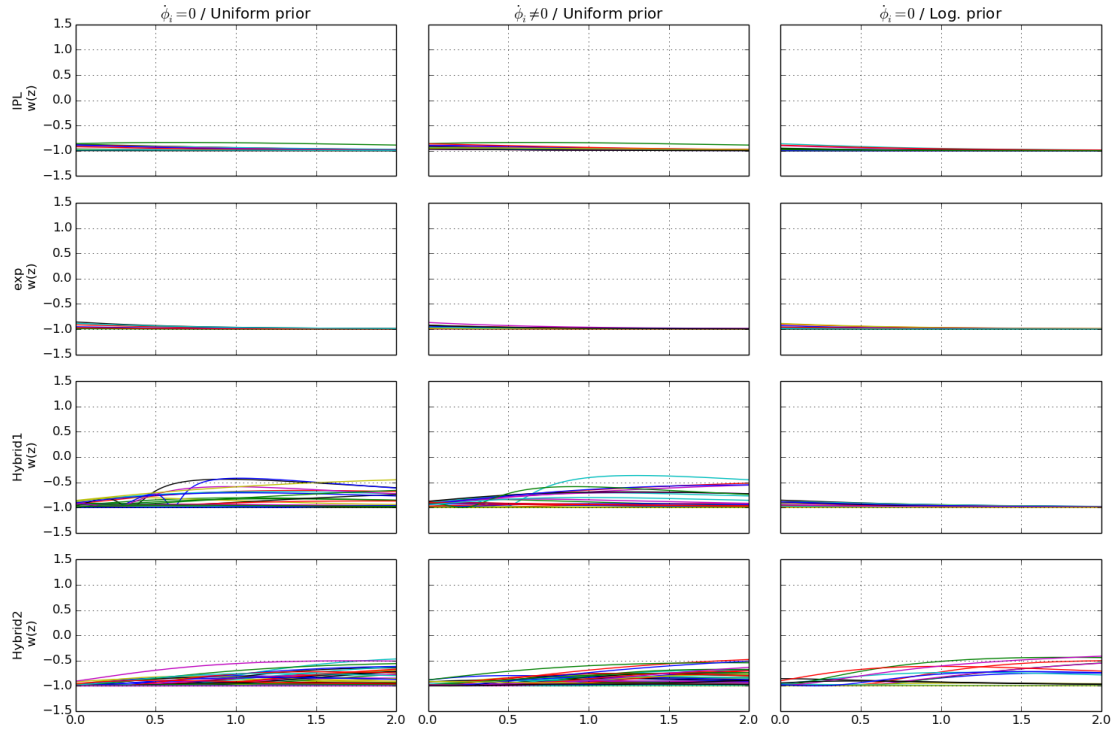

Figure 5.2: Evolution of the equation of state for the 4 "freezing models" and three different configurations: *left:* $\dot{\phi}_i = 0$ and Uniform distribution, *Middle:* $\dot{\phi}_i \neq 0$ and Uniform distribution, *Right:* $\dot{\phi}_i = 0$ and Logarithmic distribution.

Evolution of the fine structure constant with the redshift

As we have selected one representative model for both the freezing and thawing class, namely the "EFT" and "Hybrid2" models, we will study the evolution of alpha for both models.

Given the evolution of $w(z)$ and Ω_ϕ the evolution of alpha is given by the Equation 4.10. It can be seen in Figure 5.3 where we set the coupling factor equals to the standard value of -10^{-5}.

Before looking at the alpha evolution, it is interesting to notice that in the phase space $(w, \frac{dw}{dlna})$ of the Figure 5.3 each sample of the "EFT" model is classified as a thawing model, however for the "Hybrid2" model each sample is first classified as a thawing model, as it has to evolve away from -1, and then at a redshift between 1 and 2 (see Figure 5.4) it enters the freezing region. We also observe that most the samples goes beyond the lower bound of the freezing region defined

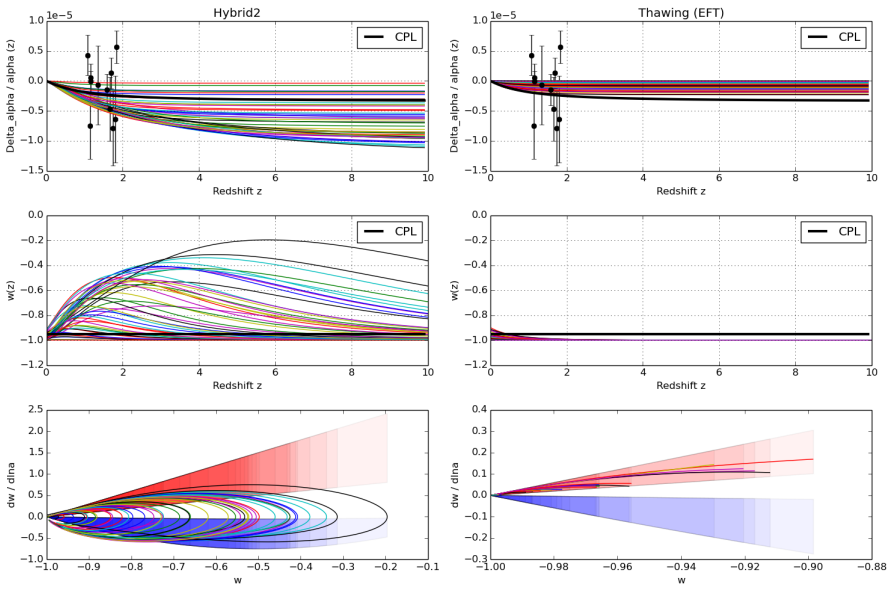

Figure 5.3: *Top:* Evolution of $\Delta\alpha/\alpha(z)$ for the "Hybrid2" and "EFT" models. The black points and their error bars reperesents the measurements of the "small" dataset. *Middle:* Corresponding evlution of the equation of state of dark energy for both models for the 2000 samples after applying the observational cuts. *Bottom:* The $(w, \frac{dw}{dlna})$ phase space for both models where the blue and red regions corresponds respectively to the freezing and thawing regions defined by Caldwell and Linder [2005]. The thick black line correpsonds to the CPL parametrisation with $w_0 = -0.95$ and $w_a = 0$.

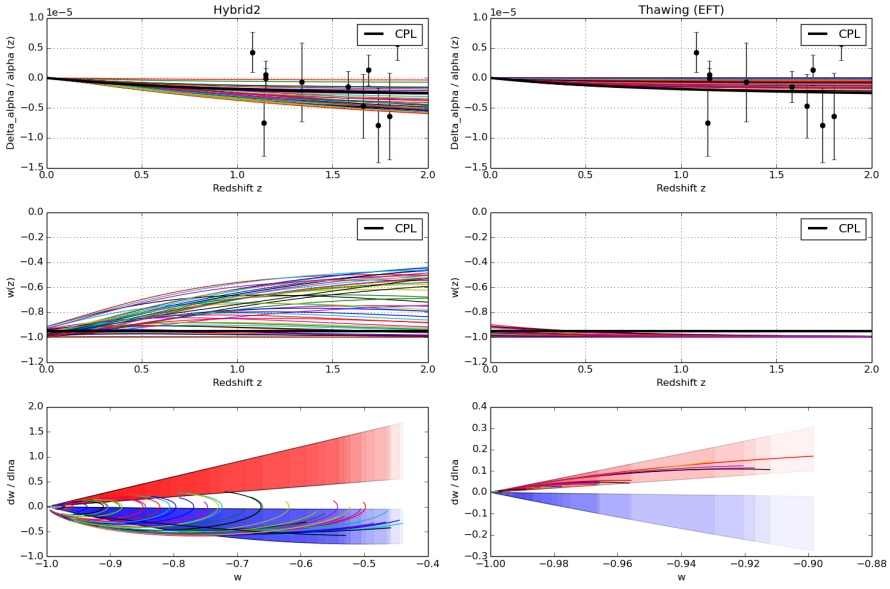

Figure 5.4: Same as Figure 5.3 but restricted to the redshift range $0 < z < 2$.

by Caldwell and Linder [2005]. This has also been reported in the work of Huterer and Peiris [2007].

Regarding to the alpha evolution, we see that the freezing model and the thawing one have different evolutions of alpha. This was expected as we see in the Equation 4.10 that the variation of

alpha depends of the integral from 0 to z of a quantity containing the term $(1 + w)$, so the evolution is very sensitive to the value of the equation of state of dark energy. The more different from -1 the equation of state is, the higher is the variation of alpha. We thus expect a faster variation of alpha for freezing models.
An other interesting feature of the Equation 4.10 is that even a constant equation of state different from -1 leads to a variation of alpha as the CPL parametrisation shows in Figures 5.3 and 5.4.

In the Figure 5.3, as we were expecting from the Equation 4.10, we observe that for both models as long as the equation of state is different from -1 and still evolving there is an increasing variation of alpha with the redshift until it reaches -1.
For the freezing model we see that the alpha variation is about -0.5×10^{-5} at a redshif $z = 2$ and -0.8×10^{-5} at a redshift $z = 4$, which is the most distant redhsift at which we can currently measure alpha spectroscopically with good accuracy.
So for the freezing class it appears that the variation of alpha is continuously evolving from $z = 0$ to $z = 4$ to reach the same order of magnitude as the coupling factor at a redshift $z \simeq 4$. Whereas for the thawing model the alpha variation remains constant for almost all the samples from the redshift $z \simeq 1.5 - 2$ to higher redhsifts and with almost one order of magnitude less than the coupling factor.

We see that with the current sensitivity of the HIRES-KecK and UVES-VLT, around $\sigma \simeq 2 - 8 \times 10^{-6}$, it is only possible to distinguish extreme samples of both classes.
If we consider the Echelle SPectrograph for Rocky Exoplanet- and Stable Spectroscopic Observations ESPRESSO, a new-generation spectrograph for ESO's VLT, with an expected sensitivity of $\sigma_{esp} \simeq 4 - 8 \times 10^{-7}$ in measuring $\frac{\Delta\alpha}{\alpha}$ (Pepe et al. [2013], Amendola et al. [2012]). It will increase the sensitivity of one order magnitude with respect to the current observational facilities such as UVES-VLT and HIRES-Keck. To illustrate this gain we have plotted in the Figure 5.5 the alpha measurements of the "small" dataset with uncertainties having one order of magnitude less. As the mean value of the alpha measurements will change with the new spectrograph, we just have to pay attention at the error bars and we see that for a coupling factor of $\zeta = -10^{-5}$ alpha measurements will allow a distinction between most freezing and thawing samples. It might also make a distinction among freezing samples but not among thawing samples.
The Figure 5.1 shows that in all the thawing models the eos evolves away from -1 at a redshift around 2, so the only conclusion we might drawn from this quantitative analysis for the thawing class is that a variation of alpha remaining constant from a redshift around 1.5-2 to higher

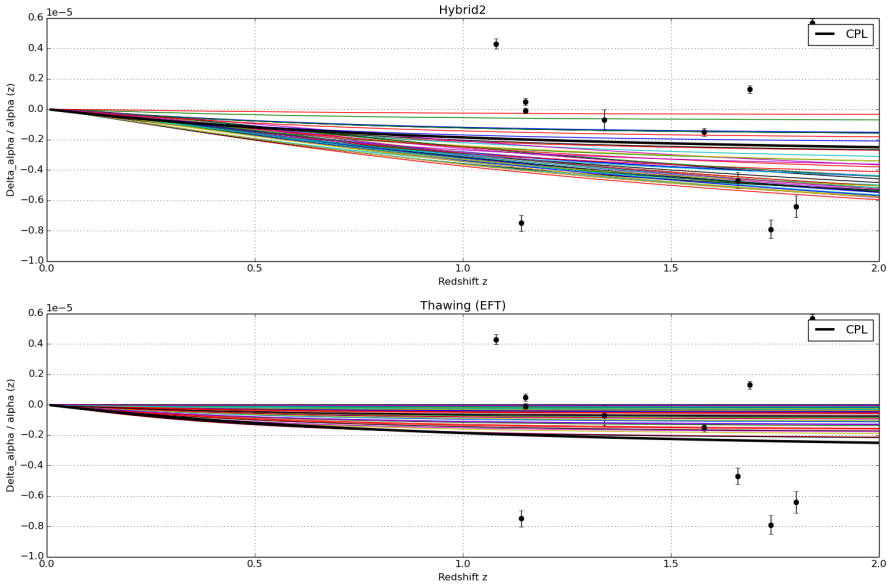

Figure 5.5: Same as in Figure 5.4 but with uncertainties lowered of one order magnitude as expected with ESPRESSO.

redhsifts would favor the thawing class and on the contrary an evolving alpha variation will favor the freezing class.

As simple as this quantitative method might be, it gives us a first impression on a possible detection of a thawing or freezing behavior of the equation of state thanks to alpha measurements with future facilities such as ESPRESSO.

Comparison with the redshift drift

As the redshift drift allows to probe the same redshift range as alpha measuremtns it is interesting to compare both methods to see which one is the most suitable one to distinguish between a freezing and a thawing behavior. The spectroscopi velocity shift is shown in Figure 5.6 where we have chosen a period of Δt =30 years, a Signal-to-Noise ratio of 3000 and 30 QSOs uniformly distributed over the redshift range $2 < z < 5$ among the following redshift bins z_{QSO} = [2.0,2.8,3.5,4.2,5.0] as in Martinelli et al. [2012].

We observe that there is no significant difference in the evolution of the signal δv for both models and thus can not be used for distinguishing the thawing / freezing classes.

Even if we have to keep in mind that the alpha measurements are model dependent this seems to be one of the most promising cosmological probe at high redshift to distinguish among the freezing and thawing classes.

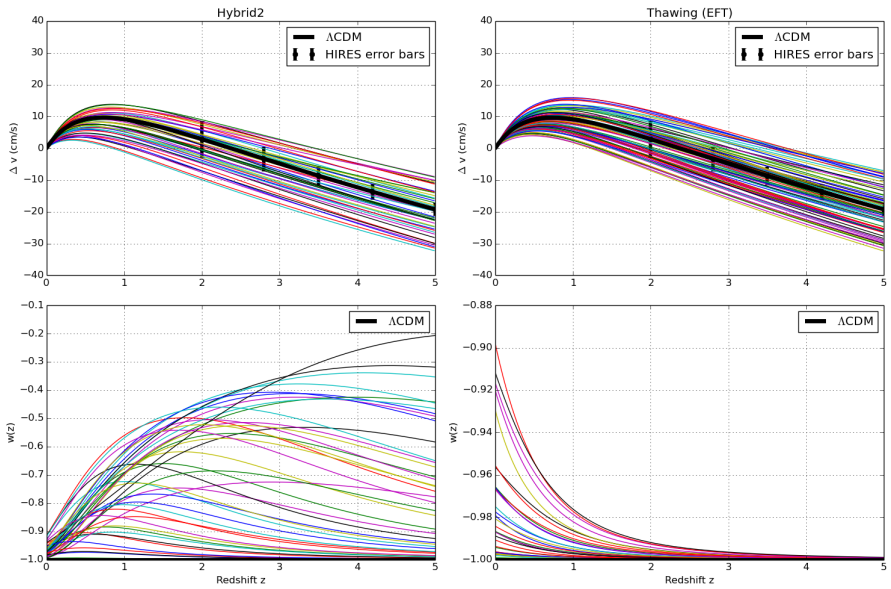

Figure 5.6: Spectroscopic velocity shift for the different samples of the ”Hybrid2” model (*Left*) and of the ”EFT” model (*Right*).

In the following sections we will use some specific parametrisations of the equation of state of dark energy to study more qualitatively the constraints that the alpha measurements might bring first to the coupling factor and then to some cosmological parameters such as the equation of state, the matter and dark energy density parameters. We will also use two simple quintessence potentials and study whether the alpha measurements bring tighter constraints on the parameters composing it in comparison to the standard Type Ia Sne and Hubble parameter data set.
As we will use up to 5 free parameters, we will not perform a frequentist likelihood analysis on the whole grid of parameters but rather use a Monte Carlo Markov Chain (MCMC) algorithm to sample the posterior.
We will then first introduce some basics about Bayesian inference and MCMC algorithm before performing the different analysis.

5.2 Bayesian inference

In Cosmology, Bayesian inference is used to estimate the theoretical model's parameters from observational data in terms of probabilities.
If we consider a theoretical model with M parameters describing a set of N observational data, we create a M-dimensional vector $\boldsymbol{\theta}$ = (θ_1,θ_2,...,θ_M) containing all the parameters and a N-dimensional vetor **x**=(x_1,x_2,...,x_N) containing all the data points. For instance, in the case of Type Ia Sne measurements the parameters θ_i can be the matter density parameter Ω_m or the equation of state of dark energy w and the observable are the luminosity distances.
The aim of Bayesian inference is then to estimate the probabilty of the parameters θ_i given the measurements data, which is written $p(\boldsymbol{\theta}/\mathbf{x})$ and is called the *posterior distribution*. The notation p(A/B) means the probability of having A given B.
However the posterior does not have a trivial expression most the time. One solution is to use the Bayes' Theorem:

$$p(\boldsymbol{\theta}/\boldsymbol{x}) = \frac{p(\boldsymbol{x}/\boldsymbol{\theta})p(\boldsymbol{\theta})}{p(\boldsymbol{x})} \tag{5.3}$$

where $p(\mathbf{x}/\boldsymbol{\theta})$ is the *likelihood* and expresses how probable are the observations given a certain theoretical cosmology model. In the following we will use the notation $\mathcal{L}(\boldsymbol{\theta}) \equiv p(\mathbf{x}/\boldsymbol{\theta})$ to refer to the *likelihood*.
$p(\boldsymbol{\theta})$ is the *prior distribution* and expresses the a priori knowledge on a given parameter. This can come from previous calculations or studies, or from physical limits on the parameter.
$p(\mathbf{x})$ is a normalisation constant, called the *Bayesian evidence*, it can expressed as:

$$p(\boldsymbol{x}) = \int p(\boldsymbol{x}/\boldsymbol{\theta})\; p(\boldsymbol{\theta})\, \mathrm{d}\theta \tag{5.4}$$

and is only of interest when comparing models as it has the same value for each parameters.
In our case we just perform parameter inference and do not compare models so the posterior distribution is expressed as the product of the *likelihood* with the *prior distribution*:

$$p(\boldsymbol{\theta}/\boldsymbol{x}) \;\propto\; \mathcal{L}(\boldsymbol{\theta})\; p(\boldsymbol{\theta}) \tag{5.5}$$

In the particular case where one parameter can take any value equally likely, the prior is therefore constant and is called a "flat prior". The posterior distribution is thus only proportional to the likelihood.

In Cosmology the observations data are often considered to follow a Gaussian distribution. In this case, if we consider a data set **x**=(x_1,x_2,...,x_N), the probability of each point in this set given the parameters (i.e. the likelihood) is fully caracterised by two parameters, the mean μ and the variance σ^2 of the Gaussian distribution:

$$\mathcal{L}(\boldsymbol{\theta}) \equiv p(\boldsymbol{x_i}/\boldsymbol{\theta}) = \;\frac{1}{\sqrt{2\pi\sigma_i}} exp\left[-\frac{\left(x_i - \mu(\theta)^2\right)}{2\sigma_i^2}\right] \tag{5.6}$$

Here σ_i is the observational error in measuring x_i and $\mu(\theta)$ the value given by the theory. In the case of Type Ia SNe x_i will be the measured luminosity distance (or distance modulus) of one supernova, σ_i its error, and $\mu(\theta)$ the theoretical one.

5.3 Monte Carlo Markov Chains

As we have briefly described in the previous section, the aim of Bayesian inference is to find a method to evaluate the posterior distribution. Whenever no analytical solutions exist or are not accurate enough, numerical techniques are used. The Monte Carlo Markov Chains tehnique is the most common one. A Monte Carlo algorithm rely on repeated random sampling to evaluate a quantity. The Markov Chains generate the samples. The aim of a MCMC algorithm is to generate a sequence of points in the parameter space, this is called a "chain", whose density is proportional to the posterior. As we do not intend to make a detailed descritpion of Markov Chains, we refer to Robert and Casella [2004], Gamerman and Lopes [2006] for a complete description.
A Markov Chain is then defined by a sequence of random variables $\{X^{\{0\}}, X^{\{1\}}, ..., X^{\{N-1\}}\}$, where the state $X^{\{i+1\}}$ depends only on the state $X^{\{i\}}$. In our case the random variables are the

parameters $\boldsymbol{\theta}$, the parameter space is explored by moving from one state $\boldsymbol{\theta^i}$, which is a vector containing the values of all parameters for this state, to another $\boldsymbol{\theta^{i+1}}$. For each state the likelihood is calculated and the decision to move to a new state is determined probabilistically using the posteriors. To generate the elements of the chain there are several algorithms such as the Metropolis-Hastings algorithm (Metropolis et al. [1953], Hastings [1970]), the Gibbs sampling (Smith and Roberts [1993]), or Hamiltonian Monte Carlo (Hanson). The choice is made depending on the characterisitcs of the considered probem. We are using the affine invariant ensemble sampler proposed by Goodman and Weare [2010] and the publicly available code implemented in python "emcee" Foreman-Mackey et al. [2013] because it allows parallel calculations and is thus faster.

One important feature of Markov Chains is that after some iterations the chain converges to a stationary state, the target distribution, which is the posterior distribution of parameters $p(\boldsymbol{\theta}/\boldsymbol{x})$ in our case. When the chain has converged, the successive elements of the chain are thus sampled from the posterior.

The standard way of a MCMC algorithm is the following:

1) Define a starting state

2) Propose a random jump from the state $\boldsymbol{\theta^{\{i\}}}$ to the state $\boldsymbol{\theta^{\{i+1\}}}$

3) Calculate the likelihood at the state $\boldsymbol{\theta^{\{i+1\}}}$ and multiply it by the prior at this state to obtain the posterior of this state $P(\boldsymbol{\theta^{\{i+1\}}})$

4) The new state $\boldsymbol{\theta^{\{i+1\}}}$ is accepted if $\frac{P(\boldsymbol{\theta^{\{i+1\}}})}{P(\boldsymbol{\theta^{\{i\}}})} > 1$ which means that the successive states are evolving to the highest likelihood. If it is not the case the new state can still be accepted with the probability $\frac{P(\boldsymbol{\theta^{\{i+1\}}})}{P(\boldsymbol{\theta^{\{i\}}})}$ to enable a sampling of the region close the high likelihood region.

5) Repeat until the posterior is sampled with enough points

Even if the steps 2) to 4) are algorithm dependent and thus subject to differences, the main idea follows this scheme though.

If the chain is started at a random position, it will take some steps before the chain converges to the posterior distribution. These steps corresponds to the "burn-in" phase and the posterior is sampled with the Monte Carlo algorithm after the burn-in phase.

In order to chek whether the chain has converged several criteria exist. An exhaustive review was made by Cowles and Carlin [1996]. In our case we follow the recommandation given by Foreman-Mackey et al. [2013] and pay attention to the autocorrelation time which is a direct measure of the number of evaluations of the posterior distribution required to produce indepen-

dent samples of the target density. The acceptance fraction, which quantifies how many state proposals were accepted, is also checked to be in the acceptable range $0.2 <$ acceptance fraction < 0.6 (Foreman-Mackey et al. [2013]). An acceptance fraction close to zero means that almost all the proposals were rejected and the chain will contain very few independent samples. On the contrary if the acceptance fraction is close to 1, almost all proposals were acepted and the chain contains samples which are not representative of the target density.

We have also paid attention that the chain mixes well in the parameter space, i.e. that it does not get blocked somewhere for a lot of iterations and that it explores a representative part of the parameter space and not only a tiny area.

5.4 Results

In this section we will present the probability distribution of different cosmological parameters with the MCMC algorithm. We consider a flat Universe dominated by matter and dark energy. The SN dataset is used to compare the theoretical luminosity distance with the one obtained by the data of the Union2.1 dataset. The Hubble parameter dataset is used to compare the values of the Hubble parameter at different redshift listed in 3.1 with the theoretical one. And the alpha dataset is composed of either the Keck, or VLT, or "small" dataset or a combination of the three. Flat priors are used for all simulations.
The aim is to study whether the alpha measurements might bring tighter constrain on some cosmological parameters.

5.4.1 Constant equation of state

We will first test the algorithm in the case of a constant equation of state with only 2 parameters: the constant equation of state w_0 and the coupling factor ζ. We can then compare the results with the one obtained by Martins and Pinho [2015] where they have used a frequentist approach by exploring the whole grid of parameters. We are using te Union2.1 Supernovae data, the Hubble parameter data and the alpha mesurements from all the dataset combined. Our result is seen on the Figure 5.7. The median value of the marginalised posterior for w_0 is -0.998 and the first and third quartiles give an estimated uncertainty of $+0.0229\ /\ -0.0158$. Similarly, for ζ we obtain -6.98×10^{-8} with an estimated uncertainty of $+5.49 \times 10^{-6}\ /\ -5.23 \times 10^{-6}$. This result allows an equation of state equal to -1 and a null variation of alpha. This result is in agreement with Martins and Pinho [2015]

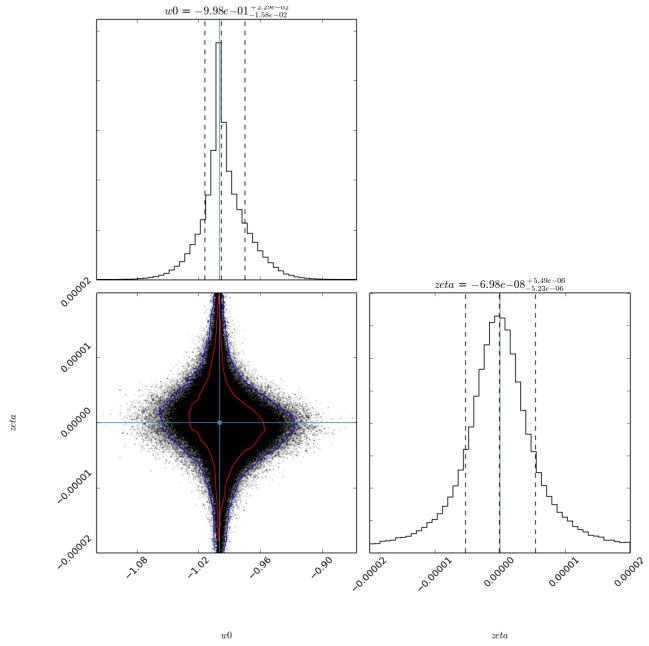

Figure 5.7: The 2D $w_0 - \zeta$ histogram considering a constant equation of state. Only 2 parameters are allowed to vary:w_0 and ζ. We have set $\Omega_{m0} = 0.3$ and $h = 0.7$. The 1D histograms on the diagonal represents the marginalised posterior distribution for each parameters. The dataset used combined SN+Hubble+alpha measurements. The red contour contains 68% of the points and the blue one 95%. The black points represents the sampling of the posterior distribution

An other test we have performed is to use either alpha measurements data set separately or combined. On the Fig. 5.8 we see on both plots that we obtain a bi-modal posterior corresponding to quintessence and phantom field, we recall equations 4.10 and 4.11. The figure on the top (data from the Keck Telescope) shows that for $w_0 < -1$ correponds a positive ζ and inversely for $w_0 > -1$ correponds a negative ζ, these dataset favors then a negative $\frac{\Delta\alpha}{\alpha}$ and excludes a null variation at least 2σ. On figure on the bottom (data from VLT) the data favors on the contrary a positive value for $\frac{\Delta\alpha}{\alpha}$, the null variation is also excluded at at least 2σ but not as strong as the alpha measurements from the Keck Telescope. In order to estimate more precisely the exact number of σ the null variation is excluded for both cases a better sampling of the posterior is needed. This is in agreement with the results of Murphy et al. [2004].

On the Fig. 5.9 the figure on the top represents the result combining the Keck and VLT data sets and we see that the null variation is not excluded anymore. An equation of state lower than -1 is slightly favored as well as a negative value of $\frac{\Delta\alpha}{\alpha}$ and the coupling factor is constrained at 1σ to be lower than 5×10^{-6}. The figure on the bottom represents the results with the small data set only and pretty much the same conclusion can be drawn. This is also in agreement with Webb et al. [2011a], King et al. [2012].

In the following we will always use all the data set together as it might lower the influence of systematics on the results.

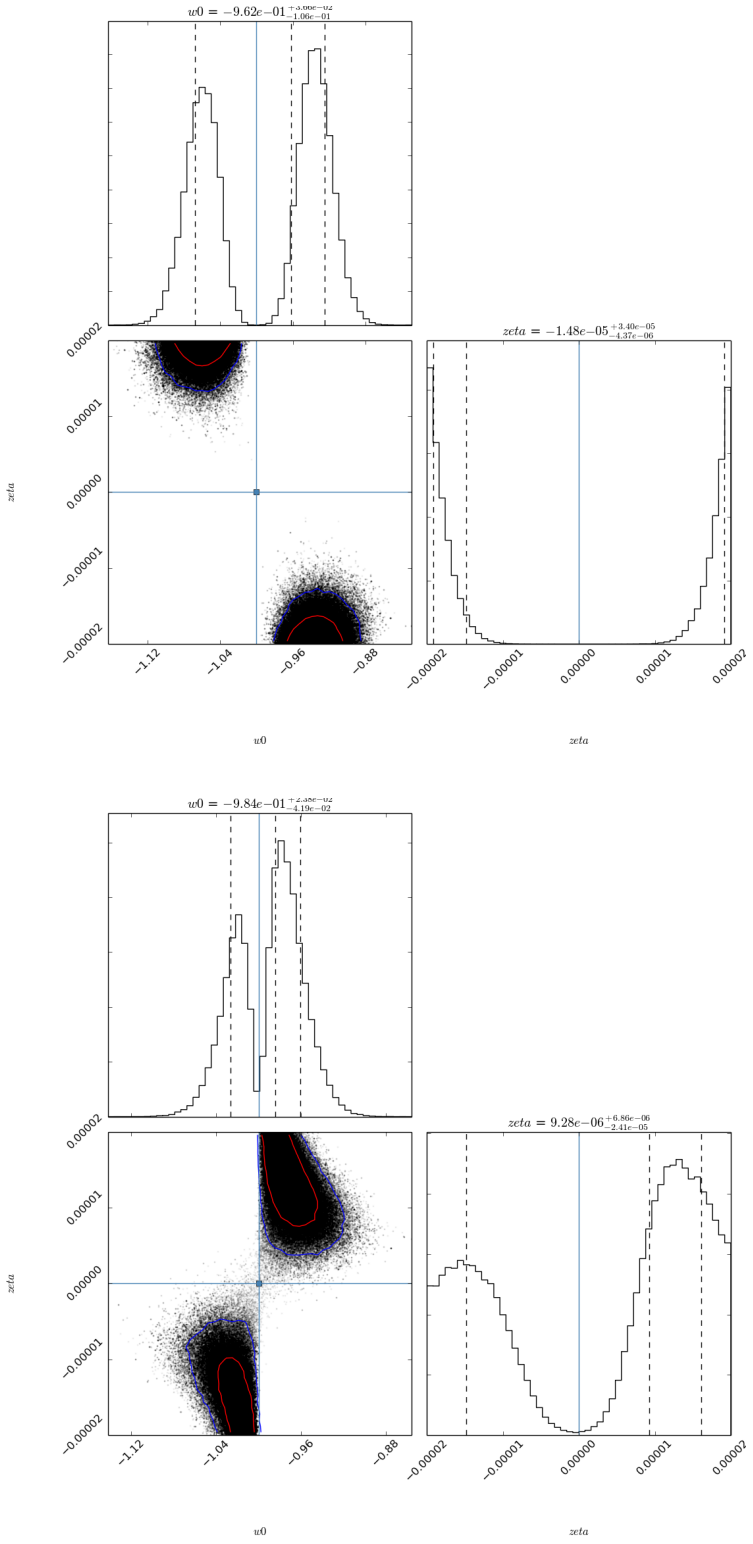

Figure 5.8: The 2D $w_0 - \zeta$ histogram considering a constant equation of state. Only 2 parameters are allowed to vary:,w_0 and ζ. We have set $\Omega_{m0} = 0.3$ and $h = 0.7$. The 1D histograms on the diagonal represents the marginalised posterior distribution for each parameters. The dataset used combined SN+Hubble+alpha measurements. *Top:* Alpha measurements from the Keck Telescope, *Bottom:* alpha measurements from the VLT. The red contour contains 68% of the points and the blue one 95%.

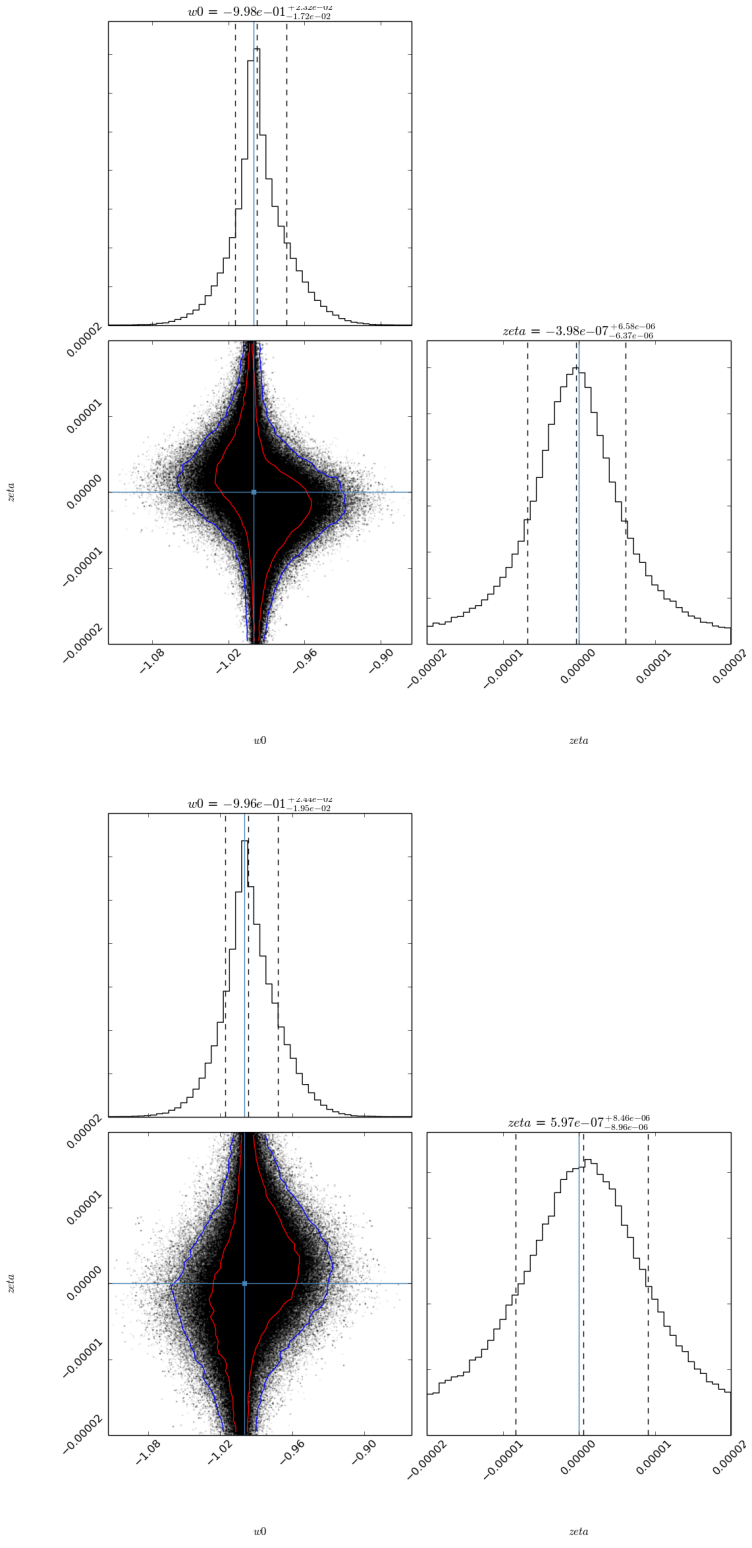

Figure 5.9: Same as Fig. 5.8 with alpha measurements from the Keck Telescope and the VLT combined (*Top*) and alpha measurements from the more recent set (*Bottom*). The red contour contains 68% of the points and the blue one 95%.

5.4.2 The CPL parametrisation

In this section we have parametrised the equation of state using the CPL parametrisation. We have allowed 4 parameters to vary during the simulation: Ω_{m0},w_0,w_a and ζ. The result is seen in the Fig. 5.10, where the blue lines refer to the Union2.1 SNe dataset alone, the red lines refer to SNe + Hubble parameters and the green ones to SNe + Hubble + alpha. We see that the marginalised posterior distribution is more peaked for the parameters Ω_{m0},w_0 and w_a when adding the Hubble parameters dataset to the SN dataset. When adding the alpha measurements we see that it brings a tighter constraint on w_a, as expected because this parameter represents the variation of the eos with respect to the redshift and the alpha data set is the only dataset to probe up to $z \sim 4$. It favors also a negative value for w_a similarly to the one in Planck Collaboration et al. [2015a]. The coupling factor ζ distribution excludes the non-variation of alpha, which was not expected using all alpha datasets together as it is not hte case if a constant eos is assumed. So it is clearly parametrisation dependant. The matter density parameter is also a bit more constrained when adding the alpha measurements, the lower values are discarded. The Table 5.4 lists the median value of the marginalised posterior distribution for each parameter and each dataset.

However due to the bimodal distribution when adding the alpha measurements one has to be carreful before drawing conclusions and comparing it with other data sets such as the CMB for instance. When applying the correction we used for each result we ended with an unimodal distribution (see Appendix B) but without applying any correction results in a bimodal distribution. Consequently, this result has to be checked with an other MCMC code (with a better handling of the multi-modal distribution) for consistency before claiming that a no-variation is excluded using the CPL parametrisation.

Table 5.4: Median, first and third quartiles of the marginalised posterior distribution for the different cosmological parameters.

Parameters	SN	SN + Hubble	SN + Hubble + alpha
Ω_{m0}	$0.345^{+0.072}_{-0.147}$	$0.243^{+0.047}_{-0.096}$	$0.273^{+0.014}_{-0.014}$
w_0	$-1.12^{+0.221}_{-0.255}$	$-0.936^{+0.103}_{-0.1}$	$-0.877^{+0.055}_{-0.050}$
w_a	$0.078^{+1.17}_{-1.85}$	$0.448^{+0.484}_{-0.910}$	$-0.387^{+0.159}_{-0.174}$
ζ	/	/	$-4.37e^{-5}\ ^{+1.41e^{-5}}_{-1.93e^{-5}}$

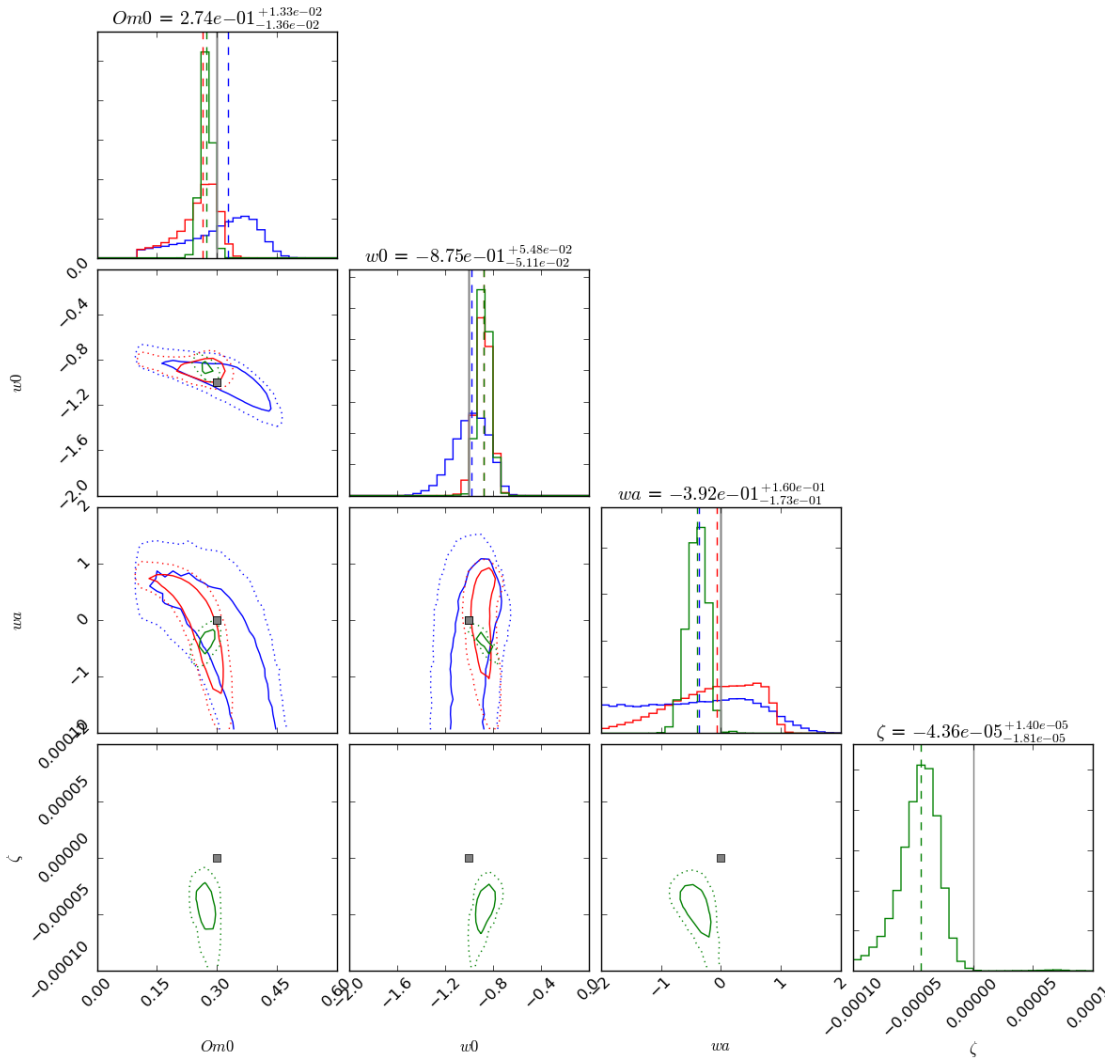

Figure 5.10: The 2D histograms of the CPL parametrisations where we allow 4 parameters:Ω_{m0},w_0,w_a and ζ. h is taken equal to 0.7. The 1D histograms on the diagonal represents the marginalised posterior distribution for each parameters. The blue contour represents the SN dataset, red: SN+Hubble, green: SN+Hubble+alpha. The straight contour contains 68% of the points and the dotted one 95%. The dashed lines represent the median values.

5.4.3 Quintessence

In this section, the aim is to study whether the alpha measurements might help to constrain some quintessence models. For this purpose we have coupled the autonomous system 2.18a,2.18b and 2.18c with the MCMC algorithm developped by Foreman-Mackey et al. [2013]. The autonomous system is solved using the publicly available python code "ScalPy: A Python Package For Late Time Scalar Field" Kumar et al. [2015]. Two quintessence models, the inverse power law and the exponential ones, whose potentials are given in Equations 2.19 are studied.

The autonomous system is integrated from the photon decoupling epoch to now, so from a redshift z=1101 to 0. We stress the fact that radiation is neglected in the ScalPy solver although it starts at z=1101, ideally the autonomous system based on 2.17a and 2.17b should be modified to take the radiation into account. Nevertheless we consider it as an acceptable approximation in a first approach. 3 initial conditions are needed, (γ_{ini}, $\Omega_{\phi\ ini}$,λ_{ini}) where $\gamma_{ini} = 1 + w(z = 1101)$, $\Omega_{\phi\ ini}$ is the scalar field density parameter at $z = 1101$ and the value of the slope of the potential λ_{ini}. We will first perform the MCMC run with all these 3 parameters free to vary in addition to the coefficients of the inverse power law and exponential potentials to get a first idea of the most likely value if any. And then we will focus on constraining the quintessence potential coefficients only and see if the alpha measurements brings tighter constraints.

The following priors were used for these parameters:

- $0 < \gamma_{ini} < 2$, as for a quintessence model $-1 < w < 1$

- $10^{-11} < \Omega_{\phi\ ini} < 10^{-3}$, the upper bound comes from the Planck Mission 2015 results Planck Collaboration et al. [2015b], and the lower bound is set so that it allows some deviation from the ΛCDM model which predicts $\Omega_\phi(z = 1101) \simeq 1.74 \times 10^{-9}$

- $\lambda_{ini}^2 < 6$, using the fixed points study carried out in Copeland et al. [2006].

- $-20 < n < 0$, we allow the power law coefficient to vary in this range even if some studies have already showed that current observational constraints put a lower bound on p: -2 $\lesssim p$ Eriksson and Amanullah [2002], Chen et al. [2015]

Inverse Power Law potential

For the IPL (Inverse Power Law) the results can be seen in Figure 5.11. We can see that the initial value of the scalar field density parameter has a well peacked distribution centered at about the same value as the one given by the ΛCDM model. The initial value of the γ parameter is quite unconstrained, and hence allows freezing models. The coefficient n is also not well constrained. Finally the initial value of the parameter λ is well constrained around 1.

Even if the IPL potential respects the tracker condition $\Gamma > 1$, Rakhi and Indulekha [2009], which means that it shoud not be sensitive to the initial conditions, we see that the initial slope of the potential and the initial amount of Dark Energy have to respect some constrains. It can be explained by the fact that even if Dark Energy can be represented mathematically by a stable fixed point in this system, we do not know where our epoch is ”located” in the phase plane. As analytically calculated in Copeland et al. [2006], for the IPL the only fixed point which might allow a late time expansion ends with a dark energy density parameter equal to 1, and today the value is around

0.7. So if this is the fixed point where we are attracted to, we have not reached it yet and thus different initial conditions still lead to different values.

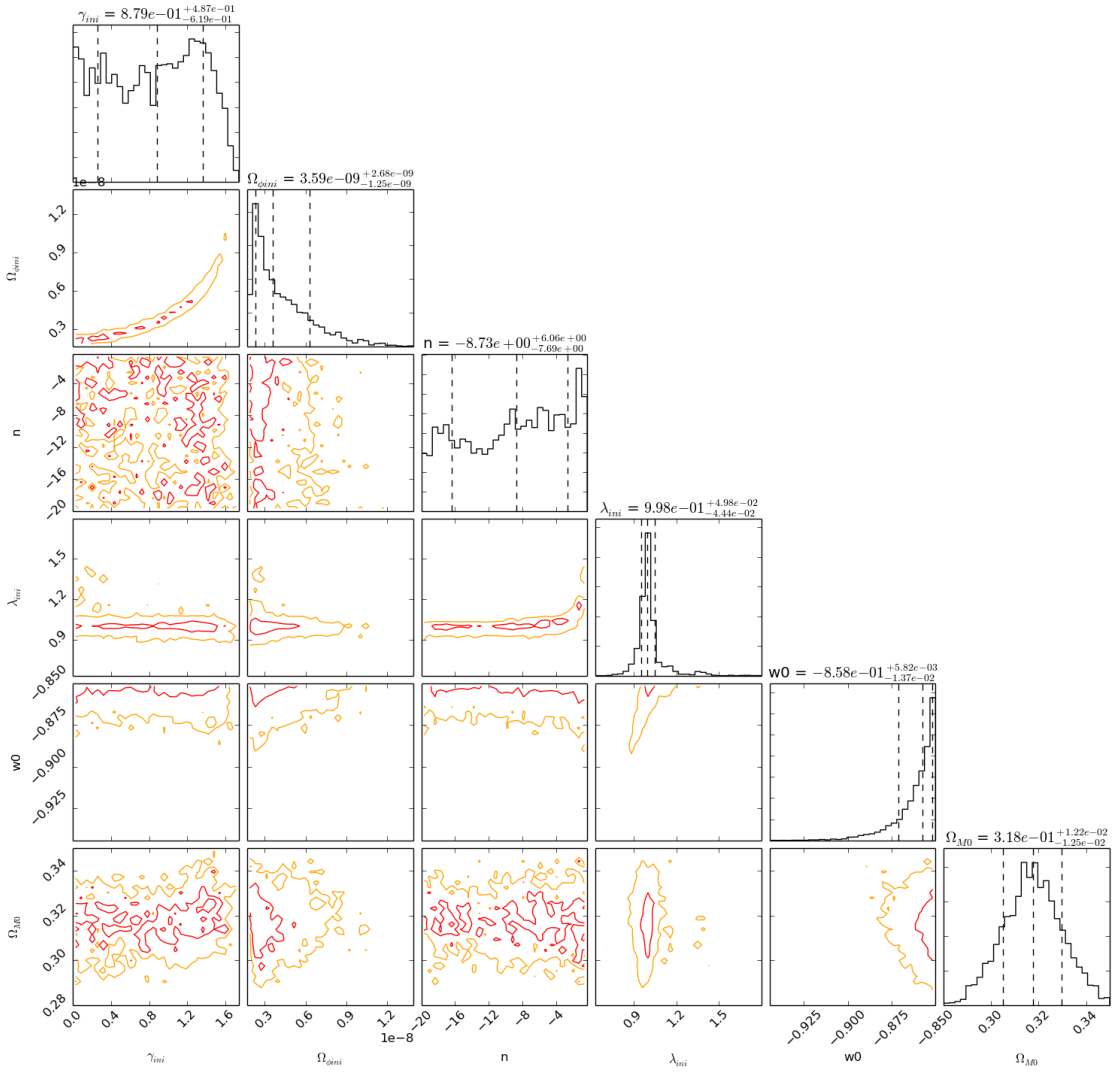

Figure 5.11: The 2D histograms of the IPL parametrisations where we allow 5 parameters to vary: γ_{ini}, $\Omega_{\phi\ ini}$, λ_{ini}, n and ζ . The 1D histograms on the diagonal represents the frequency distribution for each parameters. Red: The SN+Hubble dataset, Green: SN+Hubble+Alpha. The straight contour contains 68% of the points and the dotted one 95%. The dashed lines represent the median values.

The resulting distribution of others cosmological parameters is also seen on the Figure 5.11. We see that the matter density agrees very well with the current observations while the eos today is a bit lower than the current observations but still acceptable not to rule it out completly. This shows that with the right choice of initial values, especially for $\Omega_{\phi\ ini}$ and λ_{ini} the current observational constraint on w_0 and $\Omega_{M\ 0}$ can be respected. The power law coefficient does not seem to be important as it is here not constrained. This is a bit surprising and might need to be

investigated in a future study.
We see that alpha measurements do not clearly bring tighter constrains on these parameters.

Exponential potential

Considering the exponential potential, the Figure 5.12 shows that the eos and matter density today are in agreement with the ones of the current LambdaCDM model. The exponential coefficient λ has a quite peak marginalised distribution, but as we did not perform a detailed study we can not give importance to the median and deviations yet. The aim of this study was to see the effect of the alpha measurements of these parameters and we see that it does not bring tighter constraint.

In order to test the robustness of these results, especially whether they are still biaised because of the initial conditions, it will be needed to run the MCMC with more walkers and steps to check whether the results change. For this study 200 walkers and 1000 steps were chosen. This yields for both IPL and exponential potentials, once this test is performed the marginalised ditributions could be analysed in detailed to extract the median and deviation values.

An other interesting study might be to keep constant the initial conditions for the parameters $\Omega_{\phi\ ini}$ and λ_{ini} at the values we have found to be more likely here, fix γ_{ini} to 0.01 for simulating a thawing behavior and then to 1 for a freezing behavior, and let the coefficients p for the IPL and λ for the exponential potential vary in order to compare the constraints obtained with and without the alpha measurements.

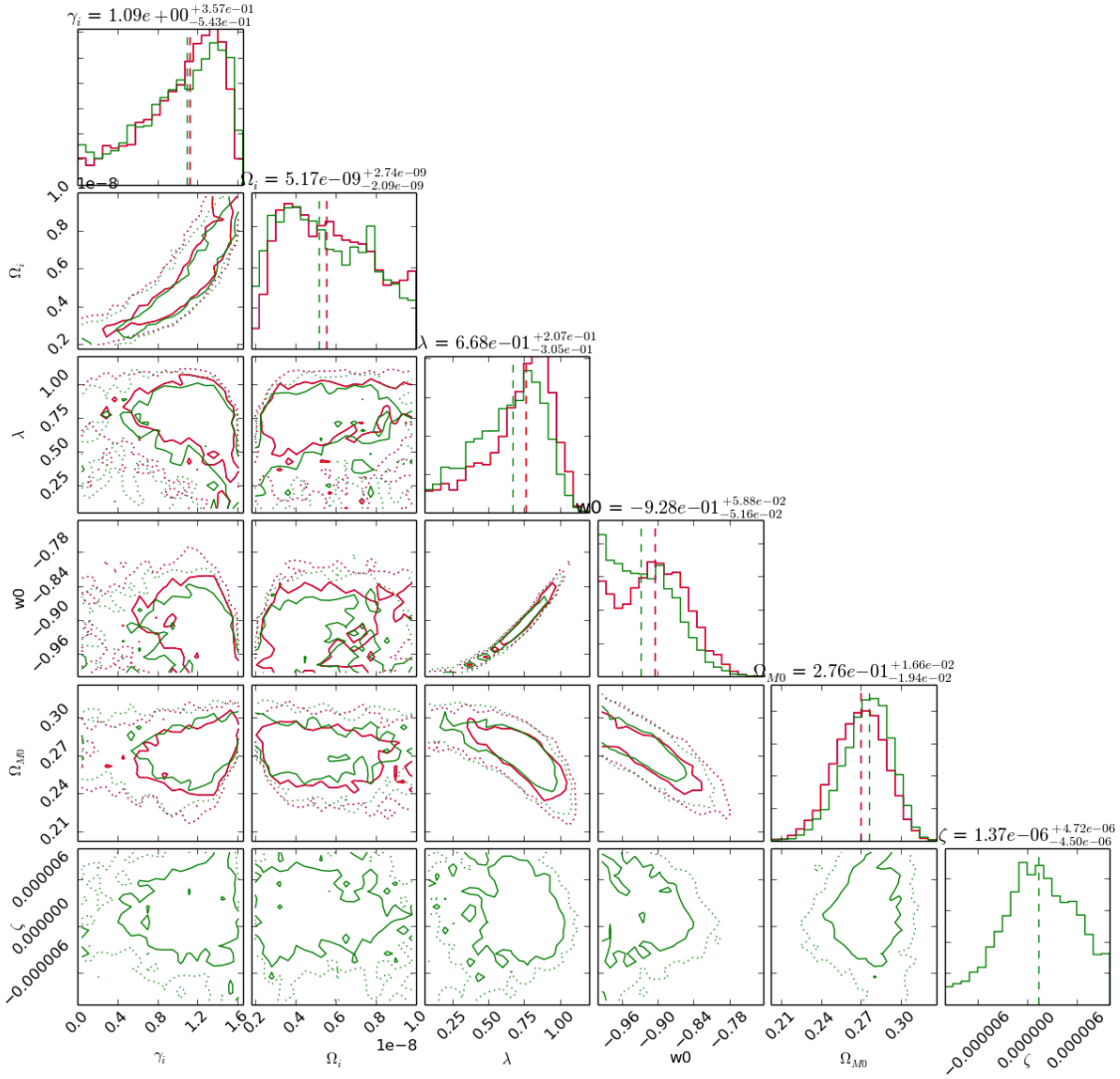

Figure 5.12: The 2D histograms of the exponential parametrisations where we allow 4 parameters to vary: γ_{ini}, $\Omega_{\phi\ ini}$, λ and ζ as well as the resulting distribution of the eos today w_0 and the matter density today $\Omega_{M\ 0}$. The 1D histograms on the diagonal represents the frequency distribution for each parameters. Red: The SN+Hubble dataset, Green: SN+Hubble+Alpha. The straight contour contains 68% of the points and the dotted one 95%. The dashed lines represent the median values.

Chapter 6.

Non parametric Analysis

6.1 Principal Component Analysis

6.1.1 Definition

For this method we will follow the work done by Huterer and Starkman [2003] to constrain the eos of dark enegy using SNeIa data and Amendola et al. [2012] who extended the method to alpha measurements.

First the data set is divided in N redshfit bins, and in each bin i the equation of state is w_i. The eos is then written as:

$$w(z) = \sum_{i=1}^{N} w_i \theta_i(z) \tag{6.1}$$

where the parameters w_i can be estimated by using the Fisher matrix, namely with $\sqrt{(F^{-1})_{ii}}$, when having marginalised over all the other parameters. To find a basis where all the parameters are uncorrelated we diagonalise the Fisher matrix as $F = W^T \Lambda W$ where Λ is a diagonal matrix and the rows of W are the eigenvectors $e_i(z)$ which form a basis in which the parameters are uncorrelated. The e_i vectors are the so-called principal components. The diagonal elements of Λ, λ_i, determine how well are measured the parameters. We define the variance as $\sigma_i^2(\alpha_i) = \frac{1}{\lambda_i}$. The eigenvalues are ordered as $\lambda_1 > \lambda_2 > ... > \lambda_N$ which means that the first mode has the lowest variance and thus correspond to the best measured parameter.

The eos can be now written as:

$$w(z) = \sum_{i=1}^{N} \alpha_i e_i(z) \tag{6.2}$$

Since F is real and symetric W can be chosen so that the basis $e_i(z)$ form an orthonormal basis. Using this orthonormality the coefficients α_i are calculated as:

$$\alpha_i = \sum_{p=1}^{N} w(z_p) e_i(z_p) \tag{6.3}$$

6.1.2 Building the Fisher matrix

Following Amendola et al. [2012] the Fisher Matrix can be expressed as:

$$F_{kl} \equiv \left.\frac{\partial^2 lnL}{\partial w_k \partial w_l}\right|_{w_{fid}} = \sum_{i,j=1}^{N} \left.\frac{\partial \mu(z_i)}{\partial w_k}\right|_{w_{fid}} D_{ij}^{-1} \left.\frac{\partial \mu(z_j)}{\partial w_l}\right|_{w_{fid}} \tag{6.4}$$

where L is the likelihood of the following generic observable:

$$m(z_i, w_i, c) = \mu(z_i, w_i) + c$$

- In the case of supernovae: $\mu(z_i, w_i) = 5log(H_0 d_L)$ and $c = M + 25 - 5log(H_0)$

- In the case of alpha measurements: $\mu(z_i, w_i) = ln([\kappa(\phi - \phi_0)]$ and $c = ln(\zeta)$

The marginalised likelihood in the parameters w_i can be expressed as:

$$L(w_i) = \sqrt{\frac{2\pi}{A}} exp\left[-\frac{1}{2}\sum_{i,j=1}^{N} (\mu - \mu_{fid})_i \, D_{ij}^{-1} \, (\mu - \mu_{fid})_j\right] \tag{6.5}$$

where

$$A = \sum_{i,j} C_{ij}^{-1}$$

with C the covariance matrix of the data, and

$$D_{ij}^{-1} = C_{ij}^{-1} - \frac{1}{A}\sum_{k,l} C_{kj}^{-1} C_{li}^{-1}$$

We have selected two fiducial models from the first (quantitative) analysis we have made in this work, as they are parametrised in a polynomial form it is simpler to show their evolution in the Fig. 6.1. We have selected quite distinguishable equation of states on purpose to perform a first qualitative test of the method.

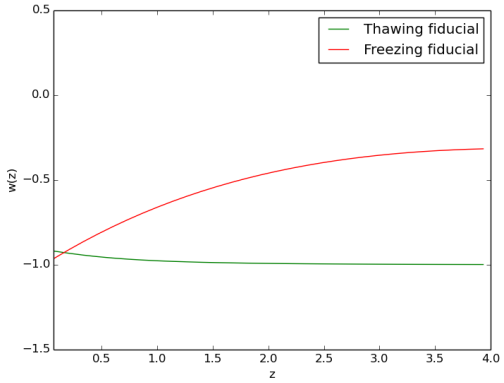

Figure 6.1: Evolution of the equation of state for the thawing and freezing fiducial models.

6.1.3 Mock data

To test the PCA we will simulate two types of data, SNeIa data and alpha measurements. - For the SNeIa data we use 3000 SNeIa over the redshift range $0 < z < 1.7$ with an uncertainty on the magnitude of $\sigma_m = 0.11$ which is representative of a "SNAP-like" survey and also used by Huterer and Starkman [2003]

- For the alpha measurements we will use two different scenarios described in Tab. 6.1 for the spectrographs ESPRESSO at the VLT and HIRES at the E-ELT. The QSO are distributed uniformly over the redshift range and the uncertainties are the same for all measurements.

Table 6.1: Different scenarios used for the reconstruction using QSO data

Scenario	redshift range	ESPRESSO	HIRES
Baseline	$0.5 < z < 4$	30 systems $\sigma_{\frac{\Delta\alpha}{\alpha}} = 6 \times 10^{-7}$	100 systems $\sigma_{\frac{\Delta\alpha}{\alpha}} = 10^{-7}$
Ideal	$0.5 < z < 4$	100 systems $\sigma_{\frac{\Delta\alpha}{\alpha}} = 2 \times 10^{-7}$	150 $\sigma_{\frac{\Delta\alpha}{\alpha}} = 3 \times 10^{-8}$

6.1.4 Selection of the number of modes

Risk method

As defined in Huterer and Starkman [2003] one method to decide how many modes (or components) have to be kept for the reconstruction is the so-called risk method. The risk is defined as

$risk = bias^2 + variance$:

$$risk = \sum_{i=1}^{N} (w(z_i) - w_{fid}(z_i))^2 + \sum_{i=1}^{N} \sigma^2(w(z_i)) \tag{6.6}$$

where w_{fid} is the fiducial value of w. The risk is calculated for each number of component. The number of components to keep is the one corresponding to the minimum value of the risk.
The variance increases with the number of modes kept on the contrary of the bias. It means that the reconstruted value of the eos will be closer to the fiducial value when keeping a lot of modes. However the variance increases with the number of modes kept so the error bars are more and more important with a bigger number of modes kept.

Normalisation method

An other method given by Albrecht et al. [2009] chooses the number of modes to keep by deciding that the largest aceptable value of the variance σ_i^2 has to be below unity since in this case it limits the variation of the equation of state to be of the order of unity: $\langle (1 + w(z))^2 \rangle = \sigma_i^2$. We call this method normalisation beause Albrecht et al. [2009] proposed to normalise the sigmas as:

$$\frac{1}{\sigma_i} = 1 + \frac{1}{\sigma_i} \quad \rightarrow \quad \sigma_{ni} = \frac{\sigma_i}{1 + \sigma_i} \tag{6.7}$$

in order to have $\sigma_{ni} = 1$ in the worst case. In our study we have discarded modes with $\sigma^2 > 1$ before the normalisation.

6.1.5 PCA results

The results we present here are aimed to provide an intuitive overview on the most suitable combination of datasets and observational facilities to distinguish among a freezing and a thawing behavior. It is just a qualitative approach to compare different observational strategies, this recosntruction of the eos can not be compared to the one given by regression models or even Gaussian Processes.
First the reonstruction using supernovae data is shown on the Fig. 6.2. We see that the reconstruction is correctly done for redshifts $z \leq 1$ and then the equation of state converges to zero due to the introduction of a systematic bias in the truncature as explained in Huterer and Starkman [2003]. The error bars of the freezing and the thawing models are overlapping so this configuration is not suitable to distinguish among them.

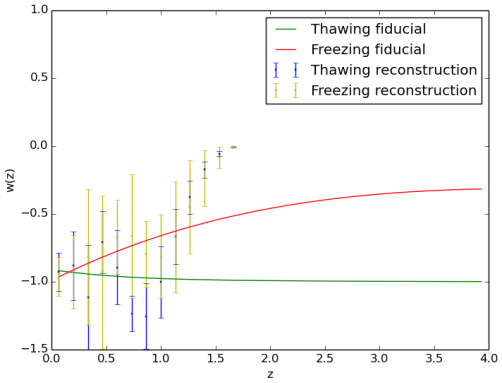

Figure 6.2: Reconstruction of 2 fiducial equations of state representing a thawing and a freezing behaviour. The reconstruction is obtained using SNeIa data only.

In the Fig. 6.3 we add the QSO data observed with ESPRESSO for both baseline and ideal senarios. We see that the reconstruction is done up to $z = 4$ for the ideal case and up to $z = 2.5$ for the freezing model in the baseline scenario before the systematic bias becomes dominant. Both behavior are catched up by the reconstruction and only the ideal scenario contain error bars which not overlapped at a redshift $z > 2.5$, thus allowing a distinction.

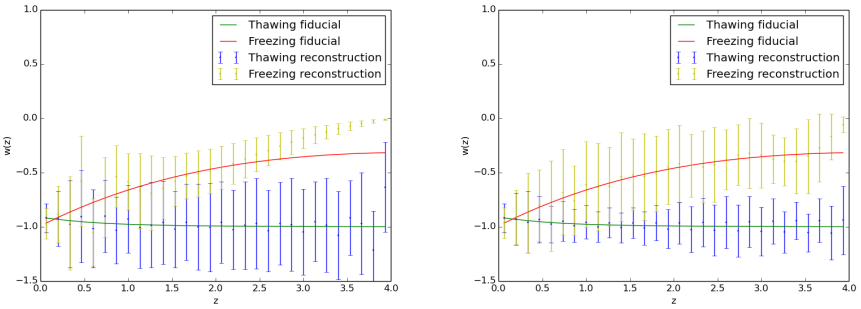

Figure 6.3: Reconstruction of 2 fiducial equation of state representing a thawing and a freezing behaviour. The reconstruction is obtained using SNeIa data and the QSO data with the Espresso baseline scenario (*left*) and the ideal scenario (*right*).

In the Fig. 6.4 we use the QSO data observed with the spectrograph HIRES for both baseline and ideal senarios. We see that the reconstruction is done reliably up to $z = 4$ for both scenarios. Both behavior are also well matched by the reconstruction. In the baseline scenario the error bars stop overlapping for redshifts $z > 2.5$ as in the ideal case with ESPRESSO. In the ideal scenario they already stop overlapping at a redshift $z \simeq 1$. In conclusion with our assumptions HIRES would be the most suitable observational facility to distinguish a freezing behavior from a thawing one, and already from redshift around 1.

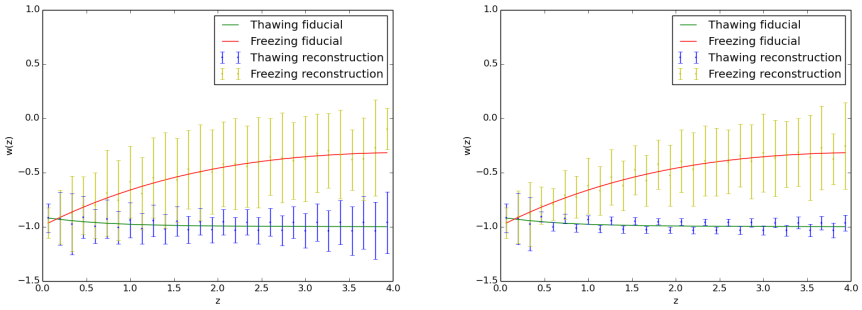

Figure 6.4: Reconstruction of 2 fiducial equations of state representing a thawing and a freezing behaviour. The reconstruction is obtained using SNeIa data and the QSO data with the HIRES baseline scenario (*left*) and the ideal scenario (*right*).

However this reconstruction depends strongly on the number of modes which are seleted as shown in Fig. 6.5 where the reconstruction in the ideal scenario for HIRES is performed for the risk and normalisation methods. The risk method selects less modes (see 6.2) and thus enables lower uncertainties with the cost of a worst expected mean for the eos. Even if both methods give different reconstructions, the behavior of the freezing and the thawing model are well identified with the risk method too and as the error bars are lower they stop overlapping at a smaller redshift. We can then consider the normalisation method as the ”worst case”.

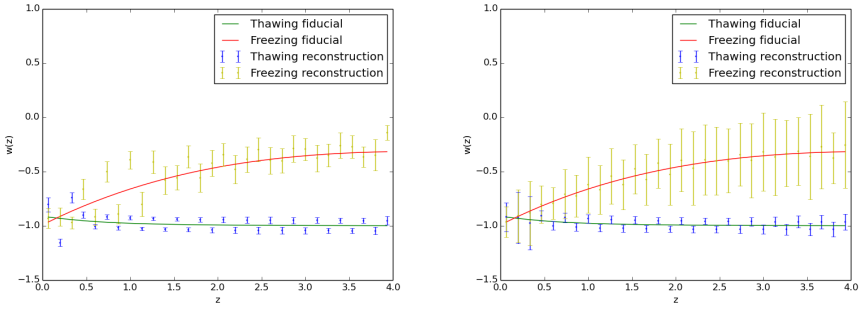

Figure 6.5: Reconstruction of 2 fiducial equations of state representing a thawing and a freezing behaviour. The reconstruction is obtained using SNeIa data and the QSO data with the HIRES ideal scenario. *Left:* number of modes selected by the risk method. *Right:* number of modes selected with the normalisation method.

It will be of interest to study whether this method might reconstruct reliably a non-monotonic freezing model. As this qualitative study shows the role that the alpha measurements might play in distinguishing different eos behaviors, the next step will be to determine the maximum deviation potentially detectable by the given sensibility of ESPRESSO and HIRES.
One can also use this method to optimize an observational strategy. Given the accuracy of the spectrograph which will be used, it might be used to select the appropriated targets, in our case

Table 6.2: Number of modes selected for the reconstruction seen is Fig. 6.5 using either the risk method or the normalisation one.

	Risk method	Normalisation method
Freezing	19	26
Thawing	27	29

for distinguishing freezing and thawing models.

6.2 Gaussian Processes

Gaussian Processes have been used recently to reconstruct the eos of dark energy and other cosmological parameters such as the deceleration parameter and the Hubble parameter as a function of the redshift Holsclaw et al. [2010b,a, 2011], Seikel et al. [2012], Seikel and Clarkson [2013], Nair et al. [2014]. There are two different approaches, one was followed by Holsclaw et al. [2011] and consists in fitting the equation of state as a GP and confront this reconstruction with the data. The other method consists in fitting the data, SNeIa or Hubble parameter, with a Gaussian Process to obtain the luminosity distance and its derivatives and then express the eos (or any cosmological parameter) as a function of the luminosity distance and its derivatives Seikel et al. [2012], Nair et al. [2014].

We will follow the second method, i.e. extracting information from the data to evaluate the reconstruction of the alpha variation. We will try to follow two approaches. The first one is to express $\frac{\Delta\alpha}{\alpha}$ in terms of the Hubble rate and its derivative and use the GP to reconstruct the Hubble rate and its derivative with SNeIa or Hubble rate data, and then propagate the error to obtain the evolution of $\frac{\Delta\alpha}{\alpha}$.

The second approach is to express the eos in terms of $\frac{\Delta\alpha}{\alpha}$ and its derivatives and use the GP to reconstruct $\frac{\Delta\alpha}{\alpha}$ and its derivatives with alpha measurements.

6.2.1 Definition

A Gaussian Process (GP) is defined as a distribution over functions. Considering a function f described by a GP, its value at a point x is drawn from a Gaussian distribution with mean $m(x)$ and a variance $Var(x)$. The value at a point x is also dependent on the values at other positions x', this dependence is described by the covariance function $cov(f(x), f(x')) = k(x, x')$. The GP is written as $f \sim GP\left(m(x), k(x, x')\right)$. For a complete description of Gaussian Processes we refer to Rasmussen and Williams [2006].

The covariance function $k(x, x')$, also called kernel, can be chosen from a wide range of possibilities depending on the properties we want the data to have (for instance isotropy, weak dependence for well separated points...). In this work we will use the standard squared exponential covariance function:

$$k(x, x') = \sigma_f exp\left(-\frac{(x - x')^2}{2l^2}\right) \tag{6.8}$$

This function has the advantage to be infinetely differentiable. We see that 2 points very close to each other have a maximum covariance and 2 points far away from each other a zero covariance

function. It means that we assume that data points are more correlated to the closest points, it follows a smooth evolution. The parameters l and σ_f are called hyperparemeters and correspond to the typical change in $f(x)$ in the x and y-axis respectively.

If we consider a data set $\mathcal{D} = (x_i, y_i)$ with N observations, the aim is to construct a function $f(x)$ describing the data. The training set, containing the observations, is written $\boldsymbol{X}$ and the positions at which we want to evaluate the function is written $\boldsymbol{X^*}$. The observations are assumed to be scaterred around the values given by the function f: $y_i = f(x_i) + \epsilon_i$ where ϵ_i represents a Gaussian noise with variance σ_i^2. The given data $\boldsymbol{y}$ are then described by a GP as:

$$\boldsymbol{y} \sim \mathcal{N}(\boldsymbol{\mu}, K(\boldsymbol{X}, \boldsymbol{X}) + C) \tag{6.9}$$

where $\boldsymbol{\mu} = m(\boldsymbol{X})$ and C is the covariance matrix of the data and the matrix $K(\boldsymbol{X}, \boldsymbol{X})_{ij} = k(x_i, x_j)$.
The function evaluated at $\boldsymbol{X^*}$ is written $\boldsymbol{f^*}$ and expressed as:

$$\boldsymbol{f^*} \sim \mathcal{N}(\boldsymbol{\mu^*}, K(\boldsymbol{X^*}, \boldsymbol{X^*})) \tag{6.10}$$

where $\boldsymbol{\mu^*} = m(\boldsymbol{X^*})$ is the mean of $\boldsymbol{f^*}$.
Given the data $\boldsymbol{y}$ we want to reconstruct $\boldsymbol{f^*}$, the joint probability of 2 GPs is given by:

$$\begin{bmatrix} \boldsymbol{y} \\ \boldsymbol{f^*} \end{bmatrix} \sim \mathcal{N}\left(\begin{bmatrix} \boldsymbol{\mu} \\ \boldsymbol{\mu^*} \end{bmatrix}, \begin{bmatrix} K & K^* \\ K^* & K^{**} \end{bmatrix} \right) \tag{6.11}$$

where $K = K(\boldsymbol{X}, \boldsymbol{X})$, $K^* = K(\boldsymbol{X^*}, \boldsymbol{X}) = K(\boldsymbol{X}, \boldsymbol{X^*})$ and $K^{**} = K(\boldsymbol{X^*}, \boldsymbol{X^*})$.
The conditional distribution of $\boldsymbol{f^*}$ given the data, which represents the posterior distribution of the function given the data, is:

$$\boldsymbol{f^*} | \boldsymbol{X^*}, \boldsymbol{X}, \boldsymbol{y} \sim \mathcal{N}(\overline{\boldsymbol{f^*}}, cov(\boldsymbol{f^*})) \tag{6.12}$$

where

$$\overline{\boldsymbol{f^*}} = \boldsymbol{\mu^*} + K^* K^{-1} \boldsymbol{y} \tag{6.13}$$

$$cov(\boldsymbol{f^*}) = K^{**} - K^* K^{-1} K^* \tag{6.14}$$

Similarly we can construct the posterior distribution function of the GP and its derivative (See detailed description in Seikel et al. [2012] and Nair et al. [2014])

6.2.2 Gaussian Processes results

Reconstruction of $\frac{\Delta\alpha}{\alpha}$ using the luminosity distance (or Hubble rate)

The aim of this reconstruction is to study whether the supernovae and Hubble rate data might bring constraints on the scalar field causing the expansion of the Universe and thus to alpha measurements in the case where the scalar field causing a variation in alpha causes also the expansion of the Universe and is of quintessence type. This method might constrain the coupling factor ζ

Recalling the equations describing the scalar field dynamics of a quintessence field 2.17a and 2.17b, we can rearrange them to express the potential and the velocity of the field as functions of the Hubble parameter and its derivatives:

$$\begin{cases} \dfrac{8\pi G}{3H_0^2}V(z) = \dfrac{H^2}{H_0^2} - \dfrac{(1+z)}{3H_0^2}HH' - \dfrac{\Omega_m(1+z)^3}{2} & \text{(6.15a)} \\ \dfrac{8\pi G}{3H_0^2}\dot{\phi}^2(z) = \dfrac{2(1+z)}{3H_0^2}HH' - \Omega_m(1+z)^3 & \text{(6.15b)} \end{cases}$$

Where the prime denotes a derivative with respect to the redshift.

Using the equations 4.6 and 6.15b, we can also express $\frac{\Delta\alpha}{\alpha}$ in terms of the Hubble parameter and its derivatives as:

$$\frac{\Delta\alpha}{\alpha} = \zeta \int_0^z \sqrt{2\frac{H'}{H(1+z')} - 3\frac{H_0^2}{H^2}\Omega_m(1+z')}\,\mathrm{d}z' \tag{6.16}$$

If we know the Hubble parameter at different redshift we can then use the GP method to reconstruct H and H'. If we use SNeIa data we have to use the definiton of the luminosity distance in a flat FLRW Universe:

$$D_L(z) = \frac{c(1+z)}{H_0}\int_0^z \frac{H_0}{H(z')}\,\mathrm{d}z' \tag{6.17}$$

In this case, following Holsclaw et al. [2011] we define the distance as $D(z) = H_0 D_L(z)$, and the Hubble rate becomes in terms of $D(z)$ and its derivative:

$$H(z) = \frac{cH_0(1+z)^2}{D'(z)(1+z) - D(z)} \tag{6.18}$$

To perform the Gaussian Process we have used the publicly available code "GaPP: Gaussian Processes in Python" Seikel et al. [2013]. So far we have obtained the reconstruction of the distance $D(z)$ and its derivatives as showed in Fig. 6.6. The next step is the calculation the Eq. 6.16 using these reconstructions. Some work has still to be done to propagate the errors through the integral. So far, the use of Taylor series seems to be the best solution to deal with fraction and integral in error propagation process.

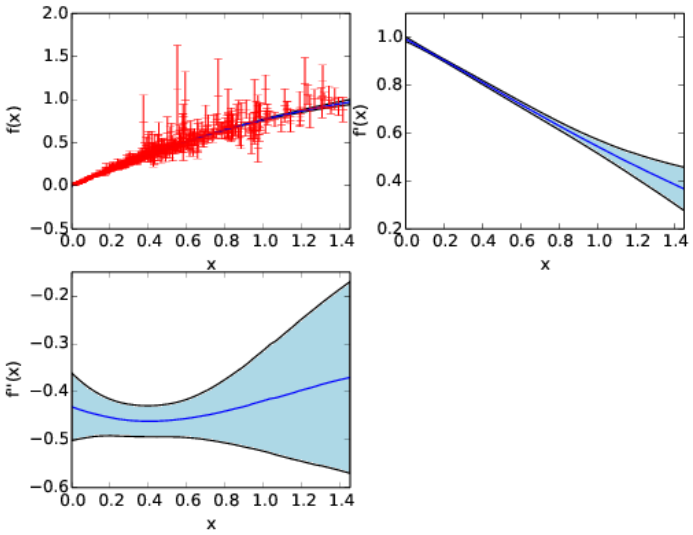

Figure 6.6: Reconstruction of the luminosity distance and its first and second derivative using the Gaussian Process method. The Union2.1 dataset was used. The blue line represents the expected value and the blue shaded region represents the 1σ uncertainty.

Reconstruction of the eos of dark energy using alpha measurements

Another way to use the GP is to use the alpha measurements to reconstruct the equation of dark energy. The aim is to compare the reconstruction of the eos given by the alpha measurements with the one by the SNeIa. This method might also constrain the coupling factor ζ. The Eq. 4.10 gives a relation between the eos and $\frac{\Delta\alpha}{\alpha}$:

$$\frac{\Delta\alpha}{\alpha}(z) = \zeta \int_0^z \sqrt{3\Omega_\phi(z)\,(1+w_\phi(z))}\frac{dz'}{1+z'}\,. \tag{6.19}$$

when rearranging this equation to express the eos in terms of $\frac{\Delta\alpha}{\alpha}$ and its derivatives we obtain:

$$w(z) = \frac{2}{3}(1+\frac{\beta''}{\beta'}) - \frac{1}{3}\left[\frac{3\zeta^2\Omega_\phi w'(1+z) - 2\Omega_\phi\beta''\beta'(1+z)^3 - 2\Omega_\phi\beta'^2(1+z)^2}{3\zeta^2\Omega_\phi(1+w) - \Omega_\phi\beta'^2(1+z)^2}\right] \tag{6.20}$$

where $\beta = \frac{\Delta\alpha}{\alpha}$ and Ω_ϕ is the current density parameter of the scalar field, responsible for the expansion of the Universe here.

It follows that a differential equation of order 1 has to be solved to obtain the reconstruction of w using alpha measurements.

The reconstruction of $\frac{\Delta\alpha}{\alpha}$ is seen on Fig. 6.7. We see that the errors for the derivatives are huge and do not allow to reconstruct the eos. This comes from the fact that a lot of measurements are at about the same redshift with sensibly different value and error bars. As the choice of the squared exponential as the covariance function implies that close points are more correlated, an other choice might improve the reconstruction a bit.

If we only consider the Keck Fig. 6.8 or the VLT 6.9 dataset alone then the reconstruction gives more convenient errors for the derivatives mainly due to the smaller number of points in each dataset.

Some work has still to be done for reconstructiong the eos using the Keck and VLT dataset separately, i.e to solve the equation 6.20.

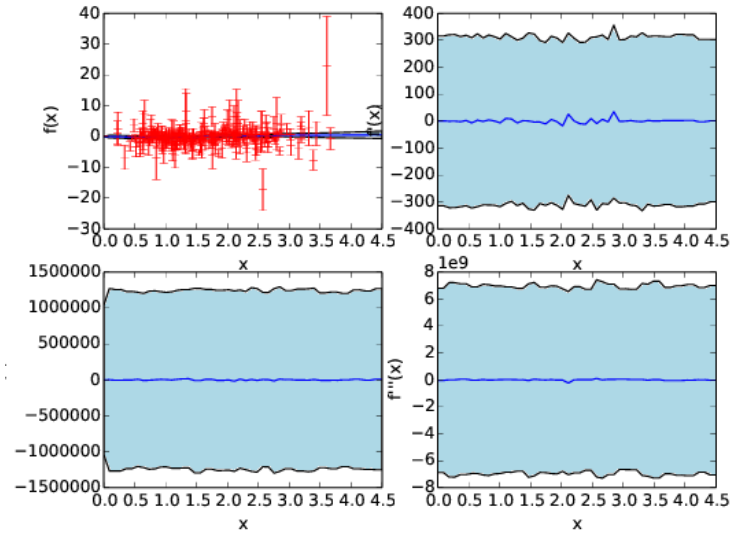

Figure 6.7: Reconstruction of $\frac{\Delta\alpha}{\alpha}$ and its first, second and third derivatives using the Gaussian Process method. The Keck and VLT datasets are combined. The blue line represents the expected value and the blue shaded region represents the 1σ uncertainty. (The y-axis scale is in $1e^{-5}$)

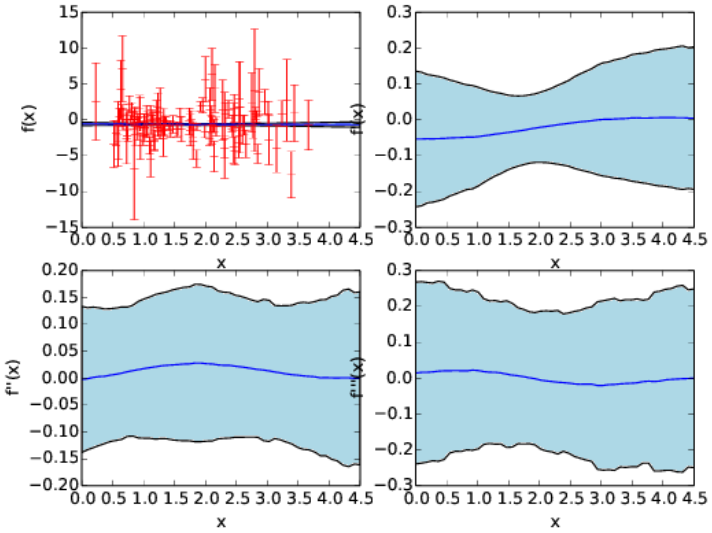

Figure 6.8: Reconstruction of $\frac{\Delta\alpha}{\alpha}$ and its first, second and third derivatives using the Gaussian Process method. Only the Keck dataset is used. The blue line represents the expected value and the blue shaded region represents the 1σ uncertainty.(The y-axis scale is in $1e^{-5}$)

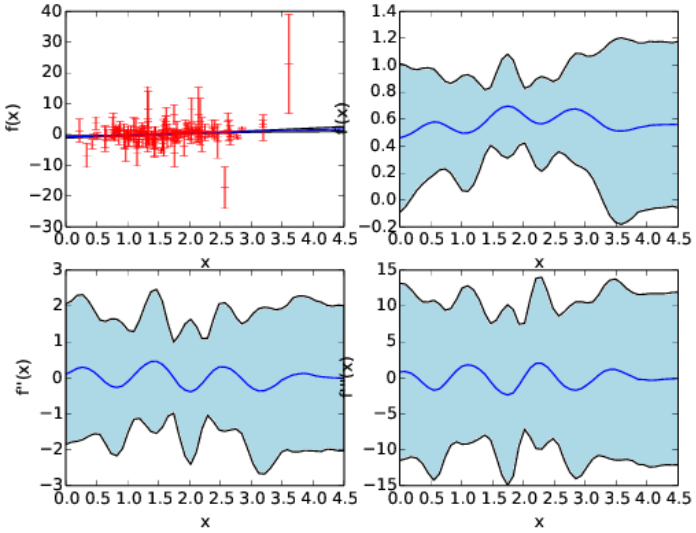

Figure 6.9: Reconstruction of $\frac{\Delta\alpha}{\alpha}$ and its first, second and third derivatives using the Gaussian Process method. Only the VLT dataset is used. The blue line represents the expected value and the blue shaded region represents the 1σ uncertainty.(The y-axis scale is in $1e^{-5}$)

Chapter 7.

Conclusion

In this work we have studied the role that the fine-structure constant measurements might play in constraining the dark energy equation of state as it is one of the only observable which allows to probe up to redshifts $z \sim 4$.

First we have performed a quantitative analysis by simulating various quintessence-like potentials in order to study the behavior of the equation of state of dark energy. We have classified this behavior in 2 categories following Caldwell and Linder [2005], namely *thawing* and *freezing*, depending on the fact that the eos is coming closer to -1 or going away from -1 respectively. Given these evolutions of the equation of states and of the dark energy density parameters we could study the corresponding evolution of the observable quantity $\frac{\Delta\alpha}{\alpha}$ with respect to the redshift. As the freezing models have a larger variation in $\frac{\Delta\alpha}{\alpha}$ we have shown qualitatively that the sensitivity of the spectrograph ESPRESSO at the VLT will allow to distinguish among a freezing and a thawing model in most of the cases. Current observational facilities do not have the required sensitivity. We have also studied the redshift drift signal for these models and did not see any differences in the pattern of these signal which might help to distinguish a freezing from a thawing model.

In the second analysis, which is a parametric study, we have shown that even the current alpha measurements might be used to constrain a dynamical equation of state. In the case of the CPL parametrisation a better constrain on the parameters w_a is obtained and lower values of Ω_m are also discarded, in comparison to SNeIa and Hubble rate data. In the case of quintessence-like potentials the calculations showed that the current datasets do not bring tighter constraints on the parameters than by using only the SNeIa and Hubble rate datasets.

In the non-parametric study, we have first used the Principal Component Analysis to study whether the spectrographs ESPRESSO and HIRES at the E-ELT will have the required sensitivity, under

some assumptions, to distinguish our 2 fiducial models correponding to a freezing and thawing one. It resulted that for almost all scenarios it will allow to do it. It will be interesting to use this technique in the close future to plan observational strategies by selecting specific targets. Giving a list of targets and a more specific estimation of the sensitivity of the measurement this technique might be used to select the most suitable targets to probe dark energy.

Regarding to the Gaussian Process technique, the theoretical background has been set and some work is still necessary to propagate the uncertainty of the reconstructed quantities (d_L or $\frac{\Delta\alpha}{\alpha}$) to enable a complete overview of the technique. However, from the first results it appears that the high scattering of the alpha measurements is problematic for reconstructing $\frac{\Delta\alpha}{\alpha}$ and its derivative using a Gaussian Process. Future ESPRESSO and ELT-HIRES data will improve this and it it will be interesting to test this technique with some simulated data. The other method using a reconstruction of the Hubble rate and its derivative seems more promising to constrain the coupling factor ζ.

This work has shown that the current alpha measurements already bring tighter constraints on a dynamical equation of state than the supernovae and Hubble rate data. However the current measurements are accurate enough to distinguish a freezing from a thawing behavior. The quantitative approach confirmed by the PCA analysis showed that ESPRESSO at the VLT and HIRES at the E-ELT will able to do so. And the PCA technique can be used to optimize the selection of the targets to try to detect which behavior exhibits the equation of state.

Bibliography

Georges Aad et al. Combined Measurement of the Higgs Boson Mass in pp Collisions at $\sqrt{s} = 7$ and 8 TeV with the ATLAS and CMS Experiments. *Phys.Rev.Lett.*, 114:191803, 2015. 10.1103/PhysRevLett.114.191803.

A. Albrecht, L. Amendola, G. Bernstein, D. Clowe, D. Eisenstein, L. Guzzo, C. Hirata, D. Huterer, R. Kirshner, E. Kolb, and R. Nichol. Findings of the Joint Dark Energy Mission Figure of Merit Science Working Group. *ArXiv e-prints*, January 2009. URL http://adsabs.harvard.edu/abs/2009arXiv0901.0721A.

L. Amendola, A. C. O. Leite, C. J. A. P. Martins, N. J. Nunes, P. O. J. Pedrosa, and A. Seganti. Variation of fundamental parameters and dark energy: A principal component approach. *prd*, 86(6):063515, September 2012. 10.1103/PhysRevD.86.063515.

Luis Anchordoqui and Haim Goldberg. Time variation of the fine structure constant driven by quintessence. *Phys. Rev.*, D68:083513, 2003. 10.1103/PhysRevD.68.083513.

W.D. Arnett. *Astrophysical Journal*, (253):785:797, 1982.

P. P. Avelino, S. Esposito, G. Mangano, C. J. A. P. Martins, A. Melchiorri, G. Miele, O. Pisanti, G. Rocha, and Pedro T. P. Viana. Early universe constraints on a time varying fine structure constant. *Phys. Rev.*, D64:103505, 2001. 10.1103/PhysRevD.64.103505.

P. P. Avelino, C. J. A. P. Martins, Nelson J. Nunes, and K. A. Olive. Reconstructing the dark energy equation of state with varying couplings. *Phys. Rev.*, D74:083508, 2006. 10.1103/PhysRevD.74.083508.

J. D. Bekenstein. Fine Structure Constant: Is It Really a Constant? *Phys. Rev.*, D25:1527–1539, 1982. 10.1103/PhysRevD.25.1527.

L. Bergstrom, S. Iguri, and H. Rubinstein. Constraints on the variation of the fine structure constant from big bang nucleosynthesis. *Phys. Rev.*, D60:045005, 1999. 10.1103/PhysRevD.60.045005.

Chris Blake et al. The WiggleZ Dark Energy Survey: Joint measurements of the expansion and growth history at z ¡ 1. *Mon. Not. Roy. Astron. Soc.*, 425:405–414, 2012. 10.1111/j.1365-2966.2012.21473.x.

P. Bonifacio, S. Cristiani, and M. Dessauges. Codex phase a science case. Report E-TRE-IOA-573-0001 Issue 1, E-ELT PROGRAMME, 2010. URL http://www.iac.es/proyecto/codex/pages/documents.php.

N. G. Busca, T. Delubac, J. Rich, S. Bailey, A. Font-Ribera, D. Kirkby, J.-M. Le Goff, M. M. Pieri, A. Slosar, É. Aubourg, J. E. Bautista, D. Bizyaev, M. Blomqvist, A. S. Bolton, J. Bovy, H. Brewington, A. Borde, J. Brinkmann, B. Carithers, R. A. C. Croft, K. S. Dawson, G. Ebelke, D. J. Eisenstein, J.-C. Hamilton, S. Ho, D. W. Hogg, K. Honscheid, K.-G. Lee, B. Lundgren, E. Malanushenko, V. Malanushenko, D. Margala, C. Maraston, K. Mehta, J. Miralda-Escudé, A. D. Myers, R. C. Nichol, P. Noterdaeme, M. D. Olmstead, D. Oravetz, N. Palanque-Delabrouille, K. Pan, I. Pâris, W. J. Percival, P. Petitjean, N. A. Roe, E. Rollinde, N. P. Ross, G. Rossi, D. J. Schlegel, D. P. Schneider, A. Shelden, E. S. Sheldon, A. Simmons, S. Snedden, J. L. Tinker, M. Viel, B. A. Weaver, D. H. Weinberg, M. White, C. Yèche, and D. G. York. Baryon acoustic oscillations in the Lyα forest of BOSS quasars. *aap*, 552:A96, April 2013. 10.1051/0004-6361/201220724.

R. R. Caldwell and E. V. Linder. Limits of Quintessence. *Physical Review Letters*, 95(14):141301, September 2005. 10.1103/PhysRevLett.95.141301.

Sean M. Carroll. Quintessence and the rest of the world. *Phys. Rev. Lett.*, 81:3067–3070, 1998. 10.1103/PhysRevLett.81.3067.

Y. Chen, C.-Q. Geng, S. Cao, Y.-M. Huang, and Z.-H. Zhu. Constraints on a phiCDM model from strong gravitational lensing and updated Hubble parameter measurements. *jcap*, 2:010, February 2015. 10.1088/1475-7516/2015/02/010.

M. Chevallier and D. Polarski. Accelerating Universes with Scaling Dark Matter. *International Journal of Modern Physics D*, 10:213–223, 2001. 10.1142/S0218271801000822.

Takeshi Chiba and Kazunori Kohri. Quintessence cosmology and varying alpha. *Prog. Theor. Phys.*, 107:631–636, 2002. 10.1143/PTP.107.631.

C.-H. Chuang and Y. Wang. Modelling the anisotropic two-point galaxy correlation function on small scales and single-probe measurements of H(z), D_A(z) and f(z)σ_8(z) from the Sloan Digital Sky Survey DR7 luminous red galaxies. *mnras*, 435:255–262, October 2013. 10.1093/mnras/stt1290.

E. J. Copeland, N. J. Nunes, and M. Pospelov. Models of quintessence coupled to the electromagnetic field and the cosmological evolution of alpha. *Phys. Rev.*, D69:023501, 2004. 10.1103/PhysRevD.69.023501.

Edmund J. Copeland, M. Sami, and Shinji Tsujikawa. Dynamics of dark energy. *Int. J. Mod. Phys.*, D15:1753–1936, 2006. 10.1142/S021827180600942X.

P.-S. Corasaniti, D. Huterer, and A. Melchiorri. Exploring the dark energy redshift desert with the Sandage-Loeb test. *Phys. Rev. D*, 75(6):062001, March 2007. 10.1103/PhysRevD.75.062001.

Pier-Stefano Corasaniti, Dragan Huterer, and Alessandro Melchiorri. Exploring the Dark Energy Redshift Desert with the Sandage-Loeb Test. *Phys. Rev.*, D75:062001, 2007. 10.1103/PhysRevD.75.062001.

M.K. Cowles and B. P. Carlin. *Journal of the American Statistical Association*, 91:883, 1996.

Thibault Damour and Freeman Dyson. The Oklo bound on the time variation of the fine structure constant revisited. *Nucl. Phys.*, B480:37–54, 1996. 10.1016/S0550-3213(96)00467-1.

G. Dvali and M. Zaldarriaga. Changing α with Time: Implications for Fifth-Force-Type Experiments and Quintessence. *Physical Review Letters*, 88(9):091303, March 2002. 10.1103/PhysRevLett.88.091303.

V. A. Dzuba, V. V. Flambaum, and J. K. Webb. Space-Time Variation of Physical Constants and Relativistic Corrections in Atoms. *Physical Review Letters*, 82:888–891, February 1999. 10.1103/PhysRevLett.82.888.

Martin Eriksson and Rahman Amanullah. Fitting inverse power law quintessence models using the SNAP satellite. *Phys. Rev.*, D66:023530, 2002. 10.1103/PhysRevD.66.023530.

O. Farooq and B. Ratra. Hubble Parameter Measurement Constraints on the Cosmological Deceleration-Acceleration Transition Redshift. *ApJ*, 766:L7, March 2013. 10.1088/2041-8205/766/1/L7.

D. Foreman-Mackey, D. W. Hogg, D. Lang, and J. Goodman. emcee: The MCMC Hammer. *pasp*, 125:306–312, March 2013. 10.1086/670067.

Peter G. O. Freund and Mark A. Rubin. Dynamics of Dimensional Reduction. *Phys. Lett.*, B97: 233–235, 1980. 10.1016/0370-2693(80)90590-0.

Yasunori Fujii, Akira Iwamoto, Tokio Fukahori, Toshihiko Ohnuki, Masayuki Nakagawa, Hiroshi Hidaka, Yasuji Oura, and Peter Moller. The Nuclear interaction at Oklo two billion years ago. *Nucl. Phys.*, B573:377–401, 2000. 10.1016/S0550-3213(00)00038-9.

D. Gamerman and H. Lopes. *Markov Chain Monte Carlo: Stochastic Simulation for Bayesian Inference*. Chapman, second edition, 2006.

Enrique Gaztanaga, Anna Cabre, and Lam Hui. Clustering of Luminous Red Galaxies IV: Baryon Acoustic Peak in the Line-of-Sight Direction and a Direct Measurement of H(z). *Mon. Not. Roy. Astron. Soc.*, 399:1663–1680, 2009. 10.1111/j.1365-2966.2009.15405.x.

J. Goodman and J. Weare. Ensemble samplers with affine invariance. *Comm. App. Math. Comp. Sci.*, 5(1):65, 2010.

C. R. Gould, E. I. Sharapov, and S. K. Lamoreaux. Time variability of alpha from realistic models of Oklo reactors. *Phys. Rev.*, C74:024607, 2006. 10.1103/PhysRevC.74.024607.

K. M. Hanson. Markov Chain Monte Carlo posterior sampling with the Hamiltonian method. *Medical Imaging: Image Processing*, 4322:456–467.

W. K. Hastings. Monte Carlo Sampling Methods Using Markov Chains and Their Applications. *Biometrika*, 57:97–109, 1970. 10.1093/biomet/57.1.97.

W. Hillebrandt and J. C. Niemeyer. Type IA Supernova Explosion Models. *araa*, 38:191–230, 2000. 10.1146/annurev.astro.38.1.191.

Tracy Holsclaw, Ujjaini Alam, Bruno Sanso, Herbert Lee, Katrin Heitmann, Salman Habib, and David Higdon. Nonparametric Reconstruction of the Dark Energy Equation of State. *Phys. Rev.*, D82:103502, 2010a. 10.1103/PhysRevD.82.103502.

Tracy Holsclaw, Ujjaini Alam, Bruno Sanso, Herbert Lee, Katrin Heitmann, Salman Habib, and David Higdon. Nonparametric Dark Energy Reconstruction from Supernova Data. *Phys. Rev. Lett.*, 105:241302, 2010b. 10.1103/PhysRevLett.105.241302.

Tracy Holsclaw, Ujjaini Alam, Bruno Sanso, Herbie Lee, Katrin Heitmann, Salman Habib, and David Higdon. Nonparametric Reconstruction of the Dark Energy Equation of State from Diverse Data Sets. *Phys. Rev.*, D84:083501, 2011. 10.1103/PhysRevD.84.083501.

D. Huterer and H. V. Peiris. Dynamical behavior of generic quintessence potentials: Constraints on key dark energy observables. *prd*, 75(8):083503, April 2007. 10.1103/PhysRevD.75.083503.

Dragan Huterer and Glenn Starkman. Parameterization of dark-energy properties: A Principal-component approach. *Phys. Rev. Lett.*, 90:031301, 2003. 10.1103/PhysRevLett.90.031301.

Kazuhide Ichikawa and M. Kawasaki. Constraining the variation of the coupling constants with big bang nucleosynthesis. *Phys. Rev.*, D65:123511, 2002. 10.1103/PhysRevD.65.123511.

Raul Jimenez and Abraham Loeb. Constraining cosmological parameters based on relative galaxy ages. *Astrophys. J.*, 573:37–42, 2002. 10.1086/340549.

S. Joudaki. Constraints on neutrino mass and light degrees of freedom in extended cosmological parameter spaces. *prd*, 87(8):083523, April 2013. 10.1103/PhysRevD.87.083523.

J. A. King, J. K. Webb, M. T. Murphy, V. V. Flambaum, R. F. Carswell, M. B. Bainbridge, M. R. Wilczynska, and F. E. Koch. Spatial variation in the fine-structure constant - new results from VLT/UVES. *MNRAS*, 422:3370–3414, June 2012. 10.1111/j.1365-2966.2012.20852.x.

S. Kumar, A. Jana, and A. A. Sen. ScalPy: A Python Package For Late Time Scalar Field Cosmology. *ArXiv e-prints*, March 2015. URL http://adsabs.harvard.edu/abs/2015arXiv150302407K.

Andrei D. Linde. Chaotic Inflation. *Phys. Lett.*, B129:177–181, 1983. 10.1016/0370-2693(83)90837-7.

E. V. Linder. Exploring the Expansion History of the Universe. *Physical Review Letters*, 90(9): 091301, March 2003. 10.1103/PhysRevLett.90.091301.

Jochen Liske et al. *Top Level Requirements For ELT-HIRES*, page Document ESO 204697 Version 1, 2014. URL https://www.eso.org/sci/facilities/eelt/docs/ESO-204697_1_Top_Level_Requirements_for_ELT-HIRES.pdf.

A. Loeb. Direct Measurement of Cosmological Parameters from the Cosmic Deceleration of Extragalactic Objects. *ApJ*, 499:L111–L114, June 1998. 10.1086/311375.

R. Maartens. Is the Universe homogeneous? *Royal Society of London Philosophical Transactions Series A*, 369:5115–5137, December 2011. 10.1098/rsta.2011.0289.

Valerio Marra and Francesca Rosati. Cosmological evolution of alpha driven by a general coupling with quintessence. *JCAP*, 0505:011, 2005. 10.1088/1475-7516/2005/05/011.

D. J. E. Marsh, P. Bull, P. G. Ferreira, and A. Pontzen. Quintessence in a quandary: Prior dependence in dark energy models. *Phys. Rev. D*, 90(10):105023, November

2014. 10.1103/PhysRevD.90.105023. URL http://adsabs.harvard.edu/abs/2014PhRvD..90j5023M.

M. Martinelli, S. Pandolfi, C. J. A. P. Martins, and P. E. Vielzeuf. Probing dark energy with redshift drift. *Phys. Rev. D*, 86(12):123001, December 2012. 10.1103/PhysRevD.86.123001.

C. J. A. P. Martins and A. M. M. Pinho. Fine-structure constant constraints on dark energy. *Phys. Rev.*, D91(10):103501, 2015. 10.1103/PhysRevD.91.103501.

Paolo A. Mazzali, Friedrich K. Ropke, Stefano Benetti, and Wolfgang Hillebrandt. A Common Explosion Mechanism for Type Ia Supernovae. *Science*, 315:825, 2007. 10.1126/SCIENCE.1136259.

N. Metropolis, A. W. Rosenbluth, M. N. Rosenbluth, A. H. Teller, and E. Teller. Equation of state calculations by fast computing machines. *J. Chem. Phys.*, 21:1087–1092, 1953. 10.1063/1.1699114.

M. Moresco, A. Cimatti, R. Jimenez, L. Pozzetti, G. Zamorani, M. Bolzonella, J. Dunlop, F. Lamareille, M. Mignoli, H. Pearce, P. Rosati, D. Stern, L. Verde, E. Zucca, C. M. Carollo, T. Contini, J.-P. Kneib, O. Le Fèvre, S. J. Lilly, V. Mainieri, A. Renzini, M. Scodeggio, I. Balestra, R. Gobat, R. McLure, S. Bardelli, A. Bongiorno, K. Caputi, O. Cucciati, S. de la Torre, L. de Ravel, P. Franzetti, B. Garilli, A. Iovino, P. Kampczyk, C. Knobel, K. Kovač, J.-F. Le Borgne, V. Le Brun, C. Maier, R. Pelló, Y. Peng, E. Perez-Montero, V. Presotto, J. D. Silverman, M. Tanaka, L. A. M. Tasca, L. Tresse, D. Vergani, O. Almaini, L. Barnes, R. Bordoloi, E. Bradshaw, A. Cappi, R. Chuter, M. Cirasuolo, G. Coppa, C. Diener, S. Foucaud, W. Hartley, M. Kamionkowski, A. M. Koekemoer, C. López-Sanjuan, H. J. McCracken, P. Nair, P. Oesch, A. Stanford, and N. Welikala. Improved constraints on the expansion rate of the Universe up to z ˜ 1.1 from the spectroscopic evolution of cosmic chronometers. *jcap*, 8:006, August 2012. 10.1088/1475-7516/2012/08/006.

M. T. Murphy, J. K. Webb, V. V. Flambaum, C. W. Churchill, and J. X. Prochaska. Possible evidence for a variable fine structure constant from QSO absorption lines: Systematic errors. *Mon. Not. Roy. Astron. Soc.*, 327:1223, 2001. 10.1046/j.1365-8711.2001.04841.x.

M. T. Murphy, V. V. Flambaum, J. K. Webb, V. A. Dzuba, J. X. Prochaska, and A. M. Wolfe. Constraining Variations in the Fine-Structure Constant, Quark Masses and the Strong Interaction. In S. G. Karshenboim and E. Peik, editors, *Astrophysics, Clocks and Fundamental Constants*, volume 648 of *Lecture Notes in Physics, Berlin Springer Verlag*, pages 131–150, 2004. URL http://adsabs.harvard.edu/abs/2004LNP...648..131M.

Remya Nair, Sanjay Jhingan, and Deepak Jain. Exploring scalar field dynamics with Gaussian processes. *JCAP*, 1401(01):005, 2014. 10.1088/1475-7516/2014/01/005.

Kenneth M. Nollett and Robert E. Lopez. Primordial nucleosynthesis with a varying fine structure constant: An Improved estimate. *Phys. Rev.*, D66:063507, 2002. 10.1103/PhysRevD.66.063507.

K. Nomoto, F.-K. Thielemann, and K. Yokoi. Accreting white dwarf models of Type I supernovae. III - Carbon deflagration supernovae. *apj*, 286:644–658, November 1984. 10.1086/162639.

N. J. Nunes, T. Dent, C. J. A. P. Martins, and G. Robbers. Reconstructing the evolution of dark energy with variations of fundamental parameters . *memsai*, 80:785, 2009. URL http://adsabs.harvard.edu/abs/2009MmSAI..80..785N.

Nelson J. Nunes and James E. Lidsey. Reconstructing the dark energy equation of state with varying alpha. *Phys. Rev.*, D69:123511, 2004. 10.1103/PhysRevD.69.123511.

Keith A. Olive, Maxim Pospelov, Yong-Zhong Qian, Alain Coc, Michel Casse, and Elisabeth Vangioni-Flam. Constraints on the variations of the fundamental couplings. *Phys. Rev.*, D66: 045022, 2002. 10.1103/PhysRevD.66.045022.

F. Pepe, S. Cristiani, R. Rebolo, N. C. Santos, H. Dekker, D. Mégevand, F. M. Zerbi, A. Cabral, P. Molaro, P. Di Marcantonio, M. Abreu, M. Affolter, M. Aliverti, C. Allende Prieto, M. Amate, G. Avila, V. Baldini, P. Bristow, C. Broeg, R. Cirami, J. Coelho, P. Conconi, I. Coretti, G. Cupani, V. D'Odorico, V. De Caprio, B. Delabre, R. Dorn, P. Figueira, A. Fragoso, S. Galeotta, L. Genolet, R. Gomes, J. I. González Hernández, I. Hughes, O. Iwert, F. Kerber, M. Landoni, J.-L. Lizon, C. Lovis, C. Maire, M. Mannetta, C. Martins, M. A. Monteiro, A. Oliveira, E. Poretti, J. L. Rasilla, M. Riva, S. Santana Tschudi, P. Santos, D. Sosnowska, S. Sousa, P. Spanò, F. Tenegi, G. Toso, E. Vanzella, M. Viel, and M. R. Zapatero Osorio. ESPRESSO—An Echelle SPectrograph for Rocky Exoplanets Search and Stable Spectroscopic Observations. *The Messenger*, 153:6–16, September 2013. URL http://esoads.eso.org/abs/2013Msngr.153....6P.

S. Perlmutter et al. Measurements of Omega and Lambda from 42 high redshift supernovae. *Astrophys. J.*, 517:565–586, 1999. 10.1086/307221.

P. Petitjean, R. Srianand, H. Chand, A. Ivanchik, P. Noterdaeme, and N. Gupta. Constraining Fundamental Constants of Physics with Quasar Absorption Line Systems. *ssr*, 148:289–300, December 2009. 10.1007/s11214-009-9520-y.

V. Pettorino, L. Amendola, and C. Wetterich. How early is early dark energy? *Phys. Rev. D*, 87 (8):083009, April 2013. 10.1103/PhysRevD.87.083009.

M. M. Phillips. The absolute magnitudes of Type IA supernovae. *ApJ*, 413:L105–L108, August 1993. 10.1086/186970.

Planck Collaboration, P. A. R. Ade, N. Aghanim, C. Armitage-Caplan, M. Arnaud, M. Ashdown, F. Atrio-Barandela, J. Aumont, C. Baccigalupi, A. J. Banday, and et al. Planck 2013 results. XXIII. Isotropy and statistics of the CMB. *aap*, 571:A23, November 2014. 10.1051/0004-6361/201321534.

Planck Collaboration, P. A. R. Ade, N. Aghanim, M. Arnaud, M. Ashdown, J. Aumont, C. Baccigalupi, A. J. Banday, R. B. Barreiro, J. G. Bartlett, and et al. Planck 2015 results. XIII. Cosmological parameters. *ArXiv e-prints*, February 2015a. URL http://adsabs.harvard.edu/abs/2015arXiv150201589P.

Planck Collaboration, P. A. R. Ade, N. Aghanim, M. Arnaud, M. Ashdown, J. Aumont, C. Baccigalupi, A. J. Banday, R. B. Barreiro, N. Bartolo, and et al. Planck 2015 results. XIV. Dark energy and modified gravity. *ArXiv e-prints*, February 2015b. URL http://adsabs.harvard.edu/abs/2015arXiv150201590P.

R. Rakhi and K. Indulekha. Dark Energy and Tracker Solution- A Review. *ArXiv e-prints*, October 2009. URL http://adsabs.harvard.edu/abs/2009arXiv0910.5406R.

C.E. Rasmussen and K.I. Williams. *Gaussian Processes for Machine Learning*. MIT Press, 2006.

Adam G. Riess et al. Observational evidence from supernovae for an accelerating universe and a cosmological constant. *Astron. J.*, 116:1009–1038, 1998. 10.1086/300499.

C.P. Robert and G. Casella. *Monte Carlo Statistical Methods*. Springer, second edition, 2004.

T. Rosenband, D. Hume, P. Schmidt, C. Chou, A. Brusch, L. Lorini, W. Oskay, W. Drullinger, T. Fortier, J. Stalnaker, S. Diddams, W. Swann, N. Newbury, W. Itano, D. Wineland, and J. Bergquist. *Science*, 319(5871):1808–1812, 2008.

V. C. Rubin, W. K. J. Ford, and N. . Thonnard. Rotational properties of 21 SC galaxies with a large range of luminosities and radii, from NGC 4605 /R = 4kpc/ to UGC 2885 /R = 122 kpc/. *apj*, 238:471–487, June 1980. 10.1086/158003.

A. Sandage. The change of redshift and apparent luminosity of galaxies due to the deceleration of selected expanding universes. *Astrophys. J.*, 136:319, September 1962. 10.1086/147385.

P. Sarkar, J. Yadav, B. Pandey, and S. Bharadwaj. The scale of homogeneity of the galaxy distribution in SDSS DR6. *mnras*, 399:L128–L131, October 2009. 10.1111/j.1745-3933.2009.00738.x.

M. Seikel and C. Clarkson. Optimising Gaussian processes for reconstructing dark energy dynamics from supernovae. *ArXiv e-prints*, November 2013. URL http://adsabs.harvard.edu/abs/2013arXiv1311.6678S.

M. Seikel, C. Clarkson, and M. Smith. GaPP: Gaussian Processes in Python. Astrophysics Source Code Library, March 2013. URL http://adsabs.harvard.edu/abs/2013ascl.soft03027S.

Marina Seikel, Chris Clarkson, and Mathew Smith. Reconstruction of dark energy and expansion dynamics using Gaussian processes. *JCAP*, 1206:036, 2012. 10.1088/1475-7516/2012/06/036.

Joan Simon, Licia Verde, and Raul Jimenez. Constraints on the redshift dependence of the dark energy potential. *Phys. Rev.*, D71:123001, 2005. 10.1103/PhysRevD.71.123001.

V. M. Slipher. The radial velocity of the Andromeda Nebula. *Lowell Observatory Bulletin*, 2: 56–57, 1913. URL http://adsabs.harvard.edu/abs/1913LowOB...2...56S.

V. M. Slipher. Spectrographic Observations of Nebulae. *Popular Astronomy*, 23:21–24, January 1915. URL http://adsabs.harvard.edu/abs/1915PA.....23...21S.

V. M. Slipher. Nebulae. *Proceedings of the American Philosophical Society*, 56:403–409, 1917. URL http://adsabs.harvard.edu/abs/1917PAPhS..56..403S.

V. M. Slipher. Two Nebulae with Unparalleled Velocities. *Popular Astronomy*, 29:128, 1921. URL http://adsabs.harvard.edu/abs/1921PA.....29..128S.

A. Smith and G. Roberts. *J. R. Statist. Soc.*, B 55:3–23, 1993.

Daniel Stern, Raul Jimenez, Licia Verde, Marc Kamionkowski, and S. Adam Stanford. Cosmic Chronometers: Constraining the Equation of State of Dark Energy. I: H(z) Measurements. *JCAP*, 1002:008, 2010. 10.1088/1475-7516/2010/02/008.

N. Suzuki, D. Rubin, C. Lidman, G. Aldering, R. Amanullah, K. Barbary, L. F. Barrientos, J. Botyanszki, M. Brodwin, N. Connolly, K. S. Dawson, A. Dey, M. Doi, M. Donahue, S. Deustua, P. Eisenhardt, E. Ellingson, L. Faccioli, V. Fadeyev, H. K. Fakhouri, A. S. Fruchter, D. G. Gilbank, M. D. Gladders, G. Goldhaber, A. H. Gonzalez, A. Goobar, A. Gude, T. Hattori, H. Hoekstra, E. Hsiao, X. Huang, Y. Ihara, M. J. Jee, D. Johnston, N. Kashikawa, B. Koester,

K. Konishi, M. Kowalski, E. V. Linder, L. Lubin, J. Melbourne, J. Meyers, T. Morokuma, F. Munshi, C. Mullis, T. Oda, N. Panagia, S. Perlmutter, M. Postman, T. Pritchard, J. Rhodes, P. Ripoche, P. Rosati, D. J. Schlegel, A. Spadafora, S. A. Stanford, V. Stanishev, D. Stern, M. Strovink, N. Takanashi, K. Tokita, M. Wagner, L. Wang, N. Yasuda, H. K. C. Yee, and T. Supernova Cosmology Project. The Hubble Space Telescope Cluster Supernova Survey. V. Improving the Dark-energy Constraints above z $>$ 1 and Building an Early-type-hosted Supernova Sample. *ApJ*, 746:85, February 2012. 10.1088/0004-637X/746/1/85.

T. Tao and V. Vu. Local universality of zeroes of random polynomials. *ArXiv e-prints*, July 2013. URL `http://adsabs.harvard.edu/abs/2013arXiv1307.4357T`.

J.-P. Uzan. Varying Constants, Gravitation and Cosmology. *Living Reviews in Relativity*, 14:2, March 2011. 10.12942/lrr-2011-2.

J. K. Webb, J. A. King, M. T. Murphy, V. V. Flambaum, R. F. Carswell, and M. B. Bainbridge. Indications of a Spatial Variation of the Fine Structure Constant. *Physical Review Letters*, 107 (19):191101, November 2011a. 10.1103/PhysRevLett.107.191101.

J. K. Webb, J. A. King, M. T. Murphy, V. V. Flambaum, R. F. Carswell, and M. B. Bainbridge. Indications of a Spatial Variation of the Fine Structure Constant. *Physical Review Letters*, 107 (19):191101, November 2011b. 10.1103/PhysRevLett.107.191101.

C. Zhang, H. Zhang, S. Yuan, S. Liu, T.-J. Zhang, and Y.-C. Sun. Four new observational H(z) data from luminous red galaxies in the Sloan Digital Sky Survey data release seven. *Research in Astronomy and Astrophysics*, 14:1221, October 2014. 10.1088/1674-4527/14/10/002.

Appendices

Chapter A.

Example of the quantitative approach before cuts

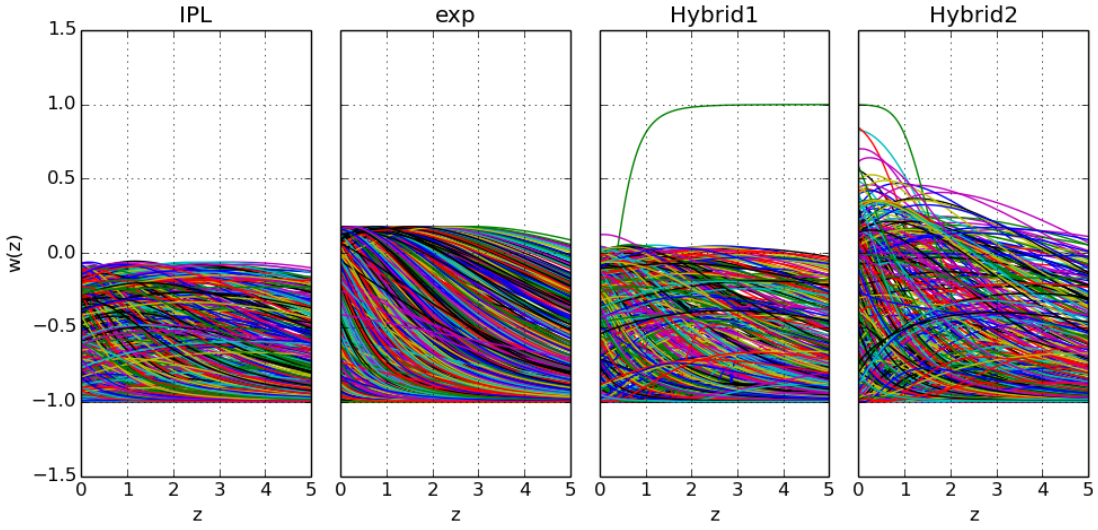

Figure A.1: Evolution of the equation of state for each ”freezing” models before applying the observational cuts. The 2000 samples are shown and the configuration is the standard one: $\dot{\phi}_i = 0$ and Uniform distribution.

Chapter B.

Importance of the chains correction in MCMC

In order to show the importance of the chain correction we illustrate it with the example of the bimodal distribution (one for quintessence, the other one for phantom field) when using the alpha measurements.

In the case of the CPL parametrisation, we chose to use 200 walkers and 2000 steps for each of the walker. The raw results are seen in Figures B.1 and B.2. We see that most of the walkers favor the quintessence model with w_a negative, ζ negative but some walkers exhibits an opposit behaviour. However the latter walkers seem to be stocked in some region because they do not move regularly. So we decided to apply a correction to the chains which is simply to delete every walker whose parameter (either Ω_{m0} or w_0 or w_a or ζ) values do not evolve for 20 steps.

The results are seen in B.3 and B.4, the bimodal distribution is suppressed. To calculate the marginalised posterior distribution we do not take into account the first 500 steps (considered as the burn-in phase).

This highlights one of the drawback of the emcee MCMC code, while enabling parallelisation and implementation of complicated likelihood it does not treat in a robust way multi-model distributions and does not propose a clear convergence criteria in this case.

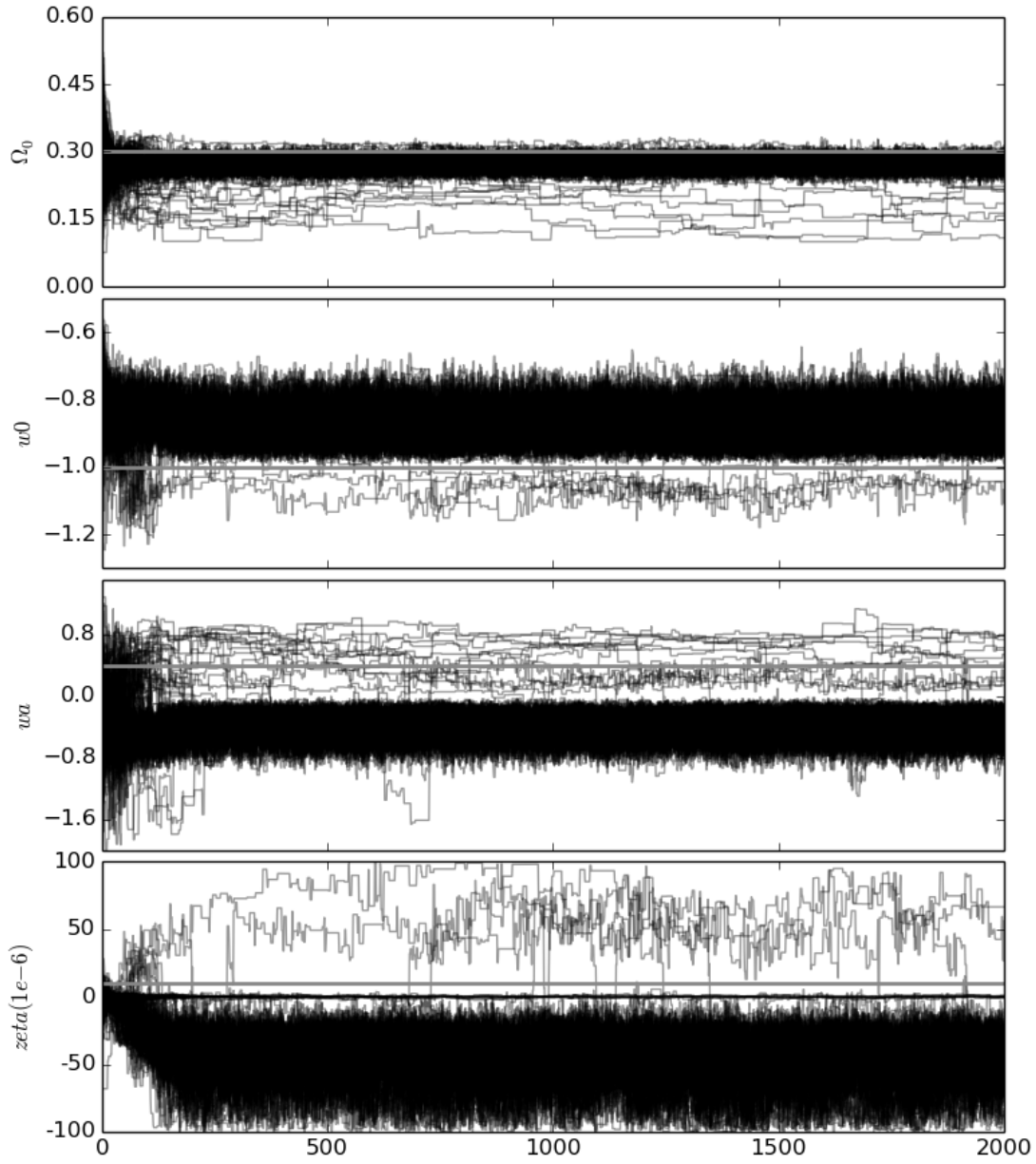

Figure B.1: The raw evolution along the steps of the CPL parametrisations where we allow 4 parameters:Ω_{m0},w_0,w_a and ζ. h is taken equal to 0.7. Each line represent one walker.

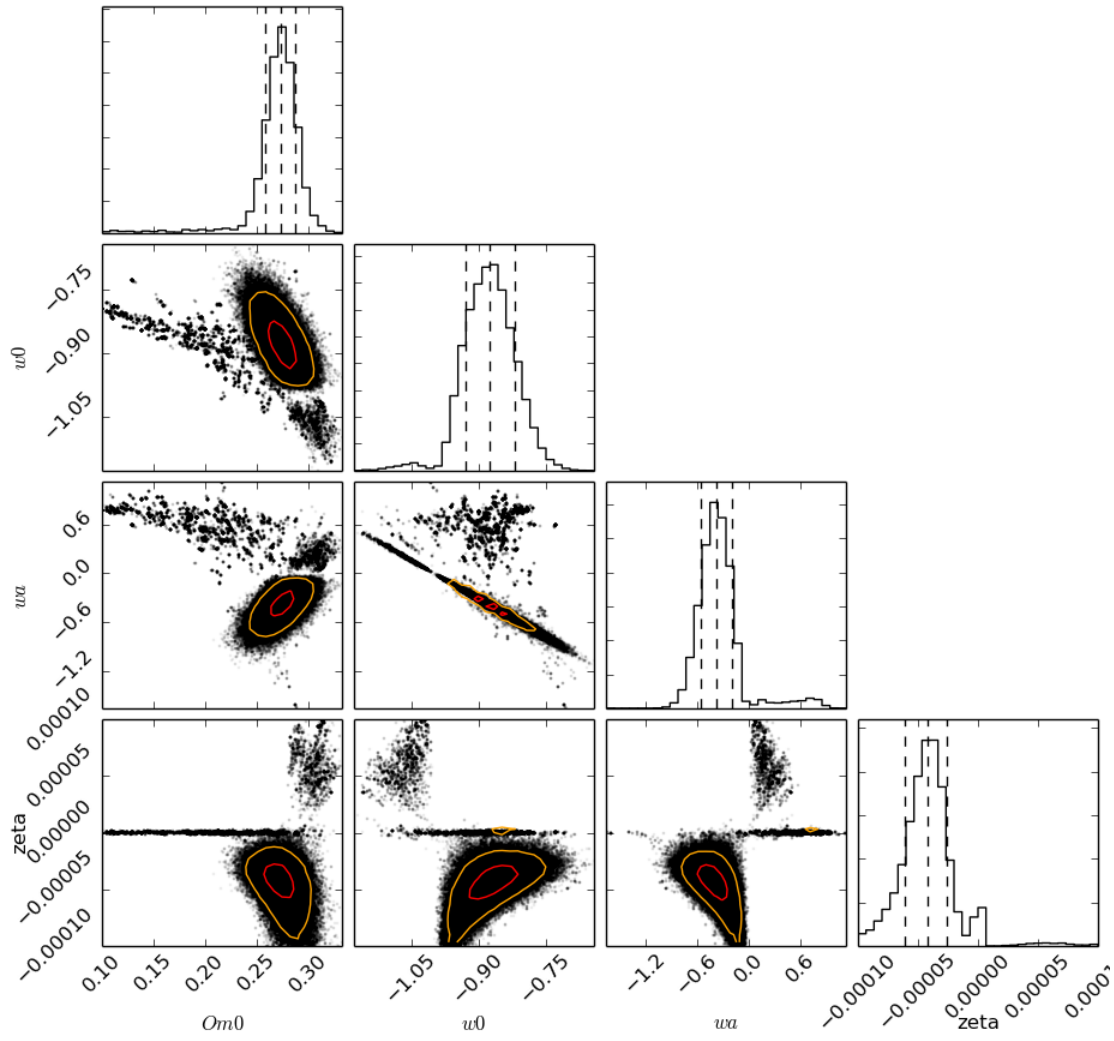

Figure B.2: The raw 2D histograms of the CPL parametrisations where we allow 4 parameters:Ω_{m0},w_0,w_a and ζ. h is taken equal to 0.7. The 1D histograms on the diagonal represents the marginalised posterior distribution for each parameters. The straight contour contains 68% of the points and the dotted one 95%. The dashed lines represent the median values.

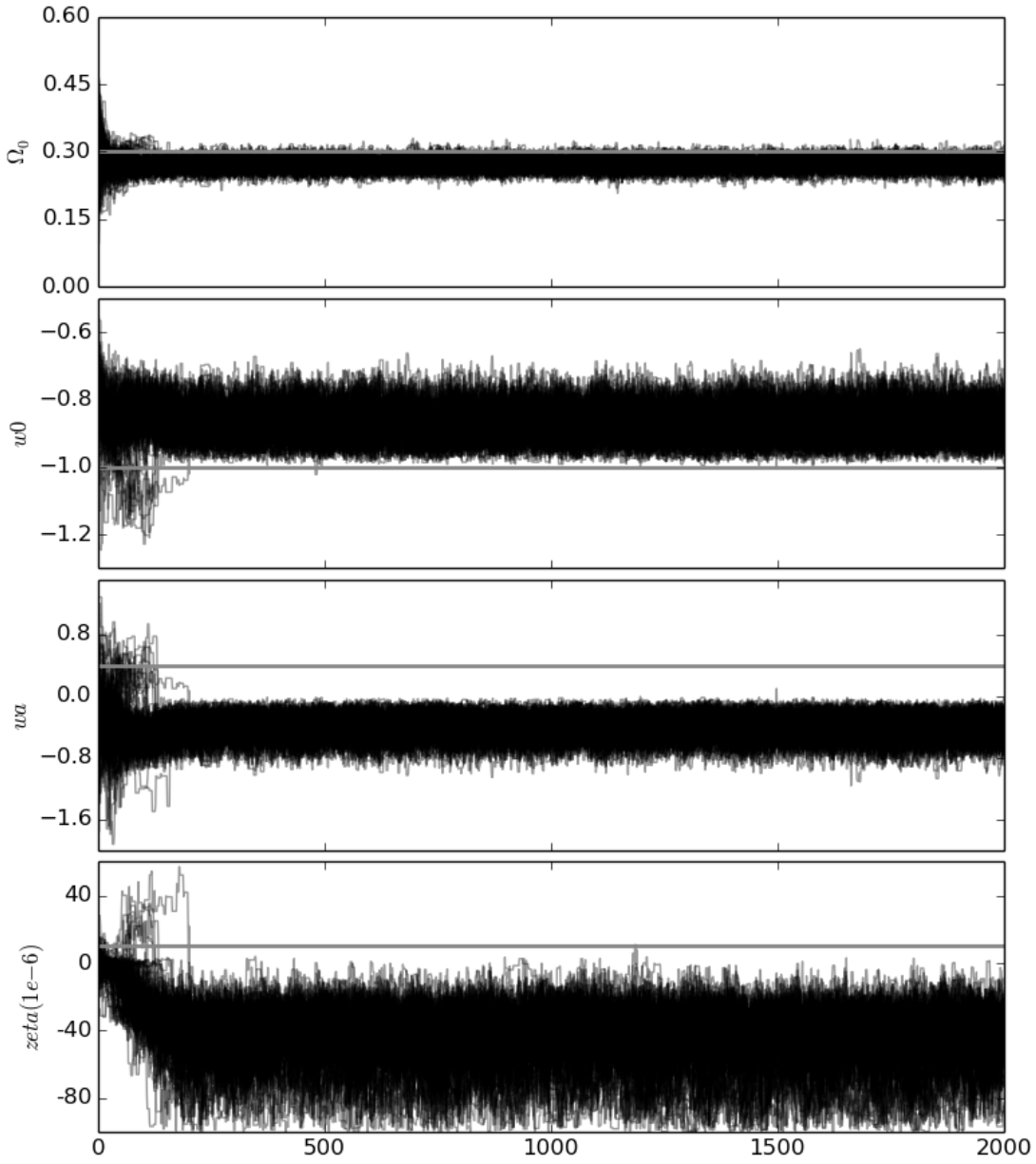

Figure B.3: The corrected evolution along the steps of the CPL parametrisations where we allow 4 parameters:Ω_{m0},w_0,w_a and ζ. h is taken equal to 0.7. Each line represent one walker.

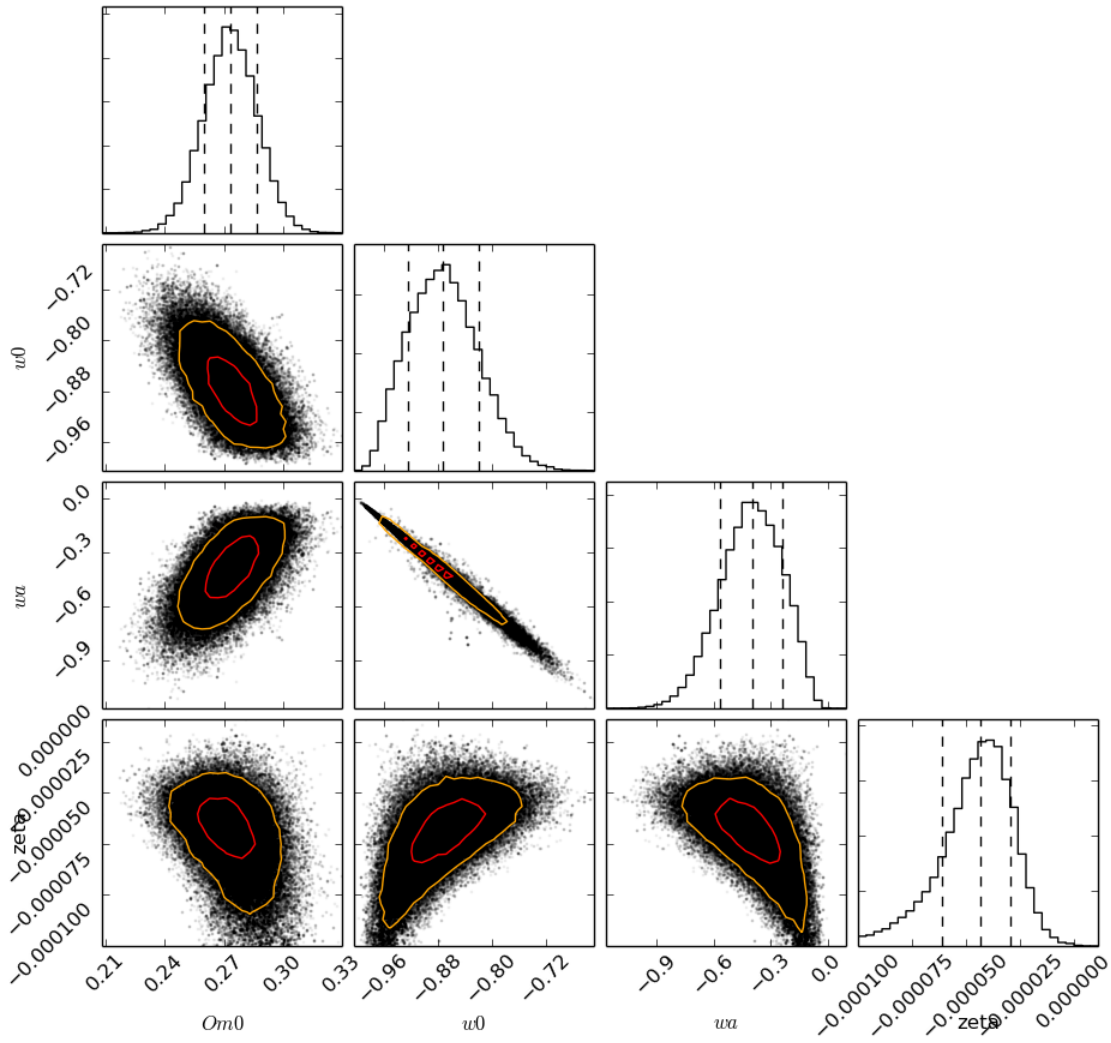

Figure B.4: The corrected 2D histograms of the CPL parametrisations where we allow 4 parameters:Ω_{m0},w_0,w_a and ζ. h is taken equal to 0.7. The 1D histograms on the diagonal represents the marginalised posterior distribution for each parameters. The straight contour contains 68% of the points and the dotted one 95%. The dashed lines represent the median values.